Summer 8-16-2024

Engineering Far-field and Near-field Thermal Radiation Using Metamaterials

Ramin Pouria
University of Maine, ramin.pouria@maine.edu

ENGINEERING FAR-FIELD AND NEAR-FIELD THERMAL RADIATION USING METAMATERIALS

By

Ramin Pouria

B.Sc. Azerbaijan University, Tabriz, Iran, 2012

M.Sc. University of Tehran, Tehran, Iran, 2016

A Dissertation

Submitted in Partial Fulfillment of the

Requirements for the Degree of

Doctor of Philosophy

(in Mechanical Engineering)

The Graduate School

The University of Maine

August 2024

Advisory Committee:

Sheila Edalatpour, Associate Professor of Mechanical Engineering, University of Maine, Advisor

Zhihe Jin, Professor of Mechanical Engineering, University of Maine

Nuri Emanetoglu, Associate Professor of Electrical & Computer Engineering, University of Maine

Mohammad Ghashami, Assistant Professor of Mechanical Engineering, University of Nebraska-Lincoln

Olivier Putzeys, Senior Lecturer of Mechanical Engineering, University of Maine

ENGINEERING FAR-FIELD AND NEAR-FIELD THERMAL RADIATION USING METAMATERIALS

By Ramin Pouria

Dissertation advisor: Dr. Sheila Edalatpour

An Abstract of the Dissertation Presented
in Partial Fulfillment of the Requirements for the
Degree of Doctor of Philosophy
(in Mechanical Engineering)
August 2024

Thermal radiation at observation distances greater than the dominant wavelength of thermal radiation (~10 μm at room temperature) is referred to as the far-field regime. Otherwise, thermal radiation is in the near-field regime. Far-field and near-field thermal radiation have significant applications in thermal management, energy-conversion devices such as thermophotovoltaic power generation, spectroscopy, imaging, infrared cloaking, temperature measurements, and optoelectronics, to name only a few. Usually, these applications require thermal radiative properties that are not found among natural materials. Metamaterials made of micro/nanoscale structures offer a great opportunity for designing thermal emitters with improved thermal radiation properties. This dissertation investigates the engineering of far-field and near-field thermal radiation using metamaterials.

In the far-field regime, two classes of metamaterials, namely polaritonic metamaterials made of micro/nanostructures of polaritonic materials such as silicon carbide (SiC) and Mie-resonance based metamaterials made of micro/nanostructures of dielectric materials, have been studied. The first study elucidates the impact on far-field thermal radiation from SiC nanopillars when the

interparticle spacing between nanopillars is reduced to the nanometer scale, leading to near-field interactions between adjacent nanopillars. Nanopillars of SiC support localized surface phonon modes in their Reststrahlen band which can be capitalized for enhancement of thermal radiation in this spectral range. It is found that the increased volume of thermal emitters as well as the spectral overlap of the localized surface phonon modes with the hybrid waveguide-surface-phonon-polariton mode in arrays with an optimized interparticle spacing of 300 nm enhance the spectral emissivity of silicon carbide to values as high as 1 across a wide range of angles. Usually, Reststrahlen band of dielectric materials such as SiC spans a limited spectral range and does not always overlap with wavelength of peak thermal radiation. Dielectric media can also emit Mie resonances, which are not limited to a spectral range, and can potentially be used for broadband enhancement of emissivity. Thus, in the second far-field study, we design a Mie resonance-based metamaterial that increases thermal radiation from a flat, unpatterned 6H-SiC substrate at the normal direction from 67% to 91% of a blackbody, while demonstrating enhanced emissivity in a wide angular range. We demonstrate that the Mie resonances of SiC microcuboids can be precisely tuned to occur outside the Reststrahlen band of SiC, aligning them with the peak thermal radiation wavelength. For both far-field studies, enhancement of thermal radiation is experimentally demonstrated.

Mie resonance-based metamaterials are also promising for tuning the near-field spectra. Using numerically-exact simulations, the tunability of spectrum of near-field radiative heat flux between Mie resonance-based metamaterials is theoretically investigated. The origins of the peaks in the near-field spectra are identified and the effect of the refractive index, extinction coefficient, shape, and interspacing of Mie resonators, as well as the separation distance of the metamaterials on the spectral locations of peaks in near-field heat flux are studied.

DEDICATION

To My beloved family

ACKNOWLEDGEMENTS

I wish to express my deepest gratitude to my advisor, Dr. Sheila Edalatpour, for her invaluable advice, unwavering support, and patience over the past five years. Her immense knowledge and insight were instrumental throughout my research and the writing of this dissertation. I could not have asked for a more dedicated and supportive advisor and mentor for my Ph.D. study.

I also extend my heartfelt thanks to Dr. Carl P. Tripp, whose expertise and support significantly shaped my experimental methods and the critique of my results. Additionally, my gratitude goes to Dr. Zhihe Jin, Dr. Nuri Emanetoglu, Dr. Mohammad Ghashami, and Dr. Olivier Putzeys for serving on my Ph.D. committee. I am thankful to my fellow lab mates Dr. Saman Zare, Mehran Habibzadeh, Md. Shofiqul Islam, and Md. Jahid Hasan Sagor for their collaborative efforts and technical support. Furthermore, I gratefully acknowledge the Department of Mechanical Engineering and the Graduate School at the University of Maine for providing the resources and support necessary for my research.

Lastly, I sincerely appreciate my parents and my sister for their unconditional love and encouragement throughout my Ph.D. journey. Without their tremendous understanding and support over the past few years, this achievement would not have been possible.

TABLE OF CONTENTS

LIST OF TABLES

LIST OF FIGURES

Chapter 1
Introduction

1.1 An Overview of Thermal Radiation and Its Regimes

Heat transfer is the transfer of energy between two or more bodies due to a temperature difference. It flows from media at higher temperatures to the ones at lower temperature, and it can occur through three mechanisms: conduction, convection, and radiation. Among these three mechanisms, thermal radiation is the only one that does not need a medium for heat transfer, making it effective in vacuum or space environments. Thermal radiation is electromagnetic waves emitted by the media at temperatures greater than absolute zero. These waves are generated by thermally driven stochastic fluctuations of charged particles inside the emitting material. Transfer of energy from one body to another one through the emission and absorption of electromagnetic waves is referred to as radiative heat transfer. Thermal radiation is wavelength dependent and can occur in the spectral range of 100 nm to 100 μm, depending on the temperature. In addition to wavelength λ, thermal radiation is a function of direction and temperature of the emitting body T [1]. In this thesis, focus is on studying thermal radiation in the mid-infrared region of electromagnetic spectrum (2-25 μm). Thermal radiation at wavelengths smaller than 2 μm and greater than 25 μm requires extremely low and high temperatures, respectively, which are not the focus of this research.

Before 1950, a classic theory by Planck [2] was used to describe thermal radiation from any thermal source. According to this theory, thermal radiation from any surface is limited by the blackbody limit. A blackbody is defined as an ideal body absorbing and emitting the maximum amount of thermal radiation at any direction and wavelength [1,2]. Planck's theory was developed

based on the assumption that all characteristic lengths of the problem L_c, which include the size of the emitting body and the distance at which thermal radiation from the emitting body is observed, are much larger than the dominant wavelength of thermal radiation $\lambda_{\max}$ found from Wien's displacement law ($\lambda_{\max} T = 2898$ where T is in Kelvin and $\lambda_{\max}$ is in μm). For example, the dominant wavelength at room temperature is $\lambda_{\max} \sim 10$ μm. The regime where $L_c \gg \lambda_{max}$ is referred to as the Planckian or far-field regimes [3]. Far-field thermal radiation from a body is often characterized by its spectral, directional emissivity (ε'_λ). This property compares the radiative power emitted by an arbitrary body at a given wavelength and direction to that emitted by a blackbody at the same temperature. Thus, emissivity can only get values between 0 and 1.

Planck's theory of thermal radiation [2], cannot be used for understanding thermal radiation in systems where L_c is smaller than or comparable to $\lambda_{\max}$. When $L_c \leq \lambda_{\max}$, the wave nature of thermal radiation becomes very important, giving rise to two effects. First, constructive and destructive interference of thermally emitted electromagnetic waves is non-negligible. Second, the contribution of evanescent waves which decay exponentially from the surface of the emitter is dominant at distances smaller than $\lambda_{\max}$ [4,5]. These effects resulted in the emergence of a research area known as near-field thermal radiation. The description of near-field thermal radiation is done by using fluctuation-dissipation theorem which was incorporated into Maxwell's equations by Sergei M. Rytov in the 1950s [6]. Later, it was shown that in the near-field regime, radiative heat transfer is primarily driven by the contribution of evanescent waves, and the magnitude of near-field radiative heat transfer can exceed the blackbody limit by several orders of magnitude [6].

1.2 Engineering Thermal Emission and Radiative Heat Transfer Using Metamaterials

Far-field and near-field thermal radiation have significant implications for applications such as thermal management [7,8], energy harvesting [9,10], and night visibility [11,12] to name only a few. Most of these applications require specific spectral thermal radiation properties. Thermal radiation properties of natural materials are limited by the number of available materials and mostly determined by their complex refractive index, $(n + \mathrm{i}\kappa)$. To overcome this limitation, metamaterials, which are materials engineered at the subwavelength scale, have been proposed for controlling thermal radiation [13]. Thermal metamaterials hold substantial potential for the development of selective thermal emitters, contributing significantly to the progress of solar cells [14], thermophotovoltaics (TPVs) [15], and infrared thermal sensing applications [16-18], thermal diodes [19,20], radiative cooling [21,22], thermal rectification [23], near-field photonic cooling [24], and infrared cloaking [25]. Thermal radiation from metamaterials is highly dependent on the geometrical parameters of the subwavelength features that constitute the metamaterials. As such, engineering the geometry of subwavelength constituents provides an excellent opportunity to design thermal emitters with desired near-field and far-field properties. The objective of this research is to elucidate some of the unexplored geometry-dependent mechanisms used for controlling the spectrum of far-field thermal emission and near-field radiative heat transfer using metamaterials. In the next subsections, a literature review of the previously proposed concepts as well as the commonly used mechanisms for controlling thermal radiation will be presented.

1.2.1 Engineering Far-Field Thermal Radiation Using Metamaterials

As mentioned before, far-field thermal radiation is characterized by the spectral, directional emissivity, ε'_λ, which is a function of λ, direction (θ, ψ), and T. Metamaterials can be used to control both the spectral distribution, (i.e., its magnitude at different spectral location) and

direction preference of ε_λ'. By engineering metamaterials, different types of far-field thermal emission such as broadband omnidirectional emission, broadband directional emission, narrowband omnidirectional emission, and narrowband directional emission can be achieved. Engineering far-field thermal radiation using metamaterials has several applications. An example application is radiative cooling [8,26-29] for thermal management. Radiative cooling requires metamaterials that completely reflect visible light received from the sun at all incidence angles, (which means thermal radiation is suppressed omnidirectionally over the spectral range of 400-700 nm) while emit like a blackbody in the atmospheric transparency windows (8-13 μm). For applications such as solar thermophotovoltaic (STPV) [30,31], which aims at overcoming the Shockley-Queisser limit in single-junction solar cells, developing customized thermal emitters is crucial. The required emitters should efficiently absorb sunlight like a blackbody while emitting thermal radiation tailored to the bandgap of the solar cell. Thermal camouflage [12], which is another application gaining increasing attention, provides the capability to conceal objects in their surroundings. This is achieved by reducing the emissivity of the material to closely match that of the background, thereby enabling effective concealment from infrared sensors.

Additional applications of metamaterials with engineered emissivity include spectroscopy [32], imaging [33,34], and chemical sensing [16-18,32,35-37]. In the following, we review some of the mechanisms used for engineering emissivity using metamaterials. One dimensional (1-D) gratings were one of the earliest metamaterials proposed for controlling far-field thermal radiation [38]. In 2002, Greffet *et al*. [39] demonstrated that metamaterials made of periodic arrays of 1-D silicon carbide (SiC) gratings on a flat SiC substrate can be designed to emit coherent thermal radiation, i.e., directional thermal radiation. Given that far-field thermal radiation from natural materials is usually incoherent, the development of a highly coherent thermal metamaterial based

on a simplistic 1-D grating is considered a significant achievement. The coherent thermal emission from 1-D gratings of SiC is due to near-field thermal emission of highly coherent surface phonon polaritons (SPhPs) which are coupled to the far-field using the grating [40]. Since then, many computational and experimental studies have explored the effect of introducing 1-D [41-45] and two dimensional (2-D) gratings [46] on the surfaces of substrates supporting resonance modes such as SPhPs, surface plasmon polaritons (SPPs), and microcavity modes. Most of the gratings studied in the literature of thermal radiation are diffractive; meaning that the periodicity of the grating, Λ, is smaller than half of the wavelength, λ. When designed properly, the spectrum of ε'_λ for these diffractive gratings has narrowband peaks or dips and are highly directional.

With the development of new micro/nanofabrication technologies, more complex metamaterials with more degrees of freedom for designing customized thermal radiation have been proposed. These more complex metamaterials utilize SPhP and SPP resonances in polar and plasmonic materials, Mie resonances in high-refractive index dielectric materials, phase change materials, metal-insulator-metal (MIM) configurations, Epsilon-near-zero (ENZ) materials for engineering ε'_λ. For example, Zhai *et al*. [27] designed and demonstrated a scalable metamaterial employing a polymeric thin film embedded with randomly distributed SiO_2 microspheres which have strong Mie resonances in the atmospheric transparency window (8-13 μm). By controlling the size of the spheres, the Mie resonances of the spheres can be spectrally overlapped with the localized surface phonon polaritons of the SiO_2 spheres resulting in resonant far-field thermal radiation in this spectral range. This metamaterial serves as a radiative cooling emitter with an emissivity exceeding 0.93 in the atmospheric window. The same mechanism has been utilized by Howes *et al*. [47] to achieve near-unity thermal radiation from SiC micropillars fabricated on a silicon substrate. Liu *et al*. [48] designed an MIM thermal emitter made of periodic arrays of cross-

shaped gold resonators separated from a gold substrate using a silicon substrate. They achieved an omnidirectional narrowband enhancement of ε_λ' by optimizing the thickness of the dielectric layer and the geometrical parameters of gold resonators. Other MIM-based metamaterials utilizing features such as arrays of disks or cylinders were also proposed for narrowband or broadband omnidirectional thermal emission [17,49,50]. Another class of metamaterials, namely ENZ-based metamaterials, was investigated by Molesky *et al*. [51] where narrowband near-unity enhancement of thermal emission was achieved. Two ENZ-based metamaterials, one with a multilayered structure and the other made of metallic nanowire arrays embedded in a dielectric matrix, were proposed for the manipulation of the parallel and perpendicular effective permittivity to control the direction-dependence of thermal radiation.

The aforementioned studies provide significant insight into engineering thermal radiation using metamaterials. However, there still exists knowledge gaps in understanding thermal radiation mediated by localized surface phonon polaritons and Mie resonances emitted by sub-wavelength particles of polar dielectric media. More specifically, thermal radiation from dense arrays of sub-wavelength particles is not understood, while these metamaterials can result in enhanced and omnidirectional thermal radiation which is suitable for cooling electronic devices and energy harvesting. Also, while localized surface phonons can be capitalized on for enhancing the emissivity, these modes are restricted to a limited spectral region called Reststrahlen band. Mie resonances supported by dielectric media with a large refractive index are not limited to any spectral band. The effect of Mie resonances on far-field thermal radiation has not been studied thoroughly. One of the objectives of this thesis is to address these two knowledge gaps.

1.2.2 Engineering Near-Field Radiative Heat Transfer

Near-field radiative heat transfer (NFRHT) can exceed the blackbody limit by orders of magnitude and can be quasi-monochromatic. The unique properties of NFRHT can be exploited for many potential applications. For example, NFRHT provides a powerful tool for imaging nanostructures beyond the diffraction limit, providing the ability to investigate materials and devices at unprecedented spatial resolutions [52]. In conventional imaging, the diffraction limit restricts the spatial resolution to about half the wavelength of the incident light. In the technique facilitated by NFRHT, which is referred to as near-field scanning thermal microscopy (NSTM), a sharp probe is brought into close proximity of the sample surface, measuring the local density of states thermally emitted in the near-field of the sample [52]. Enhancement of efficiency in TPV power generation is another application of near-field radiative heat transfer [9,10,53,54]. In a conventional TPV system, a high-temperature heat source thermally radiates photons, which are then absorbed by a semiconductor material in the photovoltaic cell to generate electron-hole pairs and produce electricity. However, the power output and efficiency of the conventional TPVs is limited due to the low energy of emitted photons and the spectral mismatch between the thermal emitter and the semiconductor bandgap. Near-field TPVs take advantage of enhanced and quasi-monochromatic heat transfer in the near-field to render larger power output and efficiency than conventional TPVs. Other applications of NFRHT include but not limited to power generation [51,54], thermal management of electronic devices [55], and thermal rectification through a vacuum gap [23,56,57]. Most of these applications require near-field thermal emission properties which are not found among natural materials.

Metamaterials made of hyperbolic [3,58-61], phononic [40,62-66], plasmonic [33,42,49,54,67], and Mie resonance-based materials [10,68-72] have been proposed for tuning NFRHT. Near-field

radiative heat transfer for metamaterial is dependent on material properties and geometry of constituents. Near-field metamaterials can be designed to have near-field thermal properties that significantly deviate from those observed in the constituent materials. The majority of numerical and experimental studies devoted to near-field metamaterials are focused on hyperbolic, phononic, and plasmonic metamaterials for enhancing and tuning NFRHT. Very few studies are done on NFRHT in Mie resonance-based metamaterials. The current studies on Mie resonance-based metamaterials have used approximate methods such as the effective medium theory (EMT) [73-79. In the EMT, the inhomogeneous metamaterial is modeled as a homogeneous media with an effective permittivity and permeability. It has been shown that the EMT is not valid in the near-field regime and can provide inaccurate estimation of both magnitude and spectrum of NFRHT [73]. Only recently, NFRHT between two Mie-resonance based metamaterials made of arrays of tellurium cubes was studied using exact numerical simulations [80]. It was shown that the Maxwell-Garnett EMT significantly underestimates NFRHT even for gap sizes as large as 10 μm, whereas the Mie EMT is not valid for separation distances below 2 μm. Even though this study is performed using numerical simulations rather than EMT, it does not provide insight into the physics underlying NFRHT between Mie resonance-based metamaterials. There is a knowledge gap regarding the origin of the peaks observed in the spectrum of NFRHT between Mie resonance-based metamaterials. It is also not known how the spectral location of the peaks of NFRHT evolve as the material properties and geometrical parameters of the subwavelength emitters vary. Another objective of this thesis is to fill this knowledge gap and elucidate the physics driving NFRHT between Mie resonance-based metamaterials.

1.3 Dissertation Outline

The outline of this dissertation is as follows. In chapter 2, we study the far-field thermal radiation from metamaterials made of periodic arrays of densely packed SiC nanopillars with a periodicity smaller than half of the wavelength of thermal radiation. Nanoparticles of polar materials such as SiC support localized surface phonon polaritons in the spectral range of ~10-12.5 μm. Thermal radiation of these modes is studied both theoretically and experimentally. The theoretical analysis is done using numerical simulations performed using the SCUFF-EM electromagnetic solver [81,82]. The effect of interpillar spacing on emissivity is theoretically analyzed, and a metamaterial with optimal interspacing is designed and fabricated. An experimental setup is developed for direct measurement of spectral, directional emissivity from heated fabricated sample. In chapter 3, we study the far-field thermal emission from periodic arrays of Mie resonance-based SiC microcubes in the spectral range of 2-16 μm which includes 92 % of thermal radiation from a blackbody at 400 ℃. This study aims to show the possibility of using Mie resonances for broadband and omnidirectional enhancement of emissivity in all-dielectric metamaterials which cannot be achieved using localized surface phonons. The effect of size of the cubes and interparticle spacing on the emissivity are investigated. A multipole expansion method is employed to identify the spectral features of the emissivity. A sample of Mie resonance-based metamaterial is fabricated, and the numerical results are compared to experimental measurements. In chapter 4, we study NFRHT between Mie resonance-based metamaterials made of periodic arrays of microparticles with different geometries made from various dielectric materials using exact numerical simulations performed via the Fourier modal method (also known as the rigorous coupled wave analysis) [83]. Using an electromagnetic multipole expansion of the scattering cross section of individual emitters, we identify the contribution of the electric and magnetic Mie

resonances of various orders to NFRHT. This study will elucidate the physics underlying NFRHT between Mie resonance-based metamaterials and can be used for designing near-field thermal emitters with novel thermal radiative properties. Finally, in chapter 5, a summary of the work described in this dissertation and some recommendations for future studies are presented.

1.4 References

[1] Modest, M.F., Mazumder, S., Modest, M.F. and Mazumder, S., 2003. Fundamentals of thermal radiation. *Radiative heat transfer*, *1*, pp.1-29.

[2] Planck, M., 1914. *The theory of heat radiation*. Blakiston.

[3] Guo, Y., Cortes, C.L., Molesky, S. and Jacob, Z., 2012. Broadband super-Planckian thermal emission from hyperbolic metamaterials. *Applied Physics Letters*, *101*(13).

[4] Edalatpour, S., 2019. Near-field thermal emission by periodic arrays. *Physical Review E*, *99*(6), p.063308.

[5] Song, B., Fiorino, A., Meyhofer, E. and Reddy, P., 2015. Near-field radiative thermal transport: From theory to experiment. *AIP advances*, *5*(5).

[6] Rytov, S.M. and Erkku, H., 1959. *Theory of electric fluctuations and thermal radiation* (p. 0280). Bedford, MA: Air Force Cambridge Research Center.

[7] Guha, B., Otey, C., Poitras, C.B., Fan, S. and Lipson, M., 2012. Near-field radiative cooling of nanostructures. *Nano letters*, *12*(9), pp.4546-4550.

[8] Hossain, M.M., Jia, B. and Gu, M., 2015. A metamaterial emitter for highly efficient radiative cooling. *Adv. Opt. Mater*, *3*(8), pp.1047-1051.

[9] Bhatt, G.R., Zhao, B., Roberts, S., Datta, I., Mohanty, A., Lin, T., Hartmann, J.M., St-Gelais, R., Fan, S. and Lipson, M., 2020. Integrated near-field thermo-photovoltaics for heat recycling. *Nature communications*, *11*(1), p.2545.

[10] Ghanekar, A., Tian, Y., Zhang, S., Cui, Y. and Zheng, Y., 2017. Mie-metamaterials-based thermal emitter for near-field thermophotovoltaic systems. *Materials*, *10*(8), p.885.

[11] Lee, N., Kim, T., Lim, J.S., Chang, I. and Cho, H.H., 2019. Metamaterial-selective emitter for maximizing infrared camouflage performance with energy dissipation. *ACS applied materials & interfaces*, *11*(23), pp.21250-21257.

[12] Pan, M., Huang, Y., Li, Q., Luo, H., Zhu, H., Kaur, S. and Qiu, M., 2020. Multi-band middle-infrared-compatible camouflage with thermal management via simple photonic structures. *Nano Energy*, *69*, p.104449.

[13] Petersen, S.J., Basu, S. and Francoeur, M., 2013. Near-field thermal emission from metamaterials. *Photonics and Nanostructures-Fundamentals and Applications*, *11*(3), pp.167-181.

[14] Davidsen, R.S., Li, H., To, A., Wang, X., Han, A., An, J., Colwell, J., Chan, C., Wenham, A., Schmidt, M.S. and Boisen, A., 2016. Black silicon laser-doped selective emitter solar cell with 18.1% efficiency. *Solar Energy Materials and Solar Cells*, *144*, pp.740-747.

[15] Molesky, S., Dewalt, C.J. and Jacob, Z., 2013. High temperature epsilon-near-zero and epsilon-near-pole metamaterial emitters for thermophotovoltaics. *Optics express*, *21*(101), pp.A96-A110.

[16] Pejcic, B., Myers, M. and Ross, A., 2009. Mid-infrared sensing of organic pollutants in aqueous environments. *Sensors*, *9*(8), pp.6232-6253.

[17] Gong, Y., Wang, Z., Li, K., Uggalla, L., Huang, J., Copner, N., Zhou, Y., Qiao, D. and Zhu, J., 2017. Highly efficient and broadband mid-infrared metamaterial thermal emitter for optical gas sensing. *Optics letters*, *42*(21), pp.4537-4540.

[18] Hodgkinson, J. and Tatam, R.P., 2012. Optical gas sensing: a review. *Measurement science and technology*, *24*(1), p.012004.

[19] Li, Q., He, H., Chen, Q. and Song, B., 2021. Radiative thermal diode via hyperbolic metamaterials. *Physical Review Applied*, *16*(6), p.064022.

[20] Huang, H., Shan, S. and Zhou, Z., 2023. Near-field thermal diode based on 2d gratings. *International Journal of Heat and Mass Transfer*, *206*, p.123942.

[21] Kong, A., Cai, B., Shi, P. and Yuan, X.C., 2019. Ultra-broadband all-dielectric metamaterial thermal emitter for passive radiative cooling. *Optics express*, *27*(21), pp.30102-30115.

[22] Huang, G., Yengannagari, A.R., Matsumori, K., Patel, P., Datla, A., Trindade, K., Amarsanaa, E., Zhao, T., Köhler, U., Busko, D. and Richards, B.S., 2024. Radiative cooling and indoor light management enabled by a transparent and self-cleaning polymer-based metamaterial. *Nature Communications*, *15*(1), p.3798.

[23] Wang, L.P. and Zhang, Z.M., 2013. Thermal rectification enabled by near-field radiative heat transfer between intrinsic silicon and a dissimilar material. *Nanoscale and microscale thermophysical engineering*, *17*(4), pp.337-348.

[24] Zhu, L., Fiorino, A., Thompson, D., Mittapally, R., Meyhofer, E. and Reddy, P., 2019. Near-field photonic cooling through control of the chemical potential of photons. *Nature*, *566*(7743), pp.239-244.

[25] Amemiya, T., Yamasaki, S., Kanazawa, T., Gu, Z., Inoue, D., Ishikawa, A., Nishiyama, N., Tanaka, T., Urakami, T. and Arai, S., 2018, May. Infrared Invisibility Cloak Using Rolled Metamaterial Film. In *2018 Conference on Lasers and Electro-Optics (CLEO)* (pp. 1-2). IEEE.

[26] Kong, A., Cai, B., Shi, P. and Yuan, X.C., 2019. Ultra-broadband all-dielectric metamaterial thermal emitter for passive radiative cooling. Optics express, 27(21), pp.30102-30115.

[27] Zhai, Y., Ma, Y., David, S.N., Zhao, D., Lou, R., Tan, G., Yang, R. and Yin, X., 2017. Scalable-manufactured randomized glass-polymer hybrid metamaterial for daytime radiative cooling. *Science*, *355*(6329), pp.1062-1066.

[28] Li, Y., Gao, W., Li, L., Guo, L., Ge, H., Xie, R., Wang, H., Wang, F. and An, B., 2022. Ultra-broadband thermal radiator for daytime passive radiative cooling based on single dielectric SiO2 on metal Ag. *Energy Reports*, *8*, pp.852-859.

[29] Gao, M., Han, X., Chen, F., Zhou, W., Liu, P., Shan, Y., Chen, Y., Li, J., Zhang, R., Wang, S. and Zhang, Q., 2019. Approach to fabricating high-performance cooler with near-ideal emissive spectrum for above-ambient air temperature radiative cooling. *Solar Energy Materials and Solar Cells*, *200*, p.110013.

[30] Lenert, A., Bierman, D.M., Nam, Y., Chan, W.R., Celanović, I., Soljačić, M. and Wang, E.N., 2014. A nanophotonic solar thermophotovoltaic device. *Nature nanotechnology*, *9*(2), pp.126-130.

[31] Dang, P.T., Kim, J., Nguyen, T.K., Le, K.Q. and Lee, J.H., 2021. Ultra-broadband metamaterial absorber for high solar thermal energy conversion efficiency. *Physica B: Condensed Matter*, *620*, p.413261.

[32] Wei, J., Ren, Z. and Lee, C., 2020. Metamaterial technologies for miniaturized infrared spectroscopy: Light sources, sensors, filters, detectors, and integration. *Journal of Applied Physics*, *128*(24).

[33] Tittl, A., Michel, A.K.U., Schäferling, M., Yin, X., Gholipour, B., Cui, L., Wuttig, M., Taubner, T., Neubrech, F. and Giessen, H., 2015. A switchable mid-infrared plasmonic perfect absorber with multispectral thermal imaging capability. *Advanced Materials*, *27*(31), pp.4597-4603.

[34] Zeng, B., Huang, Z., Singh, A., Yao, Y., Azad, A.K., Mohite, A.D., Taylor, A.J., Smith, D.R. and Chen, H.T., 2018. Hybrid graphene metasurfaces for high-speed mid-infrared light modulation and single-pixel imaging. *Light: Science & Applications*, *7*(1), p.51.

[35] Song, K., Wang, Q., Liu, Q., Zhang, H. and Cheng, Y., 2011. A wireless electronic nose system using a Fe2O3 gas sensing array and least squares support vector regression. *Sensors*, *11*(1), pp.485-505.

[36] Lochbaum, A., Dorodnyy, A., Koch, U., Koepfli, S.M., Volk, S., Fedoryshyn, Y., Wood, V. and Leuthold, J., 2020. Compact mid-infrared gas sensing enabled by an all-metamaterial design. *Nano letters*, *20*(6), pp.4169-4176.

[37] Senesky, D.G., Jamshidi, B., Cheng, K.B. and Pisano, A.P., 2009. Harsh environment silicon carbide sensors for health and performance monitoring of aerospace systems: A review. *IEEE Sensors Journal*, *9*(11), pp.1472-1478.

[38] Hesketh, P.J., Zemel, J.N. and Gebhart, B., 1986. Organ pipe radiant modes of periodic micromachined silicon surfaces. *Nature*, *324*(6097), pp.549-551.

[39] Greffet, J.J., Carminati, R., Joulain, K., Mulet, J.P., Mainguy, S. and Chen, Y., 2002. Coherent emission of light by thermal sources. *Nature*, *416*(6876), pp.61-64.

[40] Caldwell, J.D., Lindsay, L., Giannini, V., Vurgaftman, I., Reinecke, T.L., Maier, S.A. and Glembocki, O.J., 2015. Low-loss, infrared and terahertz nanophotonics using surface phonon polaritons. *Nanophotonics*, *4*(1), pp.44-68.

[41] Nguyen-Huu, N., Chen, Y.B. and Lo, Y.L., 2012. Development of a polarization-insensitive thermophotovoltaic emitter with a binary grating. *Optics express*, *20*(6), pp.5882-5890.

[42] Hooper, I.R. and Sambles, J.R., 2002. Dispersion of surface plasmon polaritons on short-pitch metal gratings. *Physical Review B*, *65*(16), p.165432.

[43] Watjen, J.I., Liu, X.L., Zhao, B. and Zhang, Z.M., 2017. A computational simulation of using tungsten gratings in near-field thermophotovoltaic devices. *Journal of Heat Transfer*, *139*(5), p.052704.

[44] Le Gall, J., Olivier, M. and Greffet, J.J., 1997. Experimental and theoretical study of reflection and coherent thermal emissionby a SiC grating supporting a surface-phonon polariton. *Physical Review B*, *55*(15), p.10105.

[45] Ito, K., Matsui, T. and Iizuka, H., 2014. Thermal emission control by evanescent wave coupling between guided mode of resonant grating and surface phonon polariton on silicon carbide plate. *Applied Physics Letters*, *104*(5).

[46] Arnold, C., Marquier, F., Garin, M., Pardo, F., Collin, S., Bardou, N., Pelouard, J.L. and Greffet, J.J., 2012. Coherent thermal infrared emission by two-dimensional silicon carbide gratings. *Physical Review B—Condensed Matter and Materials Physics*, *86*(3), p.035316.

[47] Howes, A., Nolen, J.R., Caldwell, J.D. and Valentine, J., 2020. Near-unity and narrowband thermal emissivity in balanced dielectric metasurfaces. *Advanced Optical Materials*, *8*(4), p.1901470.

[48] Liu, X., Tyler, T., Starr, T., Starr, A.F., Jokerst, N.M. and Padilla, W.J., 2011. Taming the blackbody with infrared metamaterials as selective thermal emitters. *Physical review letters*, *107*(4), p.045901.

[49] Yokoyama, T., Dao, T.D., Chen, K., Ishii, S., Sugavaneshwar, R.P., Kitajima, M. and Nagao, T., 2016. Spectrally selective mid-infrared thermal emission from molybdenum plasmonic metamaterial operated up to 1000 C. *Adv. Opt. Mater*, *4*(12), pp.1987-1992.

[50] Matsuno, Y. and Sakurai, A., 2017. Perfect infrared absorber and emitter based on a large-area metasurface. *Optical Materials Express*, *7*(2), pp.618-626.

[51] Molesky, S., Dewalt, C.J. and Jacob, Z., 2013. High temperature epsilon-near-zero and epsilon-near-pole metamaterial emitters for thermophotovoltaics. *Optics express*, *21*(101), pp.A96-A110.

[52] Kittel, A., Wischnath, U.F., Welker, J., Huth, O., Rueting, F. and Biehs, S.A., 2008. Near-field thermal imaging of nanostructured surfaces. *Applied Physics Letters*, *93*(19).

[53] Legendre, J. and Chapuis, P.O., 2022. Overcoming non-radiative losses with AlGaAs PIN junctions for near-field thermophotonic energy harvesting. *Applied Physics Letters*, *121*(19).

[54] Yu, H., Duan, Y. and Yang, Z., 2018. Selectively enhanced near-field radiative transfer between plasmonic emitter and GaSb with nanohole and nanowire periodic arrays for thermophotovoltaics. *International Journal of Heat and Mass Transfer*, *123*, pp.67-74.

[55] Latella, I., Biehs, S.A. and Ben-Abdallah, P., 2021. Smart thermal management with near-field thermal radiation. *Optics Express*, *29*(16), pp.24816-24833.

[56] Basu, S. and Francoeur, M., 2011. Near-field radiative transfer based thermal rectification using doped silicon. *Applied Physics Letters*, *98*(11).

[57] Yang, Y., Basu, S. and Wang, L., 2013. Radiation-based near-field thermal rectification with phase transition materials. *Applied Physics Letters*, *103*(16).

[58] Chang, J.Y., Yang, Y. and Wang, L., 2015. Tungsten nanowire based hyperbolic metamaterial emitters for near-field thermophotovoltaic applications. *International Journal of Heat and Mass Transfer*, *87*, pp.237-247.

[59] Biehs, S.A., Tschikin, M. and Ben-Abdallah, P., 2012. Hyperbolic metamaterials as an analog of a blackbody in the near field. *Physical review letters*, *109*(10), p.104301.

[60] Biehs, S.A., Tschikin, M., Messina, R. and Ben-Abdallah, P., 2013. Super-Planckian near-field thermal emission with phonon-polaritonic hyperbolic metamaterials. *Applied Physics Letters*, *102*(13).

[61] Liu, B. and Shen, S., 2013. Broadband near-field radiative thermal emitter/absorber based on hyperbolic metamaterials: Direct numerical simulation by the Wiener chaos expansion method. *Physical Review B—Condensed Matter and Materials Physics*, *87*(11), p.115403.

[62] Lu, G., Nolen, J.R., Folland, T.G., Tadjer, M.J., Walker, D.G. and Caldwell, J.D., 2020. Narrowband polaritonic thermal emitters driven by waste heat. *ACS omega*, *5*(19), pp.10900-10908.

[63] Lu, G., Gubbin, C.R., Nolen, J.R., Folland, T., Tadjer, M.J., De Liberato, S. and Caldwell, J.D., 2021. Engineering the spectral and spatial dispersion of thermal emission via polariton–phonon strong coupling. *Nano letters*, *21*(4), pp.1831-1838.

[64] Wang, T., Li, P., Chigrin, D.N., Giles, A.J., Bezares, F.J., Glembocki, O.J., Caldwell, J.D. and Taubner, T., 2017. Phonon-polaritonic bowtie nanoantennas: controlling infrared thermal radiation at the nanoscale. *Acs Photonics*, *4*(7), pp.1753-1760.

[65] Razdolski, I., Chen, Y., Giles, A.J., Gewinner, S., Schöllkopf, W., Hong, M., Wolf, M., Giannini, V., Caldwell, J.D., Maier, S.A. and Paarmann, A., 2016. Resonant enhancement of second-harmonic generation in the mid-infrared using localized surface phonon polaritons in subdiffractional nanostructures. *Nano letters*, *16*(11), pp.6954-6959.

[66] Chen, Y., Francescato, Y., Caldwell, J.D., Giannini, V., Maß, T.W., Glembocki, O.J., Bezares, F.J., Taubner, T., Kasica, R., Hong, M. and Maier, S.A., 2014. Spectral tuning of localized surface phonon polariton resonators for low-loss mid-IR applications. *Acs Photonics*, *1*(8), pp.718-724.

[67] Garcia-Vidal, F.J., Sanchez-Dehesa, J., Dechelette, A., Bustarret, E., Lopez-Rios, T., Fournier, T. and Pannetier, B., 1999. Localized surface plasmons in lamellar metallic gratings. *Journal of Lightwave technology*, *17*(11), p.2191.

[68] Kivshar, Y. and Miroshnichenko, A., 2017. Meta-optics with Mie resonances. *Optics and Photonics news*, *28*(1), pp.24-31.

[69] Spinelli, P., Verschuuren, M.A. and Polman, A., 2012. Broadband omnidirectional antireflection coating based on subwavelength surface Mie resonators. *Nature communications*, *3*(1), p.692.

[70] Liu, T., Xu, R., Yu, P., Wang, Z. and Takahara, J., 2020. Multipole and multimode engineering in Mie resonance-based metastructures. *Nanophotonics*, *9*(5), pp.1115-1137.

[71] Bezares, F.J., Long, J.P., Glembocki, O.J., Guo, J., Rendell, R.W., Kasica, R., Shirey, L., Owrutsky, J.C. and Caldwell, J.D., 2013. Mie resonance-enhanced light absorption in periodic silicon nanopillar arrays. *Optics Express*, *21*(23), pp.27587-27601.

[72] Petersen, S.J., Basu, S., Raeymaekers, B. and Francoeur, M., 2013. Tuning near-field thermal radiative properties by quantifying sensitivity of Mie resonance-based metamaterial design parameters. *Journal of Quantitative Spectroscopy and Radiative Transfer*, *129*, pp.277-286.

[73] Zare, S., Pouria, R. and Edalatpour, S., 2021. Validity of the effective medium theory for modeling near-field thermal emission by nanowire arrays. *Journal of Quantitative Spectroscopy and Radiative Transfer*, *261*, p.107482.

[74] Didari, A. and Mengüç, M.P., 2015. Near-to far-field coherent thermal emission by surfaces coated by nanoparticles and the evaluation of effective medium theory. *Optics express*, *23*(11), pp.A547-A552.

[75] Yang, Y., Sabbaghi, P. and Wang, L., 2017. Effect of magnetic polaritons in SiC deep gratings on near-field radiative transfer. *International Journal of Heat and Mass Transfer*, *108*, pp.851-859.

[76] Yang, Y. and Wang, L., 2016. Spectrally enhancing near-field radiative transfer between metallic gratings by exciting magnetic polaritons in nanometric vacuum gaps. *Physical review letters*, *117*(4), p.044301.

[77] Liu, X. and Zhang, Z., 2015. Near-field thermal radiation between metasurfaces. *Acs Photonics*, *2*(9), pp.1320-1326.

[78] Liu, X., Zhao, B. and Zhang, Z.M., 2015. Enhanced near-field thermal radiation and reduced Casimir stiction between doped-Si gratings. *Physical Review A*, *91*(6), p.062510.

[79] Liu, X.L., Bright, T.J. and Zhang, Z.M., 2014. Application conditions of effective medium theory in near-field radiative heat transfer between multilayered metamaterials. *Journal of Heat Transfer*, *136*(9), p.092703.

[80] Hu, Y., Li, H., Zhang, Y., Zhu, Y. and Yang, Y., 2020. Enhanced near-field radiation in both TE and TM waves through excitation of Mie resonance. *Physical Review B*, *102*(12), p.125434.

[81] Reid, M.H. and Johnson, S.G., 2015. Efficient computation of power, force, and torque in BEM scattering calculations. *IEEE Transactions on Antennas and Propagation*, *63*(8), pp.3588-3598.

[82] Reid, M.H. and Johnson, S.G., *Solving Electromagnetic Scattering Problems with Scuff-Scatter*, http://homerreid.github.io/scuff-em-documentation/applications/scuff-scatter/scuff-scatter/.

[83] Chen, K., Zhao, B. and Fan, S., 2018. MESH: A free electromagnetic solver for far-field and near-field radiative heat transfer for layered periodic structures. *Computer Physics Communications*, *231*, pp.163-172.

Chapter 2

Far-Field Thermal Radiation from Short-Pitch Silicon-Carbide Nanopillar Arrays

This chapter has been reproduced from a previous publication in Applied Physics Letters: Pouria, R., Chow, P.K., Tiwald, T., Zare, S. and Edalatpour, S., 2022. Far-field thermal radiation from short-pitch silicon-carbide nanopillar arrays. *Applied Physics Letters, 121*(13).

2.1 Abstract

Silicon carbide (SiC) supports surface phonons in the infrared region of the electromagnetic spectrum where these modes can be thermally emitted. Additionally, the magnitude, spectrum, and direction of thermal radiation from SiC can be controlled by engineering this material at the sub-wavelength scale. For these reasons, SiC nanopillars are of high interest for thermal-radiation tuning. So far, theoretical and experimental studies of thermal emission from SiC nanopillars have been limited to long-pitch arrays with a microscale interpillar spacing. It is not clear how far-field thermal emission from SiC nanopillars is affected when the interparticle spacing reduces to the nanometer scale, where the near-field interaction between adjacent nanopillars arises and the array becomes zero order. In this letter, we study physical mechanisms of far-field thermal radiation from zero-order arrays of silicon-carbide nanopillars with a nanoscale interpillar spacing. We show that the increased volume of thermal emitters and thermal radiation of the hybrid waveguide-surface-phonon-polariton mode from zero-order arrays increase the spectral emissivity of silicon carbide to values as large as 1 for a wide range of angles. The enhanced, dispersion-less thermal emission from a zero-order SiC array of nano-frustums with an optimized interspacing of 300 nm is experimentally demonstrated. Our study provides insight into thermal radiation from dense nanostructures and has significant implications for thermal management of electronic devices and energy harvesting applications.

2.2 Introduction

Flat surfaces of polar dielectric materials can support propagating surface phonon polaritons (SPhPs) in the infrared range of the electromagnetic spectrum, where these modes can be thermally emitted [1-3]. The spectral location of the SPhP modes is between the longitudinal and transverse optical phonon frequencies of the material, which is referred to as the Reststrahlen band [3,4]. The parallel component of the wavevector, k_ρ, for the SPhPs is greater than the wavevector in both the dielectric material and the free space (k_0). As such, the SPhPs are evanescent in both media [2]. Since SPhPs are confined to a distance approximately equal to the thermal wavelength from the emitter, they can only contribute to the near-field thermal radiation. Indeed, polar dielectrics are poor far-field emitters in their Reststrahlen band, since these materials have negative permittivity (and thus are highly reflective) in this band [4]. One- and two-dimensional periodic gratings have been proposed for enhancing far-field thermal emission from polar dielectric materials [5-12]. Gratings reduce k_ρ of SPhPs to values less than k_0, such that the SPhPs can couple to propagating modes in the free space [5-12]. The coupling of SPhPs to propagating modes significantly enhances far-field thermal emission characterized by the emissivity of the material. However, far-field thermal emission from gratings is highly coherent and thus directional [5-12]. Sub-wavelength particles of polar dielectric materials can support localized surface phonons (LSPhs) [4,13-19]. Unlike SPhPs, LSPhs can have k_ρs smaller than k_0 and thus can contribute to the far-field thermal radiation. Additionally, the dispersion relation of LSPhs is almost flat [16], such that LSPhs can enhance emissivity in a wide range of directions. When fabricated on a polar dielectric substrate, an array of sub-wavelength particles can also serve as a grating and couple SPhPs of the substrate to the far zone. This coupling provides an additional mechanism for enhancing emissivity of the material. Due to the enhanced emissivity and the ability to tune the spectrum and direction

of thermal radiation, sub-wavelength structures of polaritonic materials, such as silicon carbide (SiC), have been of high interest [20-25]. More complex structures made of sub-wavelength particles of two different geometries have also proven promising for achieving near-perfect absorption in a broad band [26]. So far, most of the theoretical and experimental studies on thermal radiation from SiC sub-wavelength structures have been concerned with diffractive arrays that have a pitch size, Λ, greater than half of the thermal wavelength, λ. The mechanism of thermal radiation in diffractive arrays is different from short-pitch, non-diffractive (zero-order) arrays with $\Lambda < \frac{\lambda}{2}$. This letter addresses the emissivity of zero-order arrays of sub-wavelength particles of SiC both theoretically and experimentally. It is shown that while zero-order arrays cannot couple the SPhPs emitted from the substrate into the far zone, they can emit a dispersion-less electromagnetic mode, namely the hybrid waveguide-SPhP resonance. This electromagnetic mode causes a new peak in thermal radiation from the array. Additionally, the effect of interpillar spacing on the emissivity of periodic arrays of SiC nanoparticles is addressed in this letter. While the emissivity of the array initially increases by decreasing the interpillar spacing (due to the increase in the volume of the thermal emitter), further decrease in interpillar spacing reduces thermal emission due to the strong near-field interactions between the nanoparticles. It is demonstrated that the increased volume of emitters and thermal radiation of waveguide-SPhP mode in the zero-order arrays can be capitalized on for increasing the spectral emissivity significantly up to the blackbody value of 1 in a wide range of directions. The enhanced far-field thermal radiation from nanopillars has significant implications for applications such as high-temperature SiC electronic cooling and energy harvesting using thermophotovoltaic devices.

2.3 Problem Description, Results, and Discussion

To study the effect of interparticle spacing on far-field thermal radiation, we select 6H-SiC nanopillars with the shape of a frustum of a cone [see the inset of Fig. 2-1(b)]. The frustums have a bottom diameter of D_1 = 700 nm, a top diameter of D_2 = 500 nm, and a height of H = 1000 nm. The dimensions of the nanopillars are selected such that they emit both longitudinal and transversal LSPhs, while they can also be experimentally fabricated. Thermal emission by isolated nanopillars is proportional to the imaginary part of their electric polarizability, $\mathrm{Im}[\alpha]$ (see Sec. A.1 of the Appendix A). As such, the spectral locations of the longitudinal and transversal LSPhs can be estimated by considering the spectrum of $\mathrm{Im}[\alpha]$. For cylindrical nanopillars, the polarizability along direction j ($j = x, y, z$) is found as $\alpha_j = V\frac{\varepsilon-1}{1+L_j(\varepsilon-1)}$, where V, ε, and L_j are the volume, dielectric function, and depolarization factor of the nanopillar in direction j, respectively [25,26]. The depolarization factor of the cylindrical nanopillars along x, y, z directions [see the inset of Fig. 2-1(a)] can be estimated as $L_x = L_y = \frac{1}{2}\cos\varphi - i\frac{k_0^3}{6\pi}V$ and $L_z = 1 - \cos\varphi - \frac{k_0^2}{6\pi}VC_z - i\frac{k_0^3}{6\pi}V$, where i is the imaginary unit, $\varphi = \tan^{-1}(D/H)$, and $C_z = \frac{3}{2H}\ln\left|\frac{1+E}{1-E}\right|$ with $E = 1 + \left(\frac{D}{H}\right)^2$ [27,28]. For nano-frustums, the diameter varies along the z-axis from 500 nm at the top to 700 nm at the bottom. The spectral locations of the longitudinal and transversal LSPhs of a frustum-shaped nanopillar can be estimated by considering $\mathrm{Im}[\alpha]$ of cylindrical nanopillars with diameters between 500 nm and 700 nm. Figure 1a shows $\mathrm{Im}[\alpha_{x,y}]$ (transversal polarizability) and $\mathrm{Im}[\alpha_z]$ (longitudinal polarizability) for cylinders of height H = 1000 nm and three diameters D of 500 nm, 600 nm, and 700 nm. A temperature T of 400°C is assumed, and the ordinary and extraordinary dielectric functions of 6H-SiC at this temperature are measured using ellipsometry (see Sec. A.2 of Appendix A). The ordinary dielectric function of 6H-SiC was used for the calculations. As it is

seen from Fig. 2-1(a), $\mathrm{Im}[\alpha_{x,y}]$ and $\mathrm{Im}[\alpha_z]$ each has a peak corresponding to the transversal and longitudinal dipolar LSPhs, respectively. When D changes from 500 to 700 nm, the spectral location of the longitudinal peak varies from 894 to 918 cm^{-1} while the wavenumber of the transversal mode decreases very slightly from 934 to 930 cm^{-1}. Figure 2-1(b) shows the normalized absorption cross section for an isolated frustum-shaped nanopillar at T = 400°C as obtained using the SCUFF-SCATTER tool of the SCUFF-EM electromagnetic solver [29,30]. The peak and the shoulder at 905 and 911 cm^{-1} are within the spectral band in which $\mathrm{Im}[\alpha_z]$ is maximal, and thus they are due to excitation of the longitudinal LSPhs. The peak at 933 cm^{-1} is associated with the resonance of $\mathrm{Im}[\alpha_{x,y}]$ caused by excitation of transversal dipolar LSPhs.

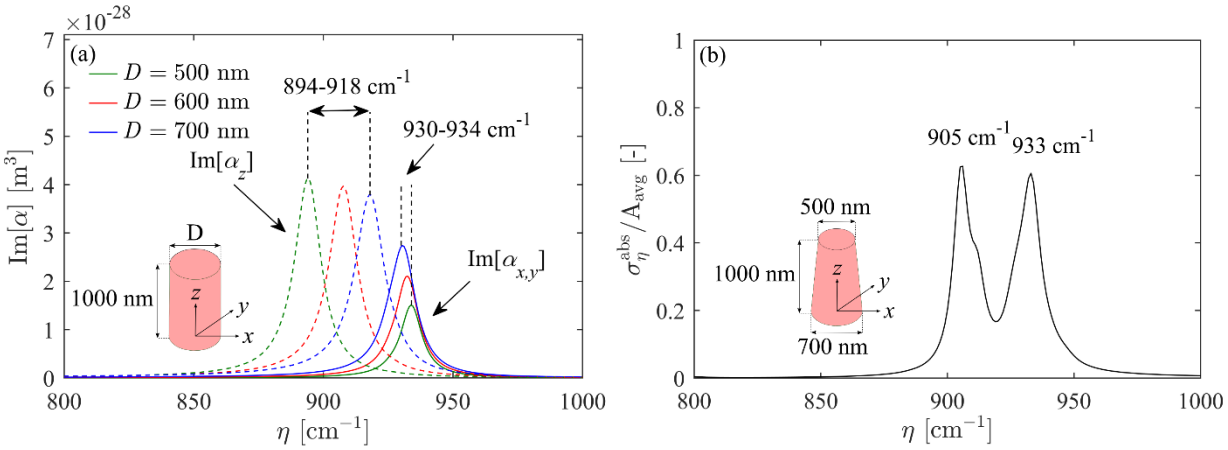

Figure 2-1 Isolated nanopillar.
(a) The imaginary part of the longitudinal and transversal polarizability of 6H-SiC cylindrical nanopillars for three diameters of 500, 600, and 700 nm. (b) The absorption cross section for a frustum-shaped nanopillar normalized by a circular cross section with an average diameter of 600 nm.

Next, thermal emission from an array of nanopillars with an interpillar spacing, d, is studied. The spectral, directional emissivity of a free-standing array of nanopillars with a square lattice [see the inset of Fig. 2-2(a)] at T = 400°C is simulated for various d ranging from 2300 nm to 50 nm. The spectral, directional emissivity, ε'_η, is found from the field amplitude reflection and transmission coefficients as $\varepsilon'_\eta = \frac{1}{2}\sum_{\gamma=\mathrm{TE,TM}}\left(1-\left|R^\gamma_\eta\right|^2-\left|T^\gamma_\eta\right|^2\right)$, where η refers to the

wavenumber, γ shows the polarization state (TE and TM stand for the transverse electric and magnetic polarizations, respectively), and R_η^γ and T_η^γ are the reflection and transmission coefficients, respectively [31]. The terms R_η^γ and T_η^γ are simulated using the SCUFF-TRANSMISSION module of the SCUFF-EM electromagnetic solver [30,32]. Figure 2-2(a) shows the spectral, normal emissivity of the nanopillar array for the considered interpillar spacing. The longitudinal and transversal dipolar LSPhs of the isolated nanopillars are observed in the emissivity spectrum of the array for all considered interspacing values. When d = 2300 nm, the electromagnetic interactions of neighboring nanopillars are weak and the spectral locations of the longitudinal and transversal LSPhs (906, 912, and 933 cm^{-1}) are almost the same as those for isolated nanopillars. The emissivity of the array for d = 2300 nm is very low ($\varepsilon'_{\eta,\max}$ ~ 0.2). As d decreases, the emissivity of the array significantly enhances in a non-monotonic manner. The emissivity increases as d decreases to ~150 nm, and then it decreases when d is further reduced to 50 nm. The non-monotonic variation of the emissivity with d can be explained by considering that there are two competing effects on the far-field thermal emission as d decreases. On one hand, the emitting volume per unit surface area of the array increases, but on the other hand, the dipole moments of the emitters decrease due to the near-field interactions between the nanopillars. As it is seen from Eq. A.3 of Appendix A, the emitted energy from a nanopillar is proportional to its dipole moment. The dipole moment of nanopillar i of the array, $\mathbf{p}_i$, can qualitatively be approximated as [33]:

$$\mathbf{p}_i = \alpha_i \left(\frac{\mathbf{p}_i^{fl}}{\varepsilon_0 V(\varepsilon-1)} + \frac{k_0^2}{\varepsilon_0} \sum_{j \neq i} \overline{\overline{\mathbf{G}}}_{ij} \cdot \mathbf{p}_j \right) \tag{2.1}$$

where $\mathbf{p}_i^{fl}$ is the thermally fluctuating dipole moment of the nanopillars, ε_0 is the permittivity of the free space, and $\overline{\overline{\mathbf{G}}}_{ij}$ is the free space electric Green's function between nanopillars i and j

[33]. In Eq. 2.1, the sum of the two terms in the parentheses indicates the total electric field in nanopillar i. The first term is the thermal field of the nanopillar, while the second term represents the electric field generated at nanopillar i due to emission from all other nanopillars of the array. Equation 2.1 shows that the interactions between the nanopillars, which is represented by the free space Green's function $\overline{\overline{\mathbf{G}}}_{ij}$, affect the dipole moments of the nanopillars, $\mathbf{p}_i$. The free space Green's function can be decomposed into three far-field, middle-field, and near-field components (See Sec. A.3 of Appendix A) [34]. As an example, these three components for the real part of $G_{ij,yy}$ are shown versus d in Fig. 2-2(b) at $\eta = 903$ cm^{-1}. It is seen that at d = 2300 nm, $G_{ij,yy}$ is mostly dominated by the middle-field contribution. As d decreases, the absolute values of the far-field, middle-field, and near-field components increase as $\frac{1}{d}$, $\frac{1}{d^2}$, and $\frac{1}{d^3}$, respectively (See Sec. A.3 of Appendix A). The enhancement of the near-field component with decreasing d is much stronger than that for the middle and far fields, such that $G_{ij,yy}$ is totally dominated by the near-field contribution when $d < 1400$ nm. Figure 2-2(d) also shows that the near-field interactions between nanopillars are very significant when $d \lesssim 300$ nm. The initial enhancement of the emissivity with decreasing d from 2300 nm to ~150 nm is driven by the increase of the volume of the emitters. As d decreases further to 50 nm, the strong near-field interactions reduce $\mathbf{p}_i$ and thus the emissivity of the array. The spectral locations of the LSPh peaks do not shift significantly when d reduces to ~300 nm. However, when $d < 300$ nm, the LSPh peaks redshift due to the strong near-field interactions of the nanopillars.

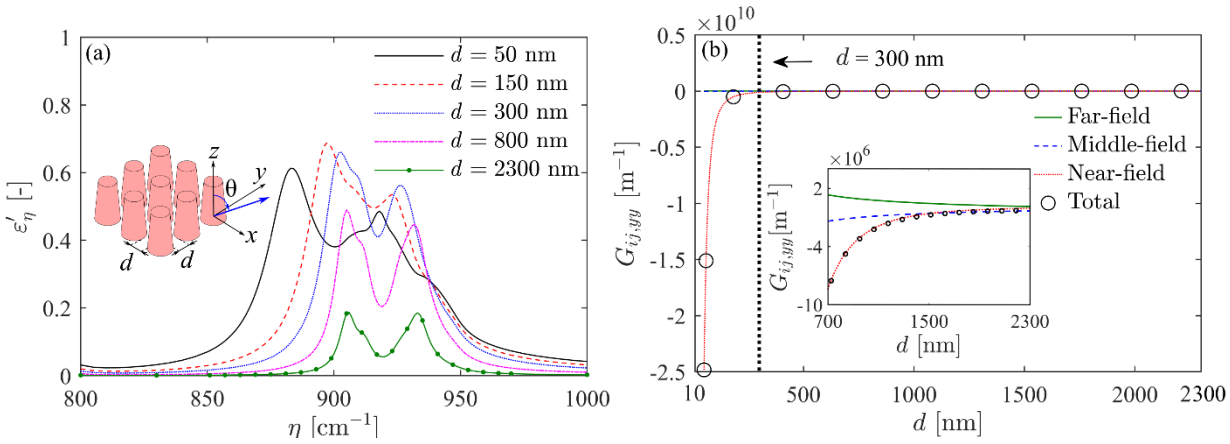

Figure 2-2 Free-standing array of nanopillars.
(a) The spectral, normal emissivity for a free-standing array of 6H-SiC frustum-shaped nanopillars. (b) The real part of the yy componet of the free space Green's function between two points i and j separated by a distance d along the y axis.

The emissivity of the array can be enhanced further by exploiting thermal emission of the SPhPs from a SiC substrate on which the nanopillar array can be fabricated. As mentioned before, the SPhPs are evanescent in the free space and thus do not contribute to the far-field thermal emission. At a given wavenumber, the parallel component of the wavevector for the SPhP modes is determined from the dispersion relation as $k_\rho^{\mathrm{SPhP}} = k_0\sqrt{\frac{\varepsilon}{\varepsilon+1}}$ [2]. When a shallow grating is added to a flat SiC surface, k_ρ^{SPhP} is modified as $k_{\rho,mn}^{\mathrm{SPhP}} = k_\rho^{\mathrm{SPhP}} \pm m\frac{2\pi}{\Lambda} \pm n\frac{2\pi}{\Lambda}$, where m and n are integers [8]. For long-pitch arrays with $\Lambda > \frac{\lambda}{2}$, $k_{\rho,mn}^{\mathrm{SPhP}}$ can reduce to values below k_0 and thus the SPhP modes can become propagative in certain directions in the free space [8]. Short-pitch shallow gratings with $\Lambda < \frac{\lambda}{2}$, which are zero order, cannot sufficiently reduce $k_{\rho,m}^{\mathrm{SPhP}}$ to below k_0 (See Sec. A.4 of Appendix A). However, when zero-order gratings are deep, a broad gap appears in the photonic structure of the material, and a new, dispersion-less electromagnetic mode emerges within this band gap [35,36]. This new electromagnetic mode, referred to as the hybrid waveguide-SPhP resonance [35,36], corresponds to highly localized electromagnetic field in the narrow

spaces between nanopillars and results in a new peak in far-field thermal radiation. Unlike SPhP modes coupled to the free space using long-pitch gratings, the dispersion-less waveguide-SPhP mode enhances thermal emission in all directions which is beneficial for thermal management applications. Figure 2-3(a) shows the spectral, normal emissivity for on-substrate SiC arrays. The additional peak observed in the emissivity spectrum corresponds to thermal emission of the hybrid waveguide-SPhP mode. The dipole moments of the nanopillars are also affected in the presence of the electric field thermally radiated from the substrate, $\mathbf{E}^{\mathrm{sub}}$. The substrate field $\mathbf{E}^{\mathrm{sub}}$, should be added to the terms in the parentheses in Eq. 2.1 when using this equation for analyzing the dipole moments of the on-substrate arrays. The existence of $\mathbf{E}^{\mathrm{sub}}$ in Eq. 2.1 can modify the spectrum and magnitude of the dipole moments. As a result, the LSPh peaks of the on-substate array are redshifted relative to the ones of the free-standing array. As d decreases, the waveguide-SPhP mode redshifts toward the longitudinal LSPhs. When d = 300 nm, the spectral overlap of these two modes results in blackbody thermal emission ($\varepsilon_\eta' \sim 1$) from the array in the spectral band of 910 – 916 cm^{-1}. As it was mentioned before, the enhancement of emissivity is not directional. Figure 2-3(b) shows a color plot of ε_η' for the array with d = 300 nm. It is seen that the designed array has significantly high thermal emission in a spectral band spanning several wavelengths and for angles as large as 75° from the surface normal. The non-directional thermal emission from the array, which is also observed for smaller interpillar spacing of d = 50 nm, is due to dispersion-less nature of the LSPh and waveguide-SPhP modes.

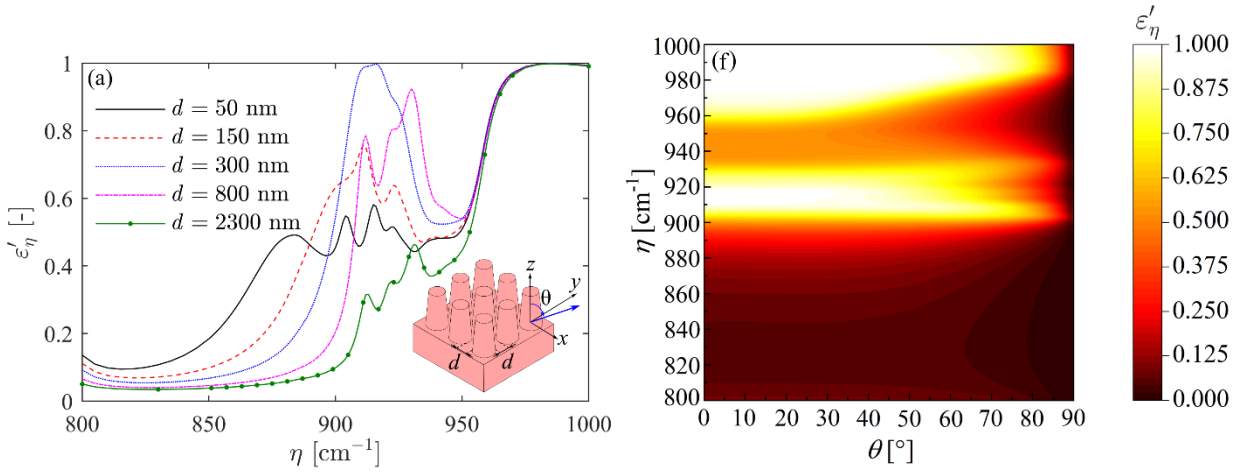

Figure 2-3 On-substrate array of nanopillars.
(a) The spectral, normal emissivity of a 6H-SiC frustum-shaped nanopillar array on a 6H-SiC substrate. (b) A color plot of the spectral, directional emissivity of the on-substrate array of 6H-SiC frustum-shaped nanopillars, as shown in Fig. 2-3(a), with d = 300 nm.

To experimentally demonstrate enhanced far-field thermal radiation from short-pitch arrays, the spectral, directional emissivity of an array of 6H-SiC frustum-shaped nanopillars with an interpillar spacing of d = 300 nm is measured. The nanopillars are fabricated on a 1 × 1 cm^2 surface area of a 430-μm-thick 6H-SiC substrate. The nanopillars are defined on the substrate using inductively-coupled plasma reactive ion etching (ICP-RIE). An array of patterned chromium circles is used as an etch hard mask, which is defined using electron beam lithography (fabrication details in Sec. A.5 of Appendix A). The erosion of the chromium mask in the radial direction during the etching process causes a frustum, rather than cylindrical, shape for the nanopillars. A scanning electron microscope (SEM) image and a brightfield microscope image of the fabricated sample are shown in Figs. 2-4(a) and (b), respectively. A setup for measuring emissivity is also established [Fig. 2-4(c)]. In this setup, the sample is mounted on an aluminum stage using a nickel base metal adhesive (Durabond, 952FS). The stage holds a cartridge heater (Watlow Firerod) inside, and it is assembled on a rotary stage (Standa Inc., 8MR174-11-20) which is used for directional measurements. The sample is heated up to 400°C. The temperature of the sample is

determined by knowing that the emissivity of SiC at the Christiansen wavenumber (990.1 cm^{-1}) is 1 [8]. Thermal emission by the heated sample ($I_{S\eta}$) is directed toward a Fourier Transform Infrared (FTIR) spectrometer (Thermo Fisher Scientific, Nicolet iS50) equipped with a mercury-cadmium-telluride detector (Thermo Fisher Scientific, MCT-A/CdTe) using flat (Thorlabs, PFSQ20-03-M03) and parabolic (Thorlabs, MPD269-M03) mirrors. An iris is placed in front of the sample to limit the collection angle. Thermal emission by a blackbody (ISDC, IR-563) located at the same optical path toward the FTIR spectrometer as the sample, is also collected ($I_{BB,\eta}$). The background thermal radiation ($I_{E,\eta}$) is recorded when both the heater and the blackbody are turned off, and it is subtracted from the sample and blackbody emissions. Finally, the spectral, directional emissivity is found as $\varepsilon'_\eta = \frac{(I_{S,\eta} - I_{E,\eta})}{(I_{BB,\eta} - I_{E,\eta})}$. Figure 2-4(d) shows the measured emissivity for the fabricated sample at θ = 0 to 60° with respect to the surface normal. As it was predicted by numerical simulations, the sample shows modest angular dependence. The normal emissivity measured for a bare SiC substrate is also shown in Fig. 2-4(d) for comparison. The presence of the array on the substrate increases the total (spectrally-integrated), normal emissivity in the spectral band of 800 – 980 cm^{-1} more than 100% without diminishing the large emissivity of the substrate between 980 – 1000 cm^{-1}. It is seen that the measured emissivity is slightly lower than those theoretically predicted in Fig. 2-3(a). Additionally, the theoretical large-emissivity band in Fig. 2-3(a) is split into two distinct peaks in the measurements, and the peaks are shifted relative to the simulations (911 and 916 cm^{-1} are predicted theoretically, while 902 and 923 cm^{-1} are measured). This difference is attributed to the surface damage during the ICP-RIE [14] as well as the difference between the fabricated and modeled geometries. The SEM images of the fabricated sample show non-uniformity in the shape and spacing of the nanopillars as well as the presence of a trench around the nanopillars [see Fig 2-4(a)]. As it is seen from Fig. 2-3(a), the emissivity of the array drops

below 1 with decreasing and increasing d from 300 nm. The splitting and shifts of the peaks are mostly due to the existence of the trench. Figure 2-4(e) shows the predicted emissivity in the presence of a conical trench of height and width 50 nm around the nanopillars. The splitting of the large-emissivity band into two peaks is theoretically predicted, and the simulated wavenumbers of the peaks in the presence of the trench (906 and 921 cm^{-1}) are close to the experimentally measured values (902 and 923 cm^{-1}).

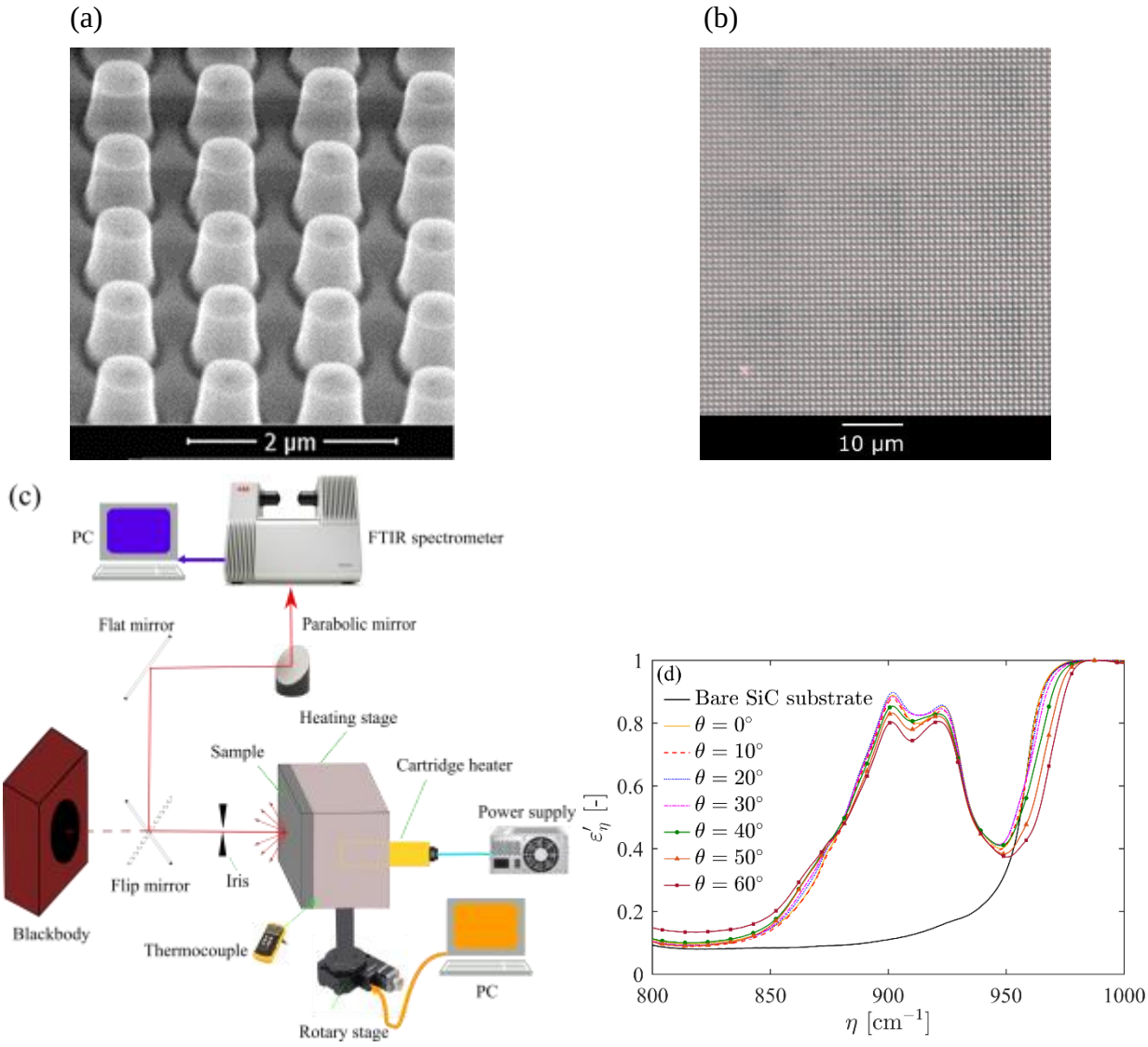

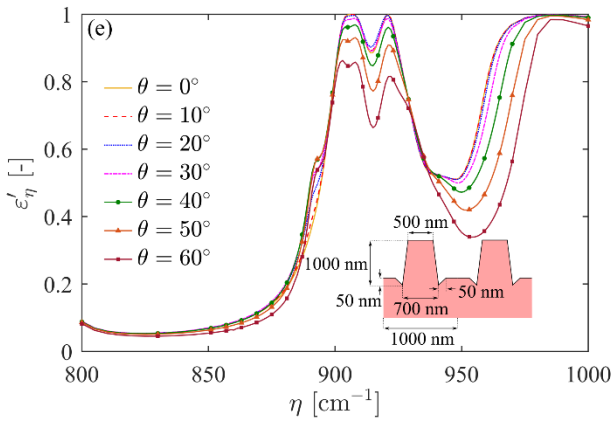

Figure 2-4 Fabrication, measurements, and experimental results.
(a) An SEM image and (b) a brightfield microscope image of the fabricated 6H-SiC nanopillar array. (c) A schematic of the setup established for measuring the spectral, directional emissivity. (d) The spectral, directional emissivity experimentally measured for the nanopillar array shown in Fig. 2-4(a). (e) The theoretically predicted spectral, directional emissivity for the nanopillar array shown in Fig. 1e and in the presence of a trench around the nanopillars.

2.4 Conclusions

To summarize, the physics underlying far-field thermal emission from zero-order arrays of SiC nanopillars was studied theoretically and experimentally. It was shown that reducing the interpillar spacing in an array of 6H-SiC nanopillars to the nanometer scale increases the emissivity due to the increase in the volume of thermal emitters. However, when the interpillar spacing is reduced below ~300 nm, the near-field interactions between the nanopillars reduce their dipole moments and eventually causes a drop in the emissivity despite the increased emitting volume. It was also demonstrated that the array can be engineered such that the LSPhs emitted by the nanopillars spectrally overlap the waveguide-SPhP resonance of the array resulting in blackbody emission in a spectral region in the Reststrahlen band. Our study unveils the physical mechanisms of far-field thermal radiation from zero-order nanostructures of polaritonic materials and demonstrates that nanoengineering surface phonons provides a great opportunity for increasing far-field thermal emission.

2.5 Acknowledgement

This work is financially supported by the National Science Foundation under Grant No. CBET-1804360. The authors thank Stephen Abbadessa for his assistance with implementing the experimental setup for measuring emissivity.

2.6 References

[1] Zhang, Z.M., 2020. *Nano/microscale heat transfer*. Cham: Springer.

[2] Joulain, K., Mulet, J.P., Marquier, F., Carminati, R. and Greffet, J.J., 2005. Surface electromagnetic waves thermally excited: Radiative heat transfer, coherence properties and Casimir forces revisited in the near field. *Surface Science Reports, 57*(3-4), pp.59-112.

[3] Foteinopoulou, S., Devarapu, G.C.R., Subramania, G.S., Krishna, S. and Wasserman, D., 2019. Phonon-polaritonics: enabling powerful capabilities for infrared photonics. *Nanophotonics, 8*(12), pp.2129-2175.

[4] Caldwell, J.D., Lindsay, L., Giannini, V., Vurgaftman, I., Reinecke, T.L., Maier, S.A. and Glembocki, O.J., 2015. Low-loss, infrared and terahertz nanophotonics using surface phonon polaritons. *Nanophotonics, 4*(1), pp.44-68.

[5] Le Gall, J., Olivier, M. and Greffet, J.J., 1997. Experimental and theoretical study of reflection and coherent thermal emissionby a SiC grating supporting a surface-phonon polariton. *Physical Review B, 55*(15), p.10105.

[6] Greffet, J.J., Carminati, R., Joulain, K., Mulet, J.P., Mainguy, S. and Chen, Y., 2002. Coherent emission of light by thermal sources. *Nature, 416*(6876), pp.61-64.

[7] Dahan, N., Niv, A., Biener, G., Gorodetski, Y., Kleiner, V. and Hasman, E., 2007. Enhanced coherency of thermal emission: Beyond the limitation imposed by delocalized surface waves. *Physical Review B—Condensed Matter and Materials Physics, 76*(4), p.045427.

[8] Arnold, C., Marquier, F., Garin, M., Pardo, F., Collin, S., Bardou, N., Pelouard, J.L. and Greffet, J.J., 2012. Coherent thermal infrared emission by two-dimensional silicon carbide gratings. *Physical Review B—Condensed Matter and Materials Physics, 86*(3), p.035316.

[9] Hasman, E., Kleiner, V., Dahan, N., Gorodetski, Y., Frischwasser, K. and Balin, I., 2012. Manipulation of thermal emission by use of micro and nanoscale structures.

[10] Hervé, A., Drévillon, J., Ezzahri, Y., Joulain, K., Meneses, D.D.S. and Hugonin, J.P., 2016. Temperature dependence of a microstructured SiC coherent thermal source. *Journal of Quantitative Spectroscopy and Radiative Transfer, 180*, pp.29-38.

[11] Chalabi, H., Alù, A. and Brongersma, M.L., 2016. Focused thermal emission from a nanostructured SiC surface. *Physical Review B*, *94*(9), p.094307.

[12] Starko-Bowes, R., Dai, J., Newman, W., Molesky, S., Qi, L., Satija, A., Tsui, Y., Gupta, M., Fedosejevs, R., Pramanik, S. and Xuan, Y., 2018. Dual-band quasi-coherent radiative thermal source. *Journal of Quantitative Spectroscopy and Radiative Transfer*, *216*, pp.99-104.

[13] Caldwell, J.D., Glembocki, O.J., Francescato, Y., Sharac, N., Giannini, V., Bezares, F.J., Long, J.P., Owrutsky, J.C., Vurgaftman, I., Tischler, J.G. and Wheeler, V.D., 2013. Low-loss, extreme subdiffraction photon confinement via silicon carbide localized surface phonon polariton resonators. *Nano letters*, *13*(8), pp.3690-3697.

[14] Chen, Y., Francescato, Y., Caldwell, J.D., Giannini, V., Maß, T.W., Glembocki, O.J., Bezares, F.J., Taubner, T., Kasica, R., Hong, M. and Maier, S.A., 2014. Spectral tuning of localized surface phonon polariton resonators for low-loss mid-IR applications. *Acs Photonics*, *1*(8), pp.718-724.

[15] Razdolski, I., Chen, Y., Giles, A.J., Gewinner, S., Schöllkopf, W., Hong, M., Wolf, M., Giannini, V., Caldwell, J.D., Maier, S.A. and Paarmann, A., 2016. Resonant enhancement of second-harmonic generation in the mid-infrared using localized surface phonon polaritons in subdiffractional nanostructures. *Nano letters*, *16*(11), pp.6954-6959.

[16] Gubbin, C.R., Martini, F., Politi, A., Maier, S.A. and De Liberato, S., 2016. Strong and coherent coupling between localized and propagating phonon polaritons. *Physical review letters*, *116*(24), p.246402.

[17] Gubbin, C.R., Maier, S.A. and De Liberato, S., 2017. Theoretical investigation of phonon polaritons in SiC micropillar resonators. *Physical review B*, *95*(3), p.035313.

[18] Gubbin, C.R., Berte, R., Meeker, M.A., Giles, A.J., Ellis, C.T., Tischler, J.G., Wheeler, V.D., Maier, S.A., Caldwell, J.D. and De Liberato, S., 2019. Hybrid longitudinal-transverse phonon polaritons. *Nature communications*, *10*(1), p.1682.

[19] Lu, G., Gubbin, C.R., Nolen, J.R., Folland, T.G., Diaz-Granados, K., Kravchenko, I.I., Spencer, J.A., Tadjer, M.J., Glembocki, O.J., De Liberato, S. and Caldwell, J.D., 2021. Collective phonon–polaritonic modes in silicon carbide subarrays. *ACS nano*, *16*(1), pp.963-973.

[20] Schuller, J.A., Taubner, T. and Brongersma, M.L., 2009. Optical antenna thermal emitters. *Nature Photonics*, *3*(11), pp.658-661.

[21] Wang, T., Li, P., Chigrin, D.N., Giles, A.J., Bezares, F.J., Glembocki, O.J., Caldwell, J.D. and Taubner, T., 2017. Phonon-polaritonic bowtie nanoantennas: controlling infrared thermal radiation at the nanoscale. *Acs Photonics*, *4*(7), pp.1753-1760.

[22] Neuner, B., Wu, C., Eyck, G.T., Sinclair, M., Brener, I. and Shvets, G., 2013. Efficient infrared thermal emitters based on low-albedo polaritonic meta-surfaces. *Applied Physics Letters*, *102*(21).

[23] Lu, G., Gubbin, C.R., Nolen, J.R., Folland, T., Tadjer, M.J., De Liberato, S. and Caldwell, J.D., 2021. Engineering the spectral and spatial dispersion of thermal emission via polariton–phonon strong coupling. *Nano letters*, *21*(4), pp.1831-1838.

[24] Lu, G., Nolen, J.R., Folland, T.G., Tadjer, M.J., Walker, D.G. and Caldwell, J.D., 2020. Narrowband polaritonic thermal emitters driven by waste heat. *ACS omega*, *5*(19), pp.10900-10908.

[25] Enoch, S. and Bonod, N. eds., 2012. *Plasmonics: from basics to advanced topics* (Vol. 167). Springer.

[26] Chen, D., Dong, J., Yang, J., Hua, Y., Li, G., Guo, C., Xie, C., Liu, M. and Liu, Q., 2018. Realization of near-perfect absorption in the whole reststrahlen band of SiC. *Nanoscale*, *10*(20), pp.9450-9454.

[27] Silva, A.O. and Costa, J.C., 2014. Retrieving the Effective Permittivity of an Optical Metamaterial Structured with Metallic Cylindrical Nanorods-An Analytical Approach Based on the Calculation of the Depolarization Field. *Journal of Microwaves, Optoelectronics & Electromagnetic Applications*, *13*.

[28] Zare, S., Pouria, R. and Edalatpour, S., 2021. Validity of the effective medium theory for modeling near-field thermal emission by nanowire arrays. *Journal of Quantitative Spectroscopy and Radiative Transfer*, *261*, p.107482.

[29] Reid, M. T. H.; Johnson, S. G. Solving electromagnetic scattering problems with scuff-scatter http://homerreid.github.io/scuff-em-documentation/applications/scuff-scatter/scuff-scatter/.

[30] Reid, M.H. and Johnson, S.G., 2015. Efficient computation of power, force, and torque in BEM scattering calculations. *IEEE Transactions on Antennas and Propagation*, *63*(8), pp.3588-3598.

[31] Edalatpour, S. and Francoeur, M., 2013. Size effect on the emissivity of thin films. *Journal of Quantitative Spectroscopy and Radiative Transfer*, *118*, pp.75-85.

[32] Reid, M. T. H.; Johnson, S. G. Fresnel Scattering http://homerreid.github.io/scuff-em-documentation/tests/FresnelScattering/FresnelScattering/.

[33] Edalatpour, S., Čuma, M., Trueax, T., Backman, R. and Francoeur, M., 2015. Convergence analysis of the thermal discrete dipole approximation. *Physical Review E*, *91*(6), p.063307.

[34] Arnoldus, H.F., 2001. Representation of the near-field, middle-field, and far-field electromagnetic Green's functions in reciprocal space. *JOSA B*, *18*(4), pp.547-555.

[35] Garcia-Vidal, F.J., Sanchez-Dehesa, J., Dechelette, A., Bustarret, E., Lopez-Rios, T., Fournier, T. and Pannetier, B., 1999. Localized surface plasmons in lamellar metallic gratings. *Journal of Lightwave technology*, *17*(11), p.2191.

[36] Hooper, I.R. and Sambles, J.R., 2002. Dispersion of surface plasmon polaritons on short-pitch metal gratings. *Physical Review B, 65*(16), p.165432.

Chapter 3

Broadband and Omni-Directional Enhancement of Emissivity Enabled by Thermal Radiation of Mie Resonances

This chapter has been submitted to be published in ACS Photonics as an article. Coauthors of this paper are Ramin Pouria, Dhan Cardinal, Philippe K. Chow, and Sheila Edalatpour.

3.1 Abstract

Enhancing the emissivity of materials in a broadband and omni-directional manner is crucial for thermal management applications. The emissivity of dielectric media is commonly enhanced by microengineering the material to thermally emit localized surface phonons (LSPhs). The LSPhs resonantly enhance emissivity at selective wavelengths inside the Reststrahlen band of the material, which usually spans a limited spectral range and can be distant from the wavelength of peak thermal radiation. Dielectric media can also emit Mie resonances, which are not limited to a spectral range, and thus can potentially be used for broadband enhancement of emissivity. In this study, we analyze thermal emission of Mie resonance from individual and arrays of microcuboids of 6H-SiC. Based on this analysis, we design a periodic array of microcuboids for broadband and omni-directional emissivity enhancement. The designed array increases thermal radiation from a flat, unpatterned 6H-SiC substrate at the normal direction from 67% to 91% of a blackbody, while demonstrating enhanced emissivity in a wide angular range. The designed array is fabricated using the e-beam lithography and reactive ion etching, and the broadband and omni-directional enhancement of emissivity by capitalizing on Mie resonances is experimentally demonstrated. This study shows the potential of Mie resonances for thermal management applications and provides a guide for designing efficient thermal emitters.

3.2 Introduction

Increasing the emissivity of dielectric materials in a wide spectral range where blackbody thermal radiation is non-negligible is of vital importance for thermal management, electronic cooling, and developing efficient heat sinks. So far, most of the studies on enhancing the emissivity of dielectric materials capitalize on thermal excitation of surface phonon polaritons (SPhPs) [1-8] or localized surface phonons (LSPhs) [9-21]. However, surface phonons are only available in a small spectral band relative to the blackbody emission band, referred to as the Reststrahlen band. Additionally, the Reststrahlen band of the dielectric media are commonly far from the dominant wavelength of blackbody thermal radiation, where most of the emitted energy is spectrally located. For example, we measured the Reststrahlen band of 6H-silicon carbide (6H-SiC) at 400°C to be 10.4 to 12.7 μm, which contains only 6.8% of the blackbody thermal radiation at this temperature. As such, an enhancement of emissivity in the Reststrahlen band does not increase the total (spectrally integrated) emissivity appreciably. In addition to the surface phonons, dielectric materials can thermally emit Mie resonances which are not confined to a limited spectral region. Thermal radiation of Mie resonances can enhance the emissivity of the material significantly. Therefore, engineering dielectric media to support various Mie resonances throughout the blackbody emission band is a promising mechanism for achieving large emissivity in a broad spectral range. Despite this promise, so far Mie resonances have not been capitalized on for broadband enhancement of emissivity. Indeed, the studies on thermal radiation of Mie resonances are very sparse. Using an approximate method, namely effective medium theory, it has been theoretically shown that the tungsten nanoparticle Mie resonators embedded in a SiO_2 film can achieve an emissivity of ~0.8 in a spectral range of 0.5 – 1.5 μm [22]. A narrowband and spectrally selective thermal emitter enabled by overlapping Mie resonances due to the electric and magnetic

dipoles was designed and demonstrated [23]. The designed emitter demonstrated a peak emissivity of 0.78 at 250°C located at 12.9 μm, which is distant from the peak of blackbody thermal radiation at this temperature (= 5.5 μm). In this paper, we study the emissivity of individual and periodic arrays of 6H-SiC Mie resonators both numerically and experimentally. Using non-approximate numerical simulations, we demonstrate that dielectric media can be engineered to thermally emit several Mie resonances throughout the blackbody emission band. We show that an array of Mie resonators can enhance the emissivity of the material up to the blackbody limit in a wide spectral range due to thermal radiation of Mie resonances and coupling near-field thermal radiation from the substrate to the far field. Our simulations predict that fabricating the periodic array on the 6H-SiC substrate enhances the total (spectrally integrated over 2 to 16 μm, where 92% of blackbody thermal radiation is located), normal emissivity from 0.67 to 0.91. Additionally, the emissivity enhancement is observed for a wide angular range, which is crucial for maximal energy emission. The emissivity enhancement for the above-mentioned array of Mie resonators is experimentally demonstrated by measuring the spectral, directional emissivity at a temperature of 400°C and an angular range of 0 to 60° with respect to the surface normal. The enhanced emissivity measured for the Mie-resonator array compared to the one for an unpatterned substrate demonstrates that Mie resonances are promising for designing broadband and omnidirectional thermal emitters.

3.3 Problem Description, Results, and Discussion

6H-SiC is considered as the dielectric material for this study, since it is thermally and chemically stable at high temperatures and has a large refractive index in the IR. A cubical geometry is selected for the Mie resonators as fabricating microcubes is less challenging than spheres and cylinders. The temperature is fixed at T = 400°C throughout this study. To analyze

the Mie resonances supported by the 6H-SiC microcubes, the scattering cross section, σ_s, for a microcube with a side length of L illuminated by an incident electric, $\mathbf{E}_{\text{inc}}$, as shown in the inset of Fig. 3-1(a), is modelled using the Wave Optics Module of COMSOL Multiphysics software. The incident electric field has a magnitude of 1 V/m, while it is polarized along the x-axis and travels in the negative z-direction [see the inset of Fig. 3-1(a)]. The dielectric function of 6H-SiC is measured at 400°C [21] and used for these simulations. The scattering cross section normalized by the physical cross section of the microcube, σ_s/L^2, is shown for three microcubes with side lengths of L = 1, 2, and 3 μm in Figs. 4-1(a)-(c), respectively. A broad spectral range of 2 - 16 μm, which contains 92% of blackbody radiation at 400°C, is considered. The spectra of σ_s/L^2 in Figs. 4-1(a)-(c) show several peaks. To identify the origin of these peaks, the scattering cross section is decomposed into contributions from the electric dipole (ED), magnetic dipole (MD), electric quadrupole (EQ), and magnetic quadrupole (MQ) modes. The procedure used for the multipole decomposition of the scattering cross section is detailed in Ref. [21,24]. Figure 3-1(a) shows that σ_s/L^2 for the microcube with L = 1 μm has four peaks which are located at 2.1, 3.1, 11.2, and 11.5 μm. The peaks at 2.1 and 3.1 μm, which are outside the Reststrahlen band of 6H-SiC (10.4 μm – 12.7 μm at 400°C), are due to the excitation of Mie resonances. The multipole decomposition of σ_s, presented in Fig. 3-1(a), shows that the Mie resonance at 2.1 μm is due to the combined contribution from EQ and MQ modes, while the Mie resonance at 3.1 μm is due to the ED and MD modes. The spatial distribution of electric field induced within the microcube is also modeled at these two wavelengths and is shown in Fig. 3-1(d). The electric field distributions in Fig. 3-1(d) demonstrate induced MQ-EQ and ED-MD modes within the microcubes at 2.1 and 3.1 μm. The peaks at 11.2 and 11.5 μm are located within the Reststrahlen band and are due to excitation of the LSPhs. The multipole decomposition of σ_s shows that these two LSPh peaks are due to the

excitation of ED mode. The charge density induced within the microcube is modeled at 11.2 and 11.5 μm and shown in Fig. 3-1(e). The charge density distributions in Fig. 3-1(e) demonstrate the excitation of transverse EDs inside the microcube at these two wavelengths.

For the microcube with $L = 2$ μm, the normalized scattering cross section, σ_s/L^2, and its multipole decomposition are shown in Fig. 3-1(b). As L increases to 2 μm, the spectral locations of the EQ-MQ and ED-MD Mie resonances redshift from 2.1 and 3.1 μm to 4.2 and 5.9 μm, respectively, and new Mie resonances appear in the considered spectral band. When L = 2 μm, the number of peaks and shoulders in the spectrum of σ_s/L^2 increases from four to twelve, with ten being due to the Mie resonances and two being due to the LSPhs. The spectral features due to the Mie resonances are located at 2.4 (MD), 2.9 (ED), 3.4 (EQ), 4.2 (EQ-MQ), 5.9 (ED-MD) and 6.3 (ED-MD), 6.6 (ED-MD), 12.8 (ED), 13.1 (ED), and 13.6 μm (MD), while the LSPh peaks are observed at 11.3 (ED) and 11.6 μm (ED). The normalized scattering cross section for a case when the side length of the microcube is further increased to L = 3 μm is shown in Fig. 3-1(c). The most notable effect of increasing L to 3 μm on σ_s/L^2 is further redshift of the Mie resonances. Based on the spectra of σ_s/L^2 shown in Figs. 1a-c, a microcube with L = 2 μm is desirable as a thermal emitter at 400°C as this microcube has strong Mie resonances around the peak blackbody radiation occurring at 4.3 μm. The scattering cross section spectra in Fig. 1a-c are utilized for identifying the Mie and LSPh resonances supported by the microcubes. However, the strength of thermal emission of the supported Mie and LSPh resonances also depends on the extinction coefficient, κ_λ, of 6H-SiC at the spectral locations of these resonances. The absorption cross section, σ_a, can be used to qualitatively study the strength of the Mie and LSPh resonances in the spectrum of emissivity for an individual microcube.

(a)

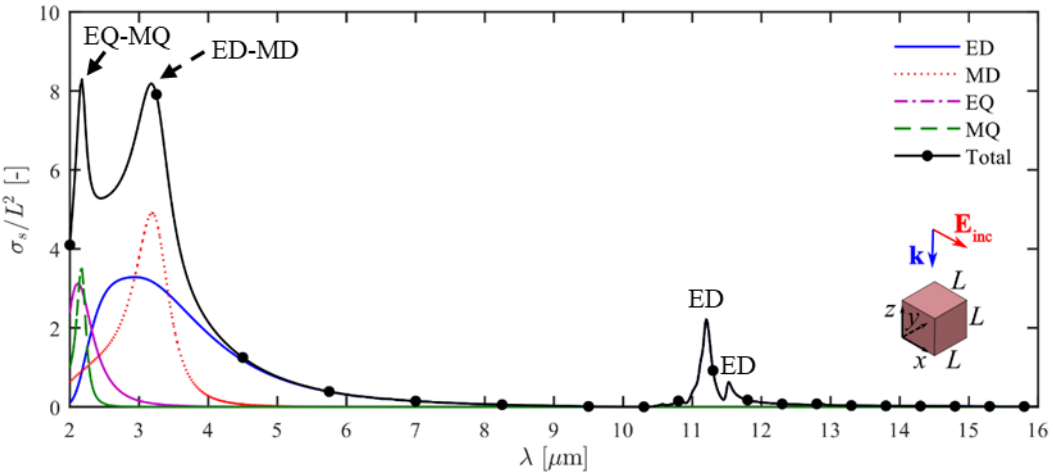
EQ-MQ
ED-MD
ED
ED
ED
MD
EQ
MQ
Total
$\mathbf{E}_{inc}$
k
L
L
L
z
y
x
σ_s/L^2 [-]
λ [μm]

(b)

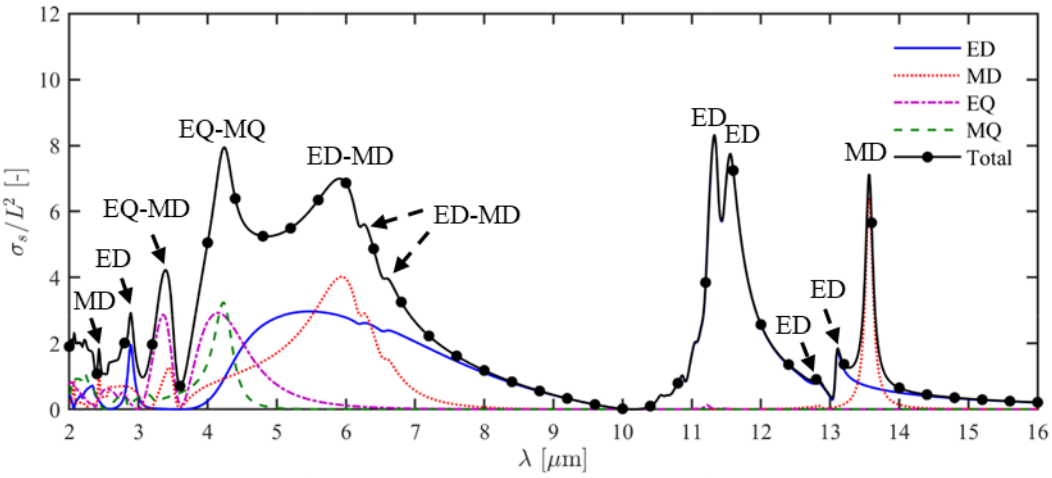
EQ-MQ
ED-MD
EQ-MD
ED
MD
ED-MD
ED
ED
MD
ED
ED
ED
MD
EQ
MQ
Total
σ_s/L^2 [-]
λ [μm]

(c)

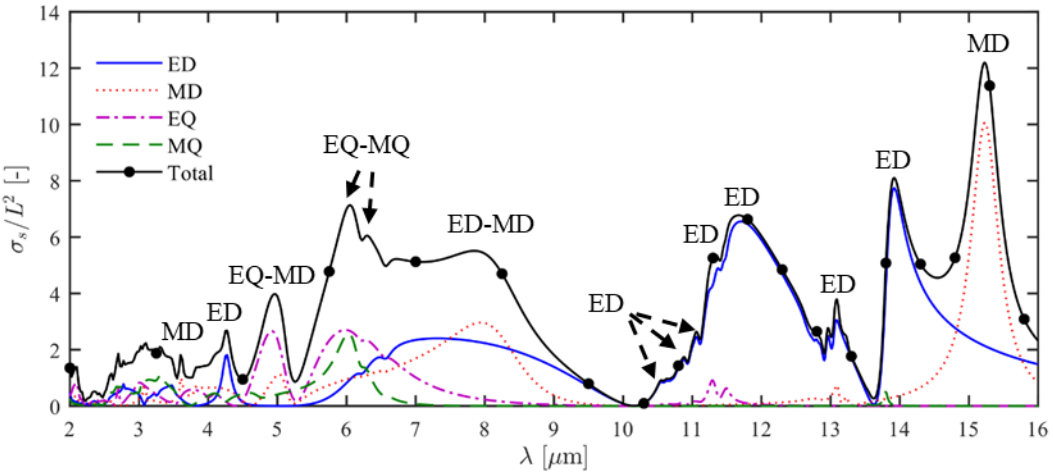
MD
ED
EQ-MD
EQ-MQ
ED-MD
ED
ED
ED
ED
ED
MD
ED
MD
EQ
MQ
Total
σ_s/L^2 [-]
λ [μm]

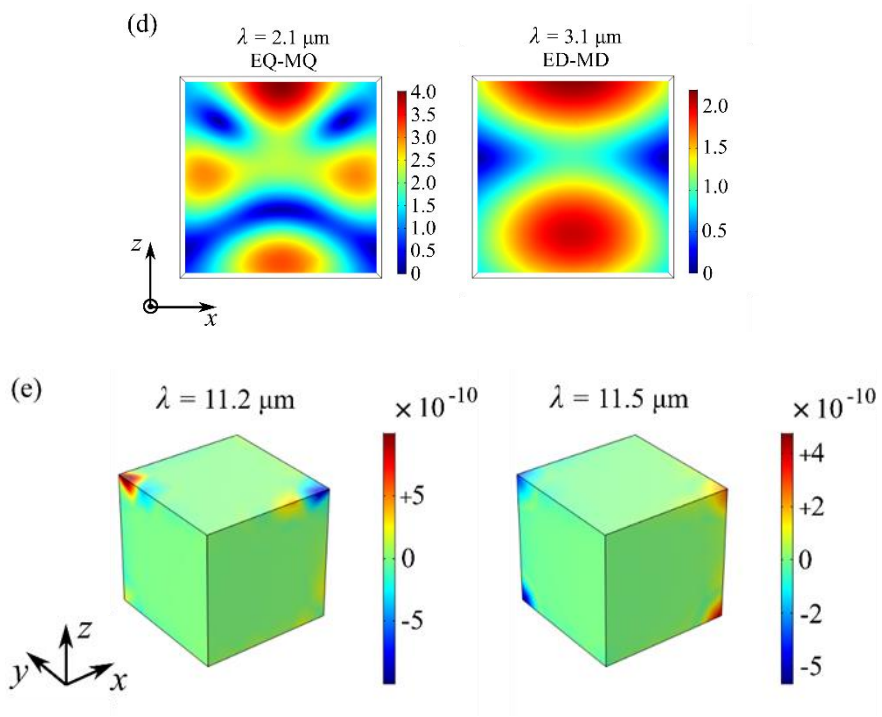

Figure 3-1 scattering cross-section, electric field distribution, and surface charge density of a single 6H-SiC microcube.

(a) The scattering cross section normalized by the physical cross section for a microcube with a side length of L = 1 μm illuminated by a planar electric field with a magnitude of 1 V/m polarized along the x-axis and propagating toward negative z-direction (see the inset). The multipole expansion of the normalized scattering cross section is also shown. (b) The same as Panel a but for L = 2 μm. (c) The same as Panel a but for L = 3 μm. (d) The spatial distribution of the induced electric field within the microcube of Panel a (L = 1 μm) at wavelengths of 2.1 and 3.1 μm. The electric field is plotted in the x-z plane in the middle of the microcube, i.e. in $y = \frac{L}{2}$. The unit for the color bar is V/m. (e) The distribution of the induced charge density within the microcube with L = 1 μm at the wavelengths of 11.2 and 11.5 μm. The microcube is illuminated by the electric field schematically shown in the inset of Panel (a). The unit for the color bar is C/m^2.

The absorption cross section normalized by the physical cross section, σ_a/L^2, for the microcube with L = 2 μm is shown in Fig. 3-2(a). The extinction coefficient for 6H-SiC at 400°C is shown in the inset of Fig. 3-2(a). The EQ-MQ and ED-MD Mie resonances, which are dominant in the scattering cross section, are suppressed in the spectrum of absorption cross section due to the small extinction coefficient of 6H-SiC at wavelengths below 10 μm. Even though the electric field inside the microcube is resonantly large at the wavelengths of EQ-MQ and ED-MD Mie resonances, it is not strongly absorbed by the microcube due to the low extinction coefficient. The

ED-MD shoulders at $\lambda = 6.2$ and 6.6 μm in Fig. 3-1(b) are boosted in the absorption spectrum as the extinction coefficient has two small peaks at these two wavelengths.

Next, the collective thermal radiation from an array of Mie resonators, as characterized by the spectral, directional emissivity, ε'_λ, is modeled for a periodic, square-lattice array of microcubes with a side length of L = 2 μm and two inter-cube spacings of D = 1.5 and 3.0 μm. The emissivity is calculated using the field amplitude reflection and transmission coefficients as $\varepsilon'_\lambda = \frac{1}{2}\sum_{\gamma=\mathrm{TE,TM}}\left(1 - \left|R_\lambda^\gamma\right|^2 - \left|T_\lambda^\gamma\right|^2\right)$, where γ refers to the transverse electric (TE) and transverse magnetic (TM) polarizations, and R_λ^γ and T_λ^γ are the field amplitude reflection and transmission coefficients, respectively. The latter are simulated using the SCUFF-TRANSMISSION module of the SCUFF-EM electromagnetic solver [25]. The spectral, normal (to the plane of the array) emissivity, ε'_λ, for the array is shown in Fig. 3-2(b). The main difference between the spectra of the absorption cross section for a single microcube, Fig. 3-2(a), and the emissivity for an array of microcubes, Fig. 3-2(b), is the abrupt enhancement of the emissivity of the array for $\lambda < 3.5$ μm when D = 1.5 μm and for $\lambda < 5.0$ μm when D = 3.0 μm. The wavelengths of λ = 3.5 and 5.0 μm are the cut-off wavelengths of the first order diffraction for the arrays with D = 1.5 μm and D = 3.0 μm, respectively. The cut-off wavelength of the diffraction order (m,n), also known as the wavelength of Rayleigh anomaly, is given by $\lambda_c^{m,n} = n_d \frac{\Lambda}{\sqrt{m^2+n^2}}$, where Λ and n_d are the array pitch ($\Lambda = L + D$) and refractive index of the medium where the diffraction occurs (here n_d = 1), respectively [26]. When $\lambda > \lambda_c^{m,n}$, the (m,n) diffraction order has a parallel component of the wavevector $k_\rho^{m,n} = \frac{2\pi}{n_d\Lambda/\sqrt{m^2+n^2}}$ for the normal direction which is greater than the magnitude of the wavevector in the free space ($k_0 = \frac{2\pi}{\lambda}$) and thus is evanescent in the free space. When $\lambda < \lambda_c^{m,n}$,

$k_\rho^{m,n} > k_0$ and the (m, n) mode is propagative in the free space. For the arrays with D = 1.5 and 3.0 μm, the first order modes (±1,0) and (0,±1) become propagative as the wavelength reduces to $\lambda_c^{\pm 1,0} = \lambda_c^{0,\pm 1}$ = 3.5 and 5 μm, respectively. These propagative modes, which can travel to the far zone, contribute to the emissivity and abruptly increase this property for $\lambda < \lambda_c^{\pm 1,0}$. When $\lambda > \lambda_c^{\pm 1,0}$, the first order diffraction mode is evanescent in the free space and cannot contribute to the emissivity. As such, the spectrum of the emissivity of the array for $\lambda > \lambda_c^{\pm 1,0}$ is similar to that of σ_a for a single microcube.

Figure 3-2(b) also shows that when the inter-cube spacing reduces from 3 to 1.5 μm, the spectral locations of the emissivity peaks are minimally affected. The reason is that the inter-cube spacings considered in this study are relatively large and thus the interaction between neighboring microcubes is not strong enough to cause any significant shift in the spectral locations of the peaks. The effect of inter-cube spacing on the magnitude of the Mie resonances is stronger than on the spectral locations of the peaks. As the inter-cube spacing decreases, both the volume of the emitters per unit area of the array and the electromagnetic interactions between the microcubes increase. The increase in the volume of emitters enhances thermal radiation from the array, while strong interactions between neighboring microcubes may affect the magnitude of the electric field inside the microcubes negatively, causing a decrease in the emissivity [21]. Depending on the relative strength of these two competing effects, the magnitude of the Mie resonances in the emissivity spectra may increase or decrease. For example, when D decreases from 3 to 1.5 μm, the magnitudes of the emissivity peaks at 12.8 and 13.1 μm, which are due to the ED Mie resonances increase, while the magnitude of the peak at 13.6 μm due to the MD Mie resonance decreases. The reason can be explained by considering the spatial distribution of the electric field within the

microcubes. The electric field distribution is plotted in Fig. 3-2(c) for three wavelengths of 12.8, 13.1, and 13.6 μm and two inter-cube spacings of D = 1.5 and 3 μm when the array is illuminated by the electric field schematically shown in the inset of Fig. 3-2(a). Figure 3-2(c) shows that the magnitude of the electric field within the microcubes at the wavelength of the ED resonances (12.8 μm and 13.1 μm) does not change significantly as the D reduces to 1.5 μm. This is since the electric field for the ED resonance is concentrated at the center of the microcubes, and thus is not significantly affected when the interspacing of the microcubes decreases. While the magnitude of the electric field within the microcubes at the wavelengths of the ED resonances does not significantly change with decreasing D, the volume of the emitters increases with the reduction of D enhancing the emissivity at 12.8 and 13.1 μm. Inversely, the electric field within the microcubes at the MD Mie resonance, as shown in Fig. 3-2(c), is strong at the edges of the microcubes. The streamlines of the electric field in the y-z plane in the middle of the cube (i.e., in the x = L/2 plane) are also shown in Fig. 3-2(d) at the wavelength of the MD Mie resonance (13.6 μm) for the case with D = 3 μm. As it is seen from Fig. 3-2(d), the electric fields of neighboring microcubes have opposite directions. The strong and opposite electric fields of the neighboring microcubes significantly reduces the magnitude of the electric field within the resonators as D decreases. As such, the emissivity of the array at the wavelength of the MD Mie resonance reduces when D decreases, even though the volume of the emitters per unit area of the array is larger at smaller Ds.

The spectral, normal emissivity for an array of 6H-SiC microcubes with L = 2 μm on a 6H-SiC substrate is shown in Fig. 3-2(e) for two inter-cube spacings of D = 1.5 and 3 μm. The emissivity for a flat unpatterned 6H-SiC substrate is also shown in Fig. 3-2(e). It is seen from Fig. 3-2(e) that the emissivity of the on-substrate array is very different from the free-standing array with the same L and D shown in Fig. 3-2(b). When D = 1.5 μm, the on-substrate array has an

emissivity greater than 0.9 over the entire spectral range of 2 to 10.4 μm and 13.6 to 16 μm, which is much greater than the emissivity of the unpatterned substrate at the same temperature. This enhanced emissivity is due to thermal radiation of Mie resonances from the microcubes as well as scattering near-field thermal radiation from the substrate to the far field by the microcube resonators. Regarding the latter, the array of the microcubes also acts as a grating for the substrate and couples a portion of the evanescent electromagnetic waves thermally emitted by the substrate into propagating waves in the free space, thus increasing the emissivity. The array can reduce the parallel component of the wavevector for thermally emitted evanescent waves of the substrate by $(m+n)\frac{2\pi}{\Lambda}$, where m and n are integers. As such, the evanescent waves with a parallel component of the wavevector $k_\rho < k_0 + (m+n)\frac{2\pi}{\Lambda}$ can couple into the far-field enhancing the emissivity. The emissivity of the on-substrate array has also four pronounced peaks, which are located at 10.5, 11.0, 12.8, and 13.8 μm for the array with D = 3 μm. The first two peaks, which are located within the Reststrahlen band of 6H-SiC, are due to thermal emission of ED LSPh resonances from the microbuses, while the peaks at 12.8 and 13.8 μm are due to thermal emission of ED and MD Mie resonances, respectively. It is seen from Fig. 3-2(e) that the magnitude of the MD peak at 13.8 μm is much greater than the ED peak at 12.8 μm, and that the MD peak for the on-substrate array is broadened compared to the free-standing array. The large and broadened MD peak for the on-substrate array is due to the strong coupling between the MD mode and the substrate. The electric field distributions within the microcubes and the substrate are plotted in Fig. 2f for the ED and MD peaks at 12.8 and 13.8 μm, respectively. In Fig. 3-2(f), D = 3 μm and the electric field is plotted in the x-z plane in the middle of the microcubes. Figure 3-2(e) clearly shows the strong coupling between the microcubes and the substrate at the MD Mie resonance, which results in enhanced thermal radiation and broadening of the MD peak.

Figure 3-2(e) shows that the emissivity of the array with the inter-cube spacing of D = 1.5 μm is greater than the one with D = 3 μm in the considered spectral band except for ~ 5.0 – 7.9 μm and ~ 10.5 – 11.5 μm. The emissivity of the array with D = 1.5 μm is greater than that for D = 3 μm due to a larger volume of Mie resonators and a greater contribution from evanescent waves thermally emitted by the substrate. As mentioned before, the evanescent waves emitted from the substrate with a wavevector of $k_\rho < k_0 + (m+n)\frac{2\pi}{\Lambda}$ can couple to the far field by the Mie resonators. As D decreases, Λ decreases and thus more evanescent waves can couple to the far field for a given wavelength. Despite this, the emissivity of the array with D = 1.5 μm is smaller than the one with D = 3.5 μm in the spectral bands of ~ 5.0 – 7.9 μm and ~ 10.5 – 11.5 μm. The reason is the strong inter-cube interactions in these two spectral bands caused by the MD Mie and ED LSPh resonances. As seen from Fig. 3-1(b), the MD Mie resonance is active between 5.0 and 7.9 μm, while the ED LSPh resonance is located between 10.5 – 11.5 μm. Figure 3-1(d) shows that the electric field at the MD Mie and ED LSPh resonances is concentrated at the boundaries of the microcubes and thus is negatively affected as the distance between the neighboring microcubes, D, decreases. This decrease in the electric field results in a reduction in the emissivity of the array.

Figure 3-2(e) shows that the emissivity of the unpatterned substrate is low in the Reststrahlen band. The reason is that 6H-SiC is highly reflective, and thus poorly emissive and absorptive, in the Reststrahlen band due to a negative real part of the dielectric function. While the far-field thermal radiation from the unpatterned substrate is low in the Reststrahlen band, the near-field thermal radiation from the substrate is resonantly large in the Reststrahlen band due to thermal emission SPhP modes. The presence of the Mie resonator array increases the emissivity of the

unpatterned substrate in the Reststrahlen band. This enhancement is due to thermal emission of ED LSPh resonances from the microcubes causing two peaks around 10.6 and 11.0 μm as well as scattering of near-field thermal radiation of the substrate to the far field by Mie resonators. It should be noted that the pitch sizes of the two arrays considered in this study are not sufficiently large to couple the near-field SPhPs, which have very large wavevectors, into the far field.

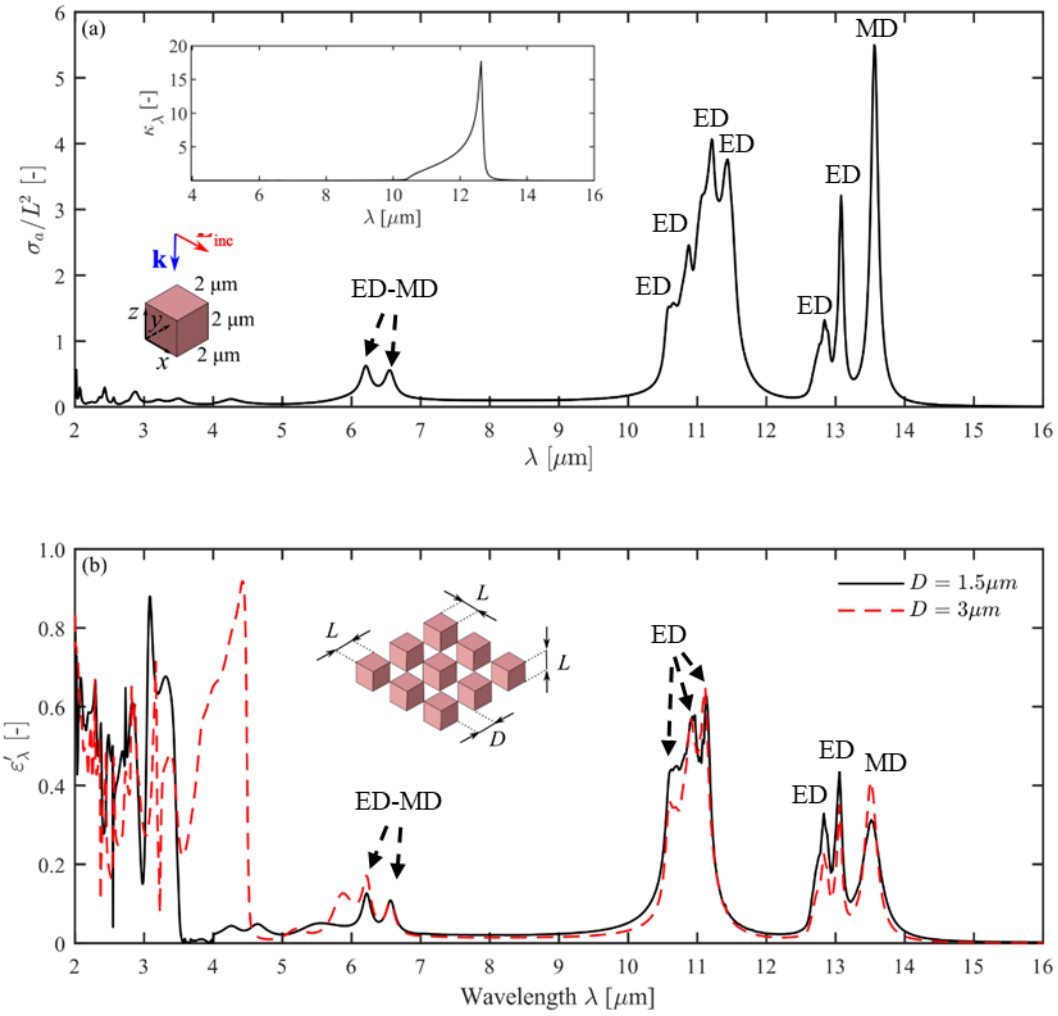

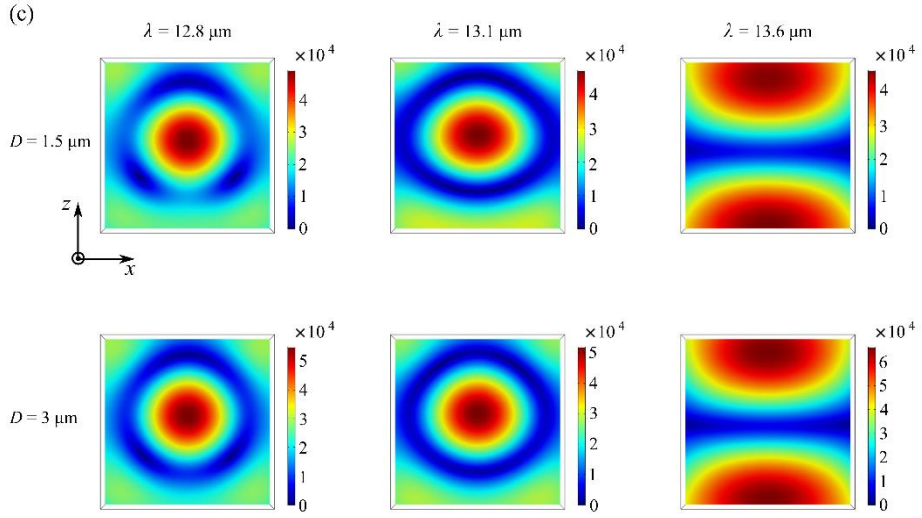
(c)
λ = 12.8 μm
λ = 13.1 μm
λ = 13.6 μm
D = 1.5 μm
D = 3 μm
×10^4
z
x

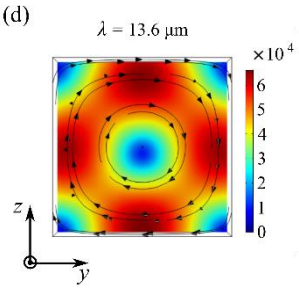
(d)
λ = 13.6 μm
×10^4
z
y

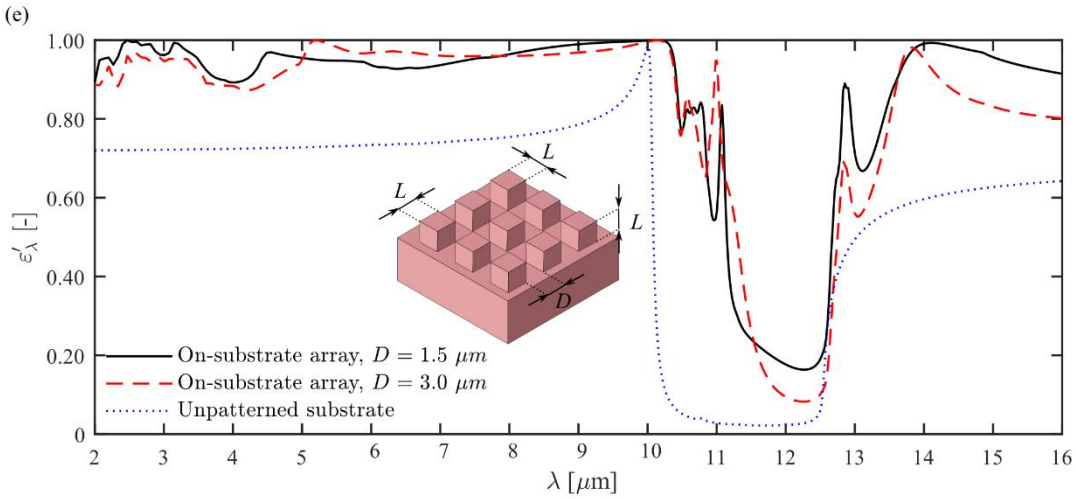
(e)
ε'λ [-]
λ [μm]
L
D
On-substrate array, D = 1.5 μm
On-substrate array, D = 3.0 μm
Unpatterned substrate

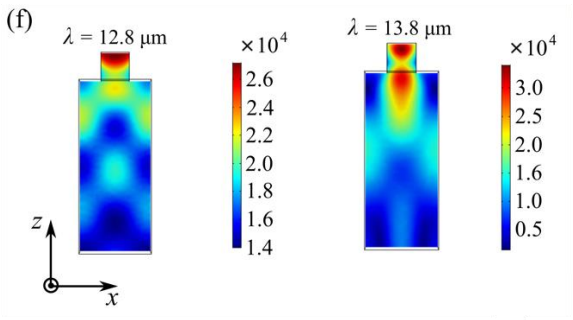

Figure 3-2 Absorption cross-section of single 6H-SiC microcube, emissivity of free-standing and on-substrate array of 6H-SiC microcubes.

(a) The absorption cross section normalized by the physical cross section, σ_a/L^2, for a microcube with L = 2 μm. The extinction coefficient of 6H-SiC at 400°C and the incident electric field are shown in the inset. (b) The spectral, normal emissivity of a free-standing periodic array of microcubes with a side length of L = 2 μm and two inter-cube spacings of D = 1.5 and 3 μm at a temperature of 400°C. (c) The spatial distribution of the induced electric field within the Mie resonators for a free-standing array of microcubes with L = 2 μm and D = 1.5 μm. The electric field distribution is plotted in the in the $x = \frac{L}{2}$ plane and the array is illuminated by the same incident electric field as in Fig. 2a. (d) The distribution of the electric field in the $x = \frac{L}{2}$ plane at a wavelength of λ = 13.6 μm for the Mie resonator array of Panel b. (e) The same as Panel b but for an on-substrate array. (f) The distribution of the electric field within the microcubes and substrate at the ED and MD Mie resonances when the array is illuminated by the electric field shown in Panel a. In this figure, D = 1.5 μm and the electric field is plotted in the $y = \frac{L}{2}$ plane.

Overall, the presence of the Mie resonator array increases the total (spectrally integrated over 2 – 16 μm, where 92% of thermal radiation from a blackbody at 400°C is located), normal emissivity of the substrate from 0.67 to 0.91 and 0.89 when D = 1.5 and 3.0 μm, respectively. This enhancement demonstrates that the Mie resonators are very promising for increasing far-field thermal radiation from dielectric media which is crucial for thermal management and energy applications.

Next, we experimentally demonstrate the potential of Mie resonators for enhancing the emissivity of the dielectric media in a broad spectral range. The array with L = 2 μm and D = 1.5 μm is selected for the experiments due to a larger emissivity than the array with D = 3.5 μm. The array is fabricated on a 6H-SiC substrate using electron beam lithography and reactive ion etching (see Appendix D for details of the fabrication method). A scanning electron microscopy (SEM) image of the fabricated sample is shown in Fig. 3-3(a). The fabricated Mie resonators have a

microcuboid geometry with side lengths of 2.1 × 2.1 × 2.3 μm and are separated by an inter-cube spacing of D = 1.47 μm. An in-house experimental set-up is used for direct measurement of the spectral, directional emissivity (see Appendix E for details of the emissivity measurement setup) for an unpatterned 6H-SiC substrate at a normal direction as well as the on-substrate array for several directions ranging from 0 to 60° with respect to the surface normal. The emissivity is measured in a spectral range of 5 – 16 μm where the MCT detector used for the experiments can detect a strong thermal radiation signal for the samples. It should be mentioned that in this study, we measure the emissivity in a direct manner by collecting thermal radiation from the samples. As such, the measured signals are much weaker than those detected when measuring emissivity indirectly by illuminating the sample by an external IR source. The measured emissivity is shown in Fig 4-3(b). The emissivity for the fabricated geometry is also modeled for the same directions and presented in Fig. 3-3(c). Several points can be observed from Figs. 4-3(b) and 4-3(c). First, the emissivity measured for the Mie resonator array is greater than that for the unpatterned substrate. The total, normal emissivity in the spectral range of 5 – 16 μm increases from 0.73 for the unpatterned substrate to 0.91 for the on-substrate array. Second, comparing Fig. 3-3(b) with Fig. 3-3(c), it seen that the experimentally measured emissivity for the array is in great agreement with the one predicted theoretically. The near-unity emissivity in the spectral range of 5 to 10 μm is captured in the measurements, while the transverse ED LSPh resonances around 10.7 and 11.1 μm and the ED and MD Mie resonances around 12.8 and 14.0 μm, respectively, are also measured in the emissivity spectra. The measured emissivity in Fig. 3-3(b) demonstrates direct thermal radiation of Mie resonances from microcuboids of 6H-SiC. It is also seen from Figs. 4-3(b) and 3(c) that the measured emissivity for the Mie resonator array slightly changes with the angle but

remains relatively large at all angles. The enhanced emissivity for broad spectral and angular ranges is crucial for enhanced radiative heat transfer from the material.

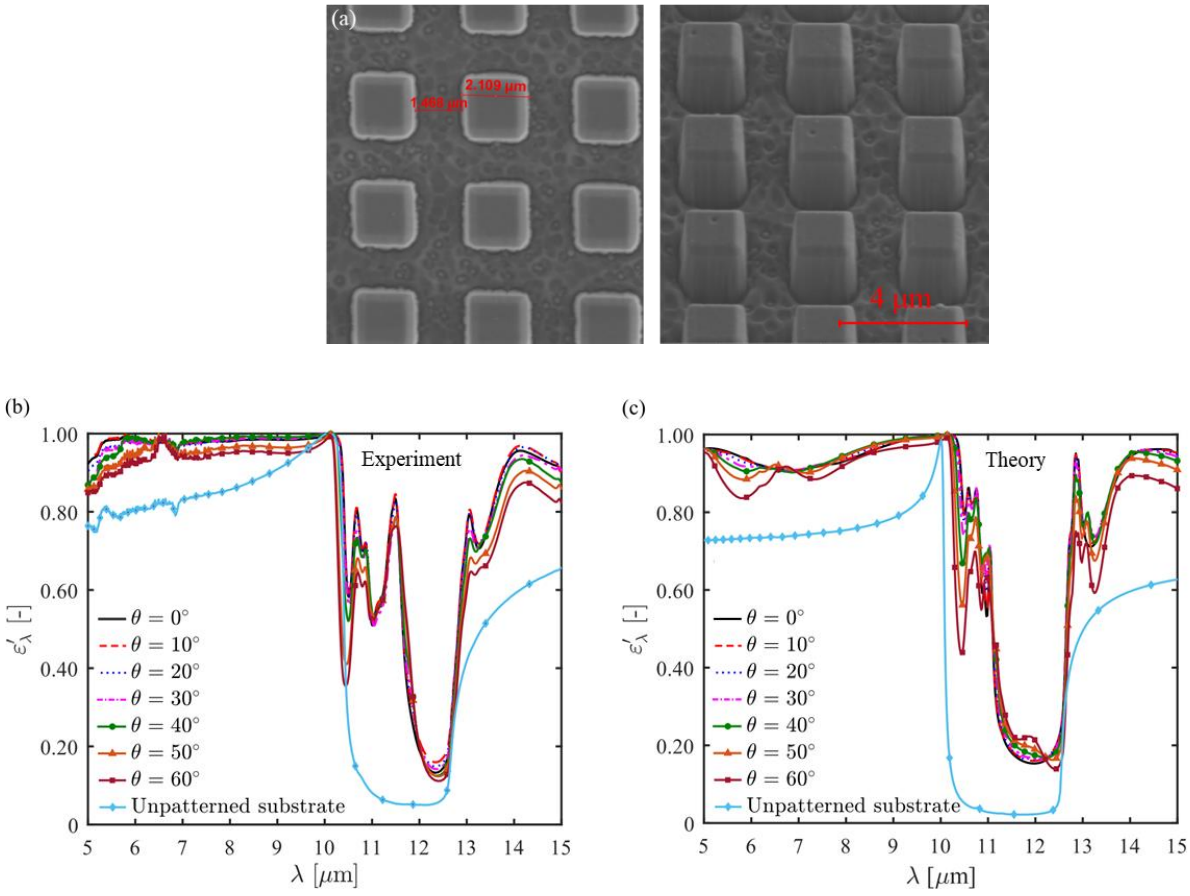

Figure 3-3 Fabricated sample and experimental measurement of the emissivity.
(a) A micrographs of the fabricated Mie resonator array. The micrograph on the left is taken from above, while the one on the right is taken at an angle of 45°. The fabricated Mie resonators have a cuboid shape with side lengths of 2.1, 2.1, and 2.3 µm and an interspacing of $D = 1.47$ µm. (b) The measured spectral, directional emissivity for the fabricated array in Panel a. (c) The predicted spectral, directional emissivity for the fabricated array in Panel a at various angles ranging from 0 to 60° with respect to the surface normal. The emissivity at the normal angle is also shown for an unpatterned substrate for comparison.

3.4 Conclusions

Thermal radiation of Mie resonances from microcuboids of a large refractive index material, namely 6H-SiC, was demonstrated theoretically and experimentally. It was shown that Mie resonator arrays can be designed to have enhanced emissivity in wide spectral and angular ranges. A periodic array of 6H-SiC microcuboids was designed and fabricated on a 6H-SiC substate. The

emissivity of the Mie resonator array was measured using an in-house emissometer. The array demonstrated an enhanced emissivity in the wide spectral range of 2 – 16 μm and angular range of 0 to 60°. The enhanced emissivity for the array is due to thermal emission of Mie resonances by the microcuboids as well as the scattering of near-field thermal radiation from the substrate into the far field by the Mie resonators. Thermal radiation of Mie resonances due to the electric and magnetic dipoles as well as localized surface phonon resonances due to the transverse electric dipole, which appear as pronounced peaks in the emissivity spectra, were experimentally demonstrated. Our study provides a guide for designing broadband and omni-directional thermal emitters made from arrays of Mie resonators which are beneficial for thermal management and energy applications.

3.5 References

[1] Le Gall, J.; Olivier, M.; Greffet, J.-J. Experimental and Theoretical Study of Reflection and Coherent Thermal Emission by a SiC Grating Supporting a Surface-Phonon Polariton. *Physical Review B* **1997**, *55* (15), 10105.

[2] Greffet, J.-J.; Carminati, R.; Joulain, K.; Mulet, J.-P.; Mainguy, S.; Chen, Y. Coherent Emission of Light by Thermal Sources. *Nature* **2002**, *416* (6876), 61–64.

[3] Dahan, N.; Niv, A.; Biener, G.; Gorodetski, Y.; Kleiner, V.; Hasman, E. Enhanced Coherency of Thermal Emission: Beyond the Limitation Imposed by Delocalized Surface Waves. *Physical Review B* **2007**, *76* (4), 045427.

[4] Arnold, C.; Marquier, F.; Garin, M.; Pardo, F.; Collin, S.; Bardou, N.; Pelouard, J.-L.; Greffet, J.-J. Coherent Thermal Infrared Emission by Two-Dimensional Silicon Carbide Gratings. *Physical Review B* **2012**, *86* (3), 035316.

[5] Hasman, E.; Kleiner, V.; Dahan, N.; Gorodetski, Y.; Frischwasser, K.; Balin, I. Manipulation of Thermal Emission by Use of Micro and Nanoscale Structures. *Journal Heat Transfer* **2012**, *134* (3).

[6] Hervé, A.; Drévillon, J.; Ezzahri, Y.; Joulain, K.; Meneses, D. D. S.; Hugonin, J.-P. Temperature Dependence of a Microstructured SiC Coherent Thermal Source. *Journal of Quantitative Spectroscopy and Radiative Transfer* **2016**, *180*, 29–38.

[7] Chalabi, H.; Alù, A.; Brongersma, M. L. Focused Thermal Emission from a Nanostructured SiC Surface. *Physical Review B* **2016**, *94* (9), 094307.

[8] Starko-Bowes, R.; Dai, J.; Newman, W.; Molesky, S.; Qi, L.; Satija, A.; Tsui, Y.; Gupta, M.; Fedosejevs, R.; Pramanik, S. Dual-Band Quasi-Coherent Radiative Thermal Source. *Journal of Quantitative Spectroscopy and Radiative Transfer* **2018**, *216*, 99–104.

[9] Schuller, J.A., Taubner, T. and Brongersma, M.L., 2009. Optical antenna thermal emitters. Nature Photonics, 3(11), pp.658-661.

[10] Caldwell, J.D., Glembocki, O.J., Francescato, Y., Sharac, N., Giannini, V., Bezares, F.J., Long, J.P., Owrutsky, J.C., Vurgaftman, I., Tischler, J.G. and Wheeler, V.D., 2013. Low-loss, extreme subdiffraction photon confinement via silicon carbide localized surface phonon polariton resonators. Nano letters, 13(8), pp.3690-3697.

[11] Neuner, B., Wu, C., Eyck, G.T., Sinclair, M., Brener, I. and Shvets, G., 2013. Efficient infrared thermal emitters based on low-albedo polaritonic meta-surfaces. Applied Physics Letters, 102(21).

[12] Chen, Y., Francescato, Y., Caldwell, J.D., Giannini, V., Maß, T.W., Glembocki, O.J., Bezares, F.J., Taubner, T., Kasica, R., Hong, M. and Maier, S.A., 2014. Spectral tuning of localized surface phonon polariton resonators for low-loss mid-IR applications. Acs Photonics, 1(8), pp.718-724.

[13] Razdolski, I., Chen, Y., Giles, A.J., Gewinner, S., Schöllkopf, W., Hong, M., Wolf, M., Giannini, V., Caldwell, J.D., Maier, S.A. and Paarmann, A., 2016. Resonant enhancement of second-harmonic generation in the mid-infrared using localized surface phonon polaritons in subdiffractional nanostructures. Nano letters, 16(11), pp.6954-6959.

[14] Gubbin, C.R., Martini, F., Politi, A., Maier, S.A. and De Liberato, S., 2016. Strong and coherent coupling between localized and propagating phonon polaritons. Physical review letters, 116(24), p.246402.

[15] Gubbin, C.R., Maier, S.A. and De Liberato, S., 2017. Theoretical investigation of phonon polaritons in SiC micropillar resonators. Physical review B, 95(3), p.035313.

[16] Wang, T., Li, P., Chigrin, D.N., Giles, A.J., Bezares, F.J., Glembocki, O.J., Caldwell, J.D. and Taubner, T., 2017. Phonon-polaritonic bowtie nanoantennas: controlling infrared thermal radiation at the nanoscale. Acs Photonics, 4(7), pp.1753-1760.

[17] Gubbin, C.R., Berte, R., Meeker, M.A., Giles, A.J., Ellis, C.T., Tischler, J.G., Wheeler, V.D., Maier, S.A., Caldwell, J.D. and De Liberato, S., 2019. Hybrid longitudinal-transverse phonon polaritons. Nature communications, 10(1), p.1682.

[18] Lu, G., Nolen, J.R., Folland, T.G., Tadjer, M.J., Walker, D.G. and Caldwell, J.D., 2020. Narrowband polaritonic thermal emitters driven by waste heat. ACS omega, 5(19), pp.10900-10908.

[19] Lu, G., Gubbin, C.R., Nolen, J.R., Folland, T.G., Diaz-Granados, K., Kravchenko, I.I., Spencer, J.A., Tadjer, M.J., Glembocki, O.J., De Liberato, S. and Caldwell, J.D., 2021. Collective phonon–polaritonic modes in silicon carbide subarrays. ACS nano, 16(1), pp.963-973.

[20] Lu, G., Gubbin, C.R., Nolen, J.R., Folland, T., Tadjer, M.J., De Liberato, S. and Caldwell, J.D., 2021. Engineering the spectral and spatial dispersion of thermal emission via polariton–phonon strong coupling. Nano letters, 21(4), pp.1831-1838.

[21] Pouria, R., Chow, P.K., Tiwald, T., Zare, S. and Edalatpour, S., 2022. Far-field thermal radiation from short-pitch silicon-carbide nanopillar arrays. Applied Physics Letters, 121(13).

[22] Ghanekar, A., Lin, L. and Zheng, Y., 2016. Novel and efficient Mie-metamaterial thermal emitter for thermophotovoltaic systems. Optics express, 24(10), pp.A868-A877.

[23] Howes, A., Nolen, J.R., Caldwell, J.D. and Valentine, J., 2020. Near-unity and narrowband thermal emissivity in balanced dielectric metasurfaces. Advanced Optical Materials, 8(4), p.1901470.

[24] Alaee, R., Rockstuhl, C. and Fernandez-Corbaton, I., 2018. An electromagnetic multipole expansion beyond the long-wavelength approximation. Optics Communications, 407, pp.17-21.

[25] Reid, M. T. H.; Johnson, S. G. Solving electromagnetic scattering problems with scuff-scatter http://homerreid.github.io/scuff-em-documentation/applications/scuff-scatter/scuff-scatter/.

[26] Hamdad, S., Diallo, A.T., Chakaroun, M. and Boudrioua, A., 2022. The role of Rayleigh anomalies in the coupling process of plasmonic gratings and the control of the emission properties of organic molecules. Scientific Reports, 12(1), p.3218.

Chapter 4

Tuning The Spectrum of Near-Field Radiative Heat Transfer Using Mie Resonance-Based Metamaterials

This chapter has been reproduced from a previous publication in Physical Review B: Pouria, R. and Edalatpour, S., 2024. Tuning the spectrum of near-field radiative heat transfer using Mie resonance-based metamaterials. *Physical Review B*, *109*(4), p.045407.

4.1 Abstract

Tuning the spectrum of near-field radiative heat transfer is crucial for many potential applications such as near-field thermophotovoltaic and thermophotonic power generation. Mie resonance-based metamaterials are promising candidates for tuning the near-field spectra. In this manuscript, we utilize the Fourier modal method to perform non-approximate simulations of near-field radiative heat flux between Mie resonance-based metamaterials. By decomposing the electromagnetic response of the Mie resonators into contributions from various multipoles, we identify the origins of the peaks in the near-field spectra. We study the effect of the refractive index, extinction coefficient, shape, and interspacing of Mie resonators, as well as the separation distance of the metamaterials on the spectrum of neat-field heat flux. Our study shows that as the refractive index of the metamaterial increases, the heat flux increases and the spectral locations of the Mie resonances redshift. As the extinction coefficient increases, the near-field heat flux increases and the damping of the Mie resonances eventually results in a broadband spectrum for the heat flux. Resonance splitting is observed when the distance between the Mie resonators approaches the nanometer scale. While the existing studies suggest that Mie resonance-based metamaterials increase the near-field heat flux, the near-field heat transfer between these metamaterials is smaller than that between two thin films of the same material and thickness.

However, Mie resonance-based metamaterials are promising for tuning the spectrum of the near-field heat flux.

4.2 Introduction

Radiative heat transfer (RHT) exceeds the blackbody limit by orders of magnitude when the heat-exchanging media are separated by a gap smaller than the thermal wavelength [1]. The enhancement of RHT at sub-wavelength separation gaps, referred to as the near-field RHT (NFRHT), is due to the tunneling of exponentially decaying evanescent waves that are only substantial at sub-wavelength distances from the emitting surface [1,2]. Near-field radiative heat transfer has several promising applications such as nano-gap thermophotovoltaic [3] and thermophotonic [4] power generation, thermal rectification [5,6], and near-field photonic cooling [7]. Tuning the spectrum of NFRHT is imperative for the development of these applications.

Metamaterials, which are materials engineered at the sub-wavelength scale [8], have been proposed for tuning the spectrum of NFRHT [9-15]. One class of the proposed metamaterials is the Mie resonance-based metamaterials which are made of sub-wavelength particles of dielectric materials [16]. These sub-wavelength particles can thermally emit at Mie resonances causing sharp peaks in the spectrum of NFRHT. The Mie resonance-based metamaterials are promising for NFRHT applications. They provide a mechanism for tuning the spectrum of NFRHT for the dielectric media that do not support surface phonon polaritons. Additionally, the spectrum of NFRHT for Mie resonance-based metamaterials can be tuned to a great extent by changing the size, shape, and material properties of the resonators. Despite this potential, so far very few studies have focused on NFRHT in Mie resonance-based metamaterials [16-20]. Using the effective medium theory (EMT), it was shown that the Mie resonance-based metamaterials can have

negative effective permeability, in addition to negative effective permittivity, and thus they can emit the surface modes in both transverse electric (TE) and transverse magnetic (TM) polarizations [16-19]. The TE-polarized surface modes, which cannot be emitted from natural materials, introduce new peaks in the spectra of near-field heat flux and provide an additional channel for heat transfer [16-19]. The EMT, which treats the array of the sub-wavelength resonators as a semi-infinite planar medium with an effective permittivity and permeability, is known to be invalid for predicting both the spectrum and the magnitude of NFRHT [21]. Recently, NFRHT between two Mie resonance-based metamaterials made of two-dimensional periodic arrays of tellurium cubes was studied using numerical simulations. It was shown that the Mie resonances cause peaks in the near-field spectra, and the locations of the peaks can be modulated by changing the size of the Mie resonators [20]. However, there is a knowledge gap about the origin of the peaks observed in the spectrum of NFRHT and how these peaks evolve as the material properties and the geometry of the array vary.

In this paper, we employ a non-approximate numerical method, namely the Fourier modal method (also known as the rigorous-coupled wave analysis) [22], to study the NFRHT between periodic arrays of Mie resonators for different material properties, separation gaps, and geometries. Using a multipole expansion of the scattering cross section of the individual Mie resonators [23], we identify the origin of various peaks observed in the spectrum of NFRHT. While previous studies indicate that the Mie resonance-based metamaterials result in enhanced NFRHT [16-20], we show that indeed NFRHT between these metamaterials is always less than that for a thin film of the same material and thickness as the corresponding metamaterials. This study elucidates the physics underlying NFRHT between Mie resonance-based metamaterials and can guide designing thermal emitters with desired NFRHT spectrum.

This paper is organized as follows. The problem under study and the methods used for solving this problem are described in Sec. 4.3. The results are described in Sec. 4.4, and the concluding remarks are presented in Sec. 4.5.

4.3 Description of the Problem and Methods

The problem under consideration is illustrated in Fig. 4-1. Two identical Mie resonance-based metamaterials made of two-dimensional periodic arrays of micro-cuboids are separated by a vacuum gap of size d. The cuboids have a side length L, a width W, a height H, and an interspacing D. The temperatures of the two metamaterials are fixed at T_1 = 400 K and T_2 = 300 K. The objective is to analyze the spectrum of NFRHT between the two metamaterials and study how the spectrum evolves as the material properties, the separation gap, and the geometry of the array change.

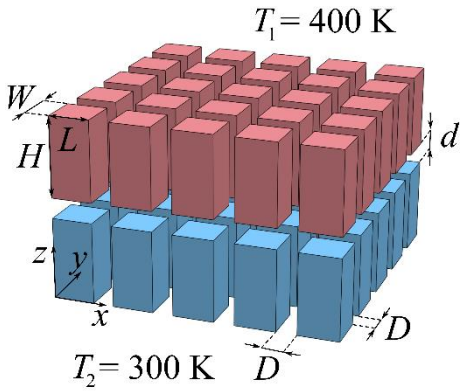

Figure 4-1 A schematic of the system under study.
Two Mie resonance-based metamaterials made of two-dimensional periodic arrays of micro-cuboids are separated by a gap of size *d*. One of the metamaterials is at temperature T_1 = 400 K, while the other one is kept at temperature T_2 = 300 K. Near-field radiative heat transfer between the two metamaterials is desired.

The near-field radiative heat flux between the metamaterials is found using the fluctuational electrodynamic theorem [1,2], and by applying the Fourier modal method, as implemented in the MESH software [22], for solving the stochastic Maxwell's equations. A summary of the Fourier modal method used for numerical modeling of NFRHT is provided in Appendix B. To identify the

peaks observed in the spectrum of the near-field heat flux, the scattering cross section of the micro-cuboids is decomposed into contributions from electric and magnetic dipoles and quadrupoles. The spectral locations of the Mie resonances in the scattering cross section are very close to those in the absorption cross section. As such, and due to the availability of the multipole expansion for the scattering cross section [23], we choose to decompose the scattering cross section into multipole contributions in this study. When an individual cuboid is illuminated with an incident electric field, $\mathbf{E}_{\mathrm{inc}}(\mathbf{r},\omega)$, a current is induced inside the cuboids. The induced current density is given by $\mathbf{J}_\omega(\mathbf{r},\omega) = -\mathrm{i}\omega\varepsilon_0(\varepsilon_r - 1)\mathbf{E}(\mathbf{r},\omega)$, where $\mathbf{r}$, ω, $\mathbf{E}(\mathbf{r},\omega)$, ε_0, and ε_r are the position vector, angular frequency, electric field, permittivity of the free space, and dielectric function of the micro-cuboids, respectively. The moments of the electric and magnetic dipoles and quadrupoles are then found using the induced current density as [23]:

$$p_\alpha = -\frac{1}{\mathrm{i}\omega}\int J_{\omega,\alpha}\, j_0(kr) d^3\mathbf{r} - \frac{k^2}{2\mathrm{i}\omega}\int \frac{j_2(kr)}{(kr)^2}[3(\mathbf{r}.\mathbf{J}_\omega)r_\alpha - r^2 J_{\omega,\alpha}]d^3\mathbf{r} \tag{3.1a}$$

$$m_\alpha = \frac{3}{2}\int (\mathbf{r}\times\mathbf{J}_\omega)_\alpha \frac{j_1(kr)}{kr} d^3\mathbf{r} \tag{3.1b}$$

$$Q^e_{\alpha\beta} = -\frac{3}{\mathrm{i}\omega}\Big\{\int \frac{j_1(kr)}{kr}[3\big(r_\beta J_{\omega,\alpha} + r_\alpha J_{\omega,\beta}\big) - 2(\mathbf{r}.\mathbf{J}_\omega)\delta_{\alpha\beta}]d^3\mathbf{r} + 2k^2\int \frac{j_3(kr)}{(kr)^3}[5r_\alpha r_\beta(\mathbf{r}.\mathbf{J}_\omega) -$$

$$\big(r_\alpha J_{\omega,\beta} + r_\beta J_{\omega,\alpha}\big)r^2 - r^2(\mathbf{r}.\mathbf{J}_\omega)\,\delta_{\alpha\beta}]d^3\mathbf{r}\Big\} \tag{3.1c}$$

$$Q^m_{\alpha\beta} = 15\int \frac{j_2(kr)}{(kr)^2}\{r_\alpha(\mathbf{r}\times\mathbf{J}_\omega)_\beta + r_\beta(\mathbf{r}\times\mathbf{J}_\omega)_\alpha\}d^3\mathbf{r} \tag{3.1d}$$

where p_α and m_α are the α ($\alpha = x, y, z$) component of the electric and magnetic dipole moments, respectively, $Q^e_{\alpha\beta}$ and $Q^m_{\alpha\beta}$ are the $\alpha\beta$ ($\beta = x, y, z$) element of the electric and magnetic quadrupole moment tensors, respectively, r is the magnitude of the position vector, i is the imaginary unit, k is the magnitude of the wavevector in the free space, and $j_n(kr)$ is the spherical

Bessel function of n^{th} kind. The induced current density, $\mathbf{J}_\omega$, required for finding the multipole moments using Eqs. 3.1a-3.1d, is simulated using the COMSOL Wave Optics Module. Once the electric and magnetic multipole moments are found, the contributions from each multipole to the total scattering cross section can be expressed as [23]:

$$\sigma_s^p = \frac{k^4}{6\pi\varepsilon_0^2|\mathbf{E_{inc}}|^2}\sum_\alpha |p_\alpha|^2 \tag{3.2a}$$

$$\sigma_s^m = \frac{k^4}{6\pi\varepsilon_0^2|\mathbf{E_{inc}}|^2}\sum_\alpha \left|\frac{m_\alpha}{c}\right|^2 \tag{3.2b}$$

$$\sigma_s^{Qe} = \frac{k^6}{720\pi\varepsilon_0^2|\mathbf{E_{inc}}|^2}\sum_{\alpha\beta} \left|Q_{\alpha\beta}^e\right|^2 \tag{3.2c}$$

$$\sigma_s^{Qm} = \frac{k^6}{720\pi\varepsilon_0^2 c^2|\mathbf{E_{inc}}|^2}\sum_{\alpha\beta} \left|Q_{\alpha\beta}^m\right|^2 \tag{3.2d}$$

where c is the speed of light in the free space, and σ_s^p, σ_s^m, σ_s^{Qe}, and σ_s^{Qm} are the contributions of the electric dipole, magnetic dipole, electric quadrupole, and magnetic quadrupole to the scattering cross section of the Mie resonators, respectively. It should be noted that the contribution of the higher order modes to the scattering cross section is negligible. This is confirmed by finding the total scattering cross section using the COMSOL Wave Optics Module and comparing the result with the summation of σ_s^p, σ_s^m, σ_s^{Qe}, and σ_s^{Qm} found using Eqs. 3.2a to 3.2d. Equations 3.2a-3.2d are utilized to find the spectral locations of Mie resonances associated with each electric and magnetic multipole.

In addition to the scattering cross section of the Mie resonators, the distribution of the electric field within the resonators when the metamaterial is illuminated by an incident electric field is computed and used for identifying the Mie resonances in the near-field spectra. The electric field distribution is modeled using the COMSOL Wave Optics Module. The spectral NFRHT between

non-periodic arrays of Mie resonators is also found using the SCUFF-NEQ package of the SCUFF-EM electromagnetic solver [24] and is employed for interpreting the spectrum of near-field heat flux.

4.4 Results and Discussion

Figure 4-2(a) shows the spectrum of NFRHT between two identical Mie resonance-based metamaterials made of micro-cubes with side lengths $L = W = H = 2$ μm, and a cubes' interspacing of $D = 2$ μm. Cubical resonators have been selected for this study since cubical microparticles can be fabricated using the standard optical lithography process. The complex refractive index and the separation gap of the two metamaterials are assumed as $\tilde{n} = 2.4 + 0.05i$ and $d = 1$ μm, respectively. The considered refractive index is close to the one for zinc selenide [24]. It should be noted that the considered refractive index may not follow the dispersion rule and the Kramers-Kronig relations. However, we proceed with this refractive index as the main objective of this study is to understand the effects of metamaterial parameters, such as the refractive index and extinction coefficient, on the spectrum of near-field heat flux. Ten peaks are observed in the near-field spectrum which are located at 3.4 μm, 3.7 μm, 4.2 μm, 4.7 μm, 5.4 μm, 6.3 μm, 6.6 μm, 6.9 μm, 7.8 μm, and 9.6 μm. To identify the origins of these peaks, the scattering cross section of an individual micro-cube when illuminated by an external electric field is computed and decomposed into contribution from the electric dipole (ED), magnetic dipole (MD), electric quadrupole (EQ), and magnetic quadrupole (MQ). The incident electric field is directed toward the x-axis, and two incidence angles of 0° and 45° with respect to the z-axis (i.e., normal and oblique incidence, respectively) are considered. Figures 4-2(b) and 4-2(c) show the decomposed scattering cross section of the micro-cubes normalized by the geometrical cross section ($L \cdot W$) for angles of incidence of 0° and 45°, respectively.

Figure 4-2(b) shows that the scattering cross section of the cubes for the normal incidence has three peaks which are located at 3.2 μm, 4.1 μm, and 6.0 μm. Considering the contributions from the ED, EQ, MD, and MQ to the scattering cross section as presented in Fig. 4-2(b), it is found that the peak at 3.2 μm is due to the EQ and MD modes (dominated by the contribution from the EQ), the peak at 4.1 μm is due to the EQ and MQ modes (with dominant contribution from the EQ), and the peak at 6.0 μm is due to contributions from the MD and ED modes (with dominant contribution from the MD). The spectral locations of the peaks in the spectrum of scattering cross section for the oblique incidence shown in Fig. 4-2(c) are approximately the same as those for the normal incidence except for the peak associated with the EQ-MQ modes, which is slightly shifted from 4.1 μm to 4.5 μm. The micro-cubes in an array are close to each other, and thus the Mie modes of the neighboring micro-cubes can spatially overlap. This overlap causes resonant shift and/or splitting of the Mie resonances into a few peaks. For example, the radiative heat flux between two two-dimensional arrays made of sixteen micro-cubes is simulated for separation gaps, d, and interspacing, D, of 10 μm and 2 μm using the SCUFF-NEQ package of the SCUFF-EM electromagnetic solver [25]. The results are shown in Fig. 4-2(d). The spectral locations of the peaks in the heat-flux spectrum for the case with $D = d = 10$ μm is very similar to those of the scattering cross section of the individual micro-cubes. From left to right, the peaks in the heat-flux spectrum are due to the EQ-MD, EQ-MQ (observed for σ_s at normal incidence), EQ-MQ (observed for σ_s at oblique incidence), and MD-ED mode. When the interspacing reduces to $D =$ 2 μm, the MD-ED mode splits into two peaks. With reducing the vacuum gap to $d = 2$ μm, the EQ-MD resonance also splits.

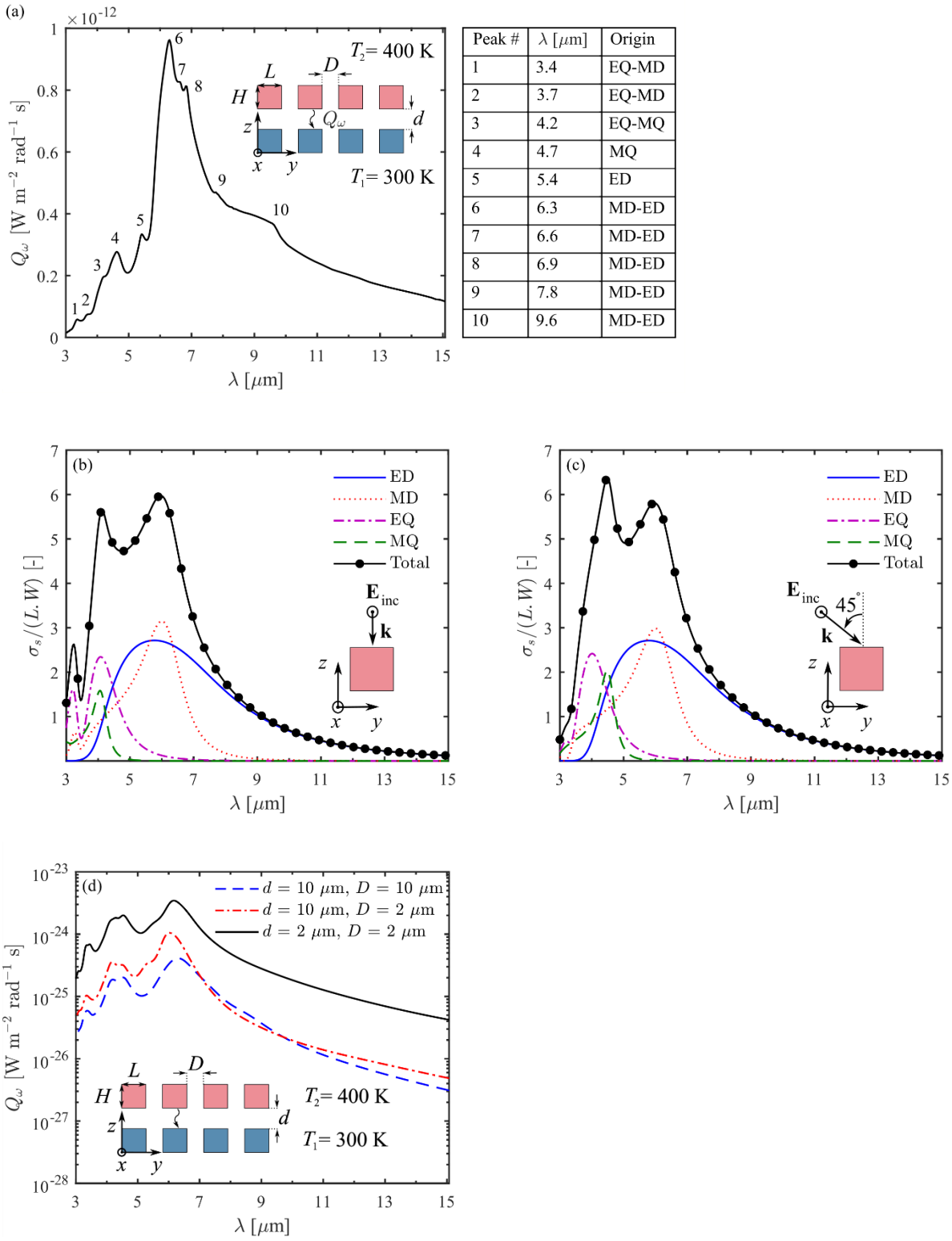

Peak #	λ [μm]	Origin
1	3.4	EQ-MD
2	3.7	EQ-MD
3	4.2	EQ-MQ
4	4.7	MQ
5	5.4	ED
6	6.3	MD-ED
7	6.6	MD-ED
8	6.9	MD-ED
9	7.8	MD-ED
10	9.6	MD-ED

Figure 4-2 Characterizing the spectrum of NFRHT between metamaterials with a complex refractive index of $\tilde{n}$ = 2.4 + 0.05i.

(a) Near-field radiative heat flux between the two metamaterials shown in Fig. 1. The refractive index of the micro-cubes and the separation gap of the metamaterials are $\tilde{n}$ = 2.4 + 0.05i and d = 1 μm, respectively, while $L = H = W$

= D = 2 μm. (b,c) The scattering cross section of an individual micro-cube normalized by the geometrical cross section, when the micro-cube is illuminated by an incident plane wave. The incident electric field is polarized along the x-axis, while it propagates along the z-axis in Panel (b) and at angle of 45° with respect to the z-axis in Panel (c). See the insets of Panels (b) and (c) for schematics. (d) The near-field heat flux between two two-dimensional finite arrays each made of 16 micro-cubes. $L = H = W$ = 2 μm.

Considering the splitting and shift of the peaks caused by the spatial overlap of the Mie modes of the neighboring micro-cubes and using the decomposed scattering cross sections in Figs. 3-2(b) and 3-2(c), the peaks of NFRHT between the two metamaterials can be identified as follows. The peak at 3.4 μm and 3.7 μm are both due to the EQ and MD (with dominant contribution from EQ), the peak at 4.2 μm is due to the EQ and MQ (with dominant contribution from MQ), the peak at 4.7 μm is due to the MQ supported at oblique incidence angles (see Fig. 4-2c), the peak at 5.4 μm is due to the ED, and the last five peaks at 6.3 μm, 6.6 μm, 6.9 μm, 7.8 μm, and 9.6 μm are all due to the ED and MD modes (with dominant contribution from the MD). The electric field distributions within the cubes when the metamaterial is illuminated by an external electric field are also computed at the peaks' wavelengths. The electric fields are plotted in the y-z plane in the middle of the cubes (i.e., in the $x = \frac{L}{2}$ plane), when the metamaterial is excited by an electric field polarized in the x-direction and incident at the normal direction [see Fig. 4-3(a)]. The magnitude of the incident electric field is assumed to be 1 V/m. The electric field distributions at the peaks' wavelengths are provided in Fig. 4-3(b), and they are in agreement with the multipole decomposition analysis. It should be noted that as seen in Fig. 4-2(a), the NFRHT between the two Mie resonance-based metamaterials is dominated by resonant thermal emission and absorption of the MD mode of the micro-cubes.

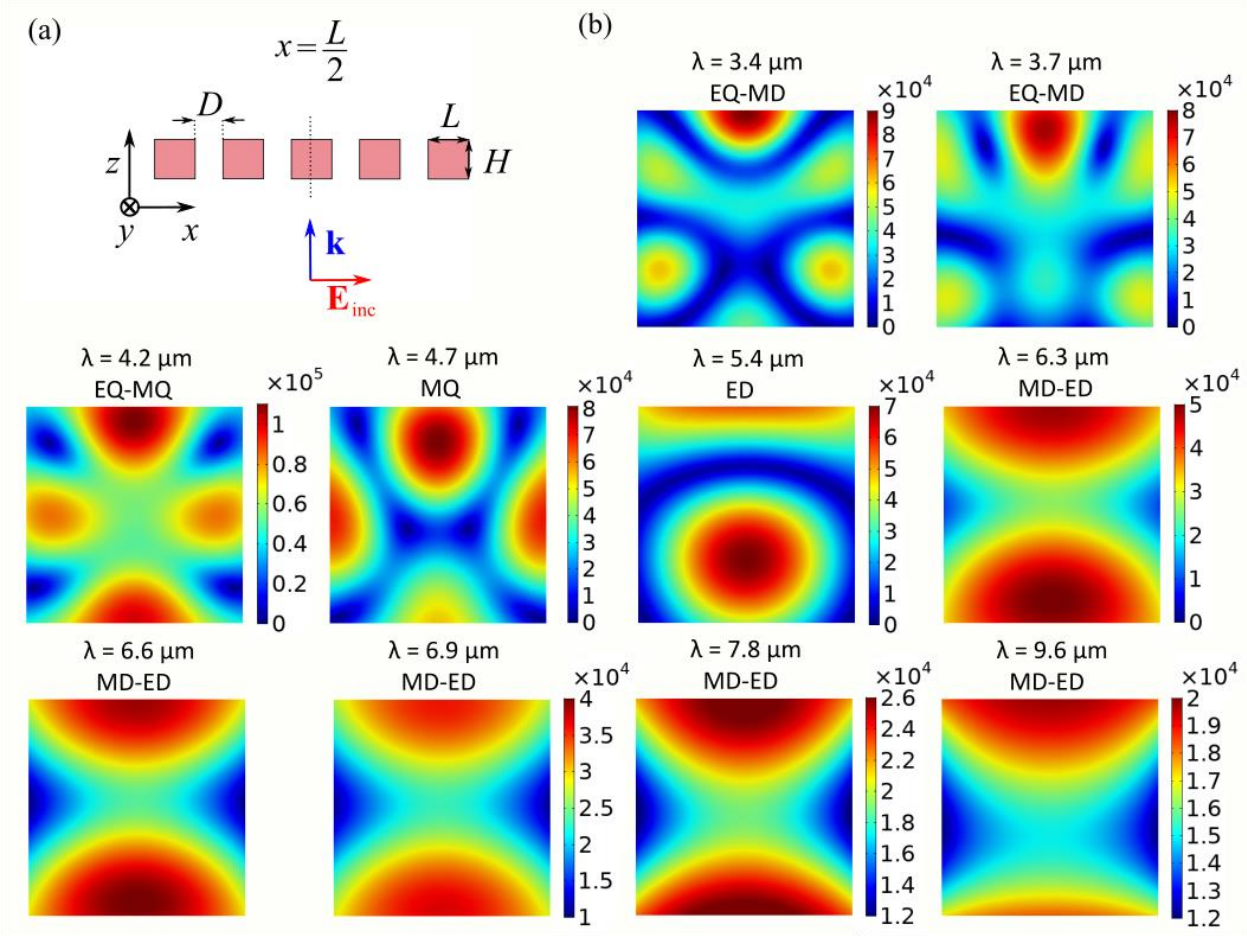

Figure 4-3 Spatial distribution of the electric field within the micro-cubes.
(a) An electric field polarized along the x-axis and propagating in the z-direction is incident on the metamaterial. The magnitude of the incident field, $\mathbf{E}_{\text{inc}}$, is 1 V/m. (b) The spatial distribution of the induced electric field within the micro-cubes at the spectral locations of the NFRHT peaks. The electric field is plotted in the $x = \frac{L}{2}$ plane. The complex refractive index is $\tilde{n}$ = 2.4 + 0.05i, while $L = W = H = D$ = 2 μm and d = 1 μm. The unit for the color bar is V/m.

To study the effect of the refractive index on the spectrum of NFRHT between the Mie resonance-based metamaterials, we increase the refractive index of the micro-cubes to n = 3.5, which is close to the refractive index of germanium telluride [26]. The other parameters of the array remain the same (i.e., κ = 0.05, $L = W = H = D$ = 2 μm, and d = 1 μm). Figure 4-4(a) shows the spectral heat flux for this case. The normalized scattering cross sections for the normal and oblique incidence angles are also plotted in Figs. 3-4(b) and 3-4(c), respectively. Several new peaks appear in the heat flux spectrum with increasing the refractive index. The appearance of the

new peaks can be explained by comparing the scattering cross sections in Fig. 4-4(b) and 3-4(c) with those for a smaller refractive index of n = 2.4 presented in Figs. 3-3(b) and 3-3(c). It is seen that the spectral locations of the Mie modes are redshifted toward longer wavelengths as the refractive index increases. The magnetic modes, namely, the MD and MQ, experience the largest redshift. As n increases, the short-wavelength Mie modes redshift inside the considered spectral band, where they can be thermally excited. This redshift of the peaks results in the appearance of the new peaks in the heat flux spectra when n increases to 3.5.

In total, there are 16 peaks in the spectrum of near-field heat flux which can be identified using the decomposed scattering cross sections in Figs. 3-4(b) and 3-4(c) as well as the spatial distributions of the electric field inside the micro-cubes. The electric field distribution at the peaks' wavelengths is shown in Fig. C-1 of Appendix C [27] for the incident electric field illustrated in Fig. 4-3(a). The wavelengths and the origins of the heat-flux peaks are listed in Fig. 4-4(a). Figure 4-4(a) also shows that the heat flux increases compared to the previous case with a smaller refractive index of n = 2.4. The greatest enhancement is seen in the wavelength range of 8 to 10 μm, where the MD modes are located. Thermal emission and absorption by the micro-cubes due to the MD modes are proportional to the imaginary part of the magnetic polarizability, Im$[\alpha^m]$ [28]. The imaginary part of the magnetic polarizability is proportional to Im$[\varepsilon]$, where ε is the dielectric function of the micro-cubes [28]. As n increases, Im$[\varepsilon]$ and Im$[\alpha^m]$ increase, which results in higher emission and absorption by the micro-cubes thus increasing the heat flux. It should be noted that, similar to the case with a smaller refractive index of n = 2.4, the heat flux is dominated by the contribution from MD modes.

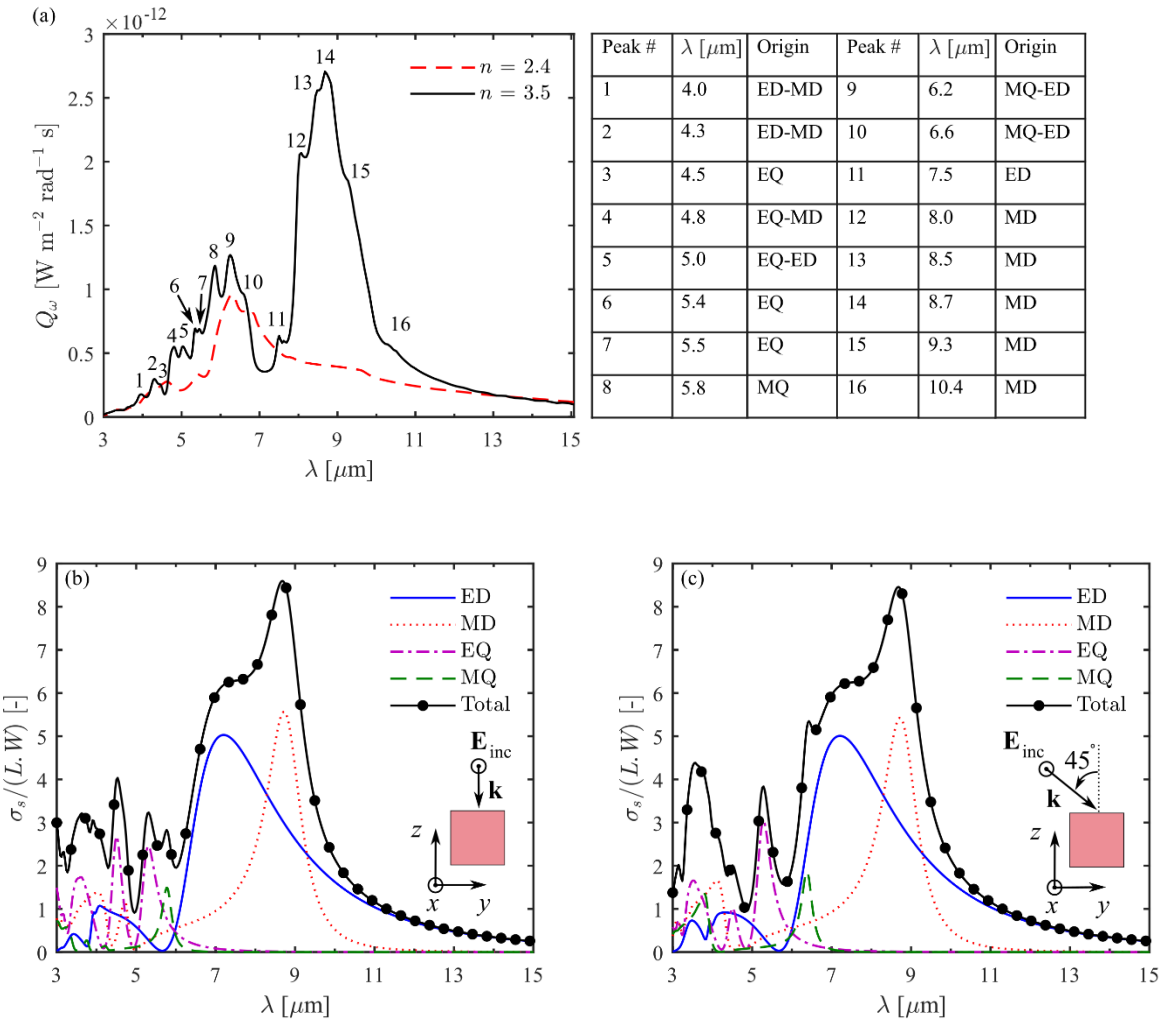

Peak #	λ [μm]	Origin	Peak #	λ [μm]	Origin
1	4.0	ED-MD	9	6.2	MQ-ED
2	4.3	ED-MD	10	6.6	MQ-ED
3	4.5	EQ	11	7.5	ED
4	4.8	EQ-MD	12	8.0	MD
5	5.0	EQ-ED	13	8.5	MD
6	5.4	EQ	14	8.7	MD
7	5.5	EQ	15	9.3	MD
8	5.8	MQ	16	10.4	MD

Figure 4-4 The same as Fig. 4-2 except for a complex refractive index of $\tilde{n}$ = 3.5 + 0.05i.5i.

In Fig. 4-5, the refractive index of the micro-cubes is further increased to n = 5.0, which is approximately the same as the refractive index of tellurium [29]. The decomposed scattering cross sections at the normal and oblique incidence are provided in Figs. C-2(a) and C-2(b) of Appendix C [27] for this case. With further increase of the refractive index, the Mie modes redshift and the heat flux increases further. The heat flux has 16 peaks associated with Mie resonances, which are identified and reported in Fig. 4-5. The heat flux is dominated by the contribution from six peaks located at 6.8 μm, 7.2 μm, 8.1 μm, 8.9 μm, 12.1 μm, and 12.7 μm (peaks numbers 8, 9, 10, 11, 15, and 16 in Fig. 4-5), which are due to the MD, EQ, MQ, ED, MD, and MD, respectively. Figure 4-

5 shows that, similar to the case with n = 3.4, the MD modes significantly contribute to the heat flux. It is also seen that the contributions from the ED and EQ to the heat flux is greater for this case compared to the cases with smaller refractive indices of n = 2.4 and n = 3.5.

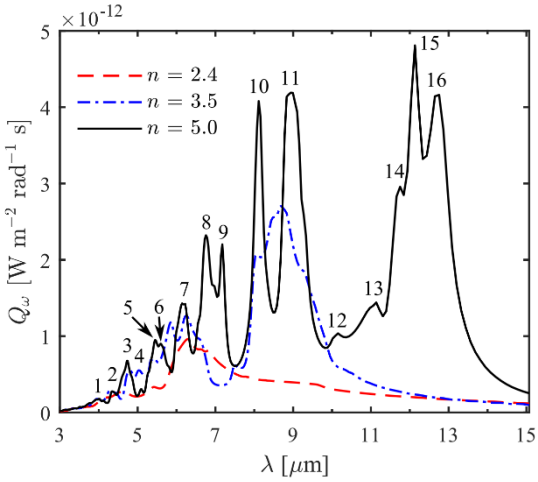

Peak #	λ [μm]	Origin	Peak #	λ [μm]	Origin
1	4.0	ED-MD-EQ-MQ	9	7.2	EQ
2	4.3	ED-MD-EQ-MQ	10	8.1	MQ
3	4.7	MQ	11	8.9	ED
4	5.1	ED-EQ	12	10.2	ED
5	5.5	ED	13	11.1	MD
6	5.6	ED	14	11.8	MD
7	6.2	EQ	15	12.1	MD
8	6.8	MD	16	12.7	MD

Figure 4-5 The same as Fig. 4-2 (a) except for a complex refractive index of $\tilde{n}$ = 5.0 + 0.05i.

Next, we study the effect of extinction coefficient, κ, on the spectrum of heat flux. Figure 4-6(a) shows the NFRHT between two Mie resonance-based metamaterials with n = 5.0 and three levels of extinction coefficient, namely, κ = 0.05, 0.1, and 0.5. With increasing κ from 0.05 to 0.1, the spectral locations of the Mie resonances do not change. However, there is an enhancement of the heat flux at all wavelengths. As κ increases, Im[ε] and thus the thermally fluctuating current of the micro-cubes, given by the fluctuational electrodynamics [1,2], increase at all wavelengths. With increasing κ further to κ = 0.5, the broadband enhancement of the heat flux and the damping of the Mie resonances result in a broadband spectrum for the heat flux. Figure 4-6(a) shows that the extinction coefficient is a key factor in determining the shape of the heat-flux spectrum (spectrally-selective or broadband).

The effect of micro-cube interspacing, D, on the NFRHT between the two Mie resonance-based metamaterials is studied in Fig. 4-6(b). This figure shows the heat flux for three interspacing

of D = 2 μm, 1 μm, and 100 nm as well as for a thin film with the same material and thickness as the metamaterials. The refractive index is fixed at $\tilde{n}$ = 5.0 + 0.05i, while the sizes of the micro-cubes and vacuum gap remain the same as in the previous cases (i.e., $L = W = H$ = 2 μm and d = 1 μm). As D reduces from 2 μm to 1 μm, the heat flux increases in a broadband manner (i.e., at both resonance and non-resonance wavelengths). This enhancement is due to a larger volume of the Mie resonators per unit area of the metamaterials for the smaller interspacing of D = 1 μm. Reducing the interspacing to D = 1 μm also results in splitting of some of the Mie resonances such as the ED resonance at 10.2 μm. The resonance splitting is due to the spatial overlap of the Mie modes of the neighboring micro-cubes as described before. When D = 100 nm, the neighboring micro-cubes are placed at a near-field distance from each other. At near-field distances, the destructive interactions between the Mie modes result in damping of the heat-flux peaks except for the dominant dipole mode between 8 μm and 10 μm, which is split into two peaks. However, the heat flux increases in a broadband manner when D reduces to 100 nm. As $D \rightarrow 0$, the spectrum of NFRHT approaches that for a thin film as shown in Fig. 7b. It should be noted that the four peaks observed in the spectrum of heat flux for the thin films at 4.0 μm, 5.0 μm, 6.6 μm, and 9.8 μm are due to the fifth, fourth, third, and second Fabry–Pérot interference resonances, respectively. The Fabry–Pérot resonances are excited inside the thin films at wavelengths $\lambda = \frac{2nH}{N}$, where H (= 2 μm) and N are the thickness of the film and the order of the resonance, respectively. It should also be noted that, unlike indicated by previous studies [16-20], the total heat flux for the Mie resonance-based metamaterials is less than that for the thin films with the same refractive index and thickness. However, the Mie resonance-based metamaterials provide more degrees of freedom for designing the spectrum of NFRHT when compared to thin films.

To study the spectrum of NFRHT at smaller separation gaps, the spectral heat flux between two Mie resonance-based metamaterials separated by a gap of size d = 100 nm is compared with the one for d = 1 μm in Fig. 4-6(c). The complex refractive index of the micro-cubes is assumed to be $\tilde{n}$ = 5.0 + 0.05i for both cases. As expected, the heat flux increases as the gap size decreases. However, as the gap size decreases by one order of magnitude, the total (spectrally integrated) heat flux increases only by a factor of 2. This shows that the Mie resonance-based metamaterials are suitable for intermediate near-field gaps (i.e., d > 500 nm) which are experimentally more attainable. With decreasing the separation gap, the spectral locations of some of the Mie peaks such as the EQ slightly redshift. Additionally, the spatial overlap of the Mie modes results in splitting of the ED, MD, and MQ modes [see Fig. 4-6(c)].

Lastly, we show that the spectral locations and the relative intensity of the NFRHT peaks can be modulated to a great extent via varying the geometry of the Mie resonators. By changing the geometry of the resonators, it is possible to have several scattered peaks in the spectrum, or to spectrally overlap the Mie modes into a dominant peak. For example, Fig. 4-6(d) compares NFRHT for the micro-cube geometry studied so far ($L = W = H$ = 2 μm) with that for a cuboidal geometry with edge lengths of $L = W$ = 1.26 μm and H = 5.04 μm. The former has a height over width of $\frac{H}{W}$ = 1, while this ratio for the latter is $\frac{H}{W}$ = 4. The volume (= 8 μm^3) and the array pitch (= 4 μm), and thus the emitting volume per unit area of the metamaterials, are the same for both geometries. The refractive index is assumed to be $\tilde{n}$ = 5.0 + 0.05i for both cases. It is seen that for the case with $\frac{H}{W}$ = 1, there are four dominant peaks at 8.1 μm, 8.9 μm, 12.1 μm, and 12.7 μm, which, as discussed before, are due to the MQ, ED, MD, and MD modes, respectively. When $\frac{H}{W}$ = 4, the MD modes at 12.1 μm and 12.7 μm blueshift, while the MQ mode at 8.1 μm and the ED

mode at 8.9 μm redshift. With the shift of the modes with changing the geometry, the MD, MQ, and ED modes spectrally overlap which results in a dominant peak in the spectrum of the near-field heat flux as seen in Fig. 4-6(d). In addition to the ratio $\frac{H}{W}$, the location and relative magnitude of the heat flux peaks can be tuned by varying the ratio $\frac{L}{W}$ of the cubes (for example, the spectral heat flux for two cases with $\frac{L}{W}$ = 1.0 and $\frac{L}{W}$ = 1.5 can be compared in Fig. C-3 of Appendix C).

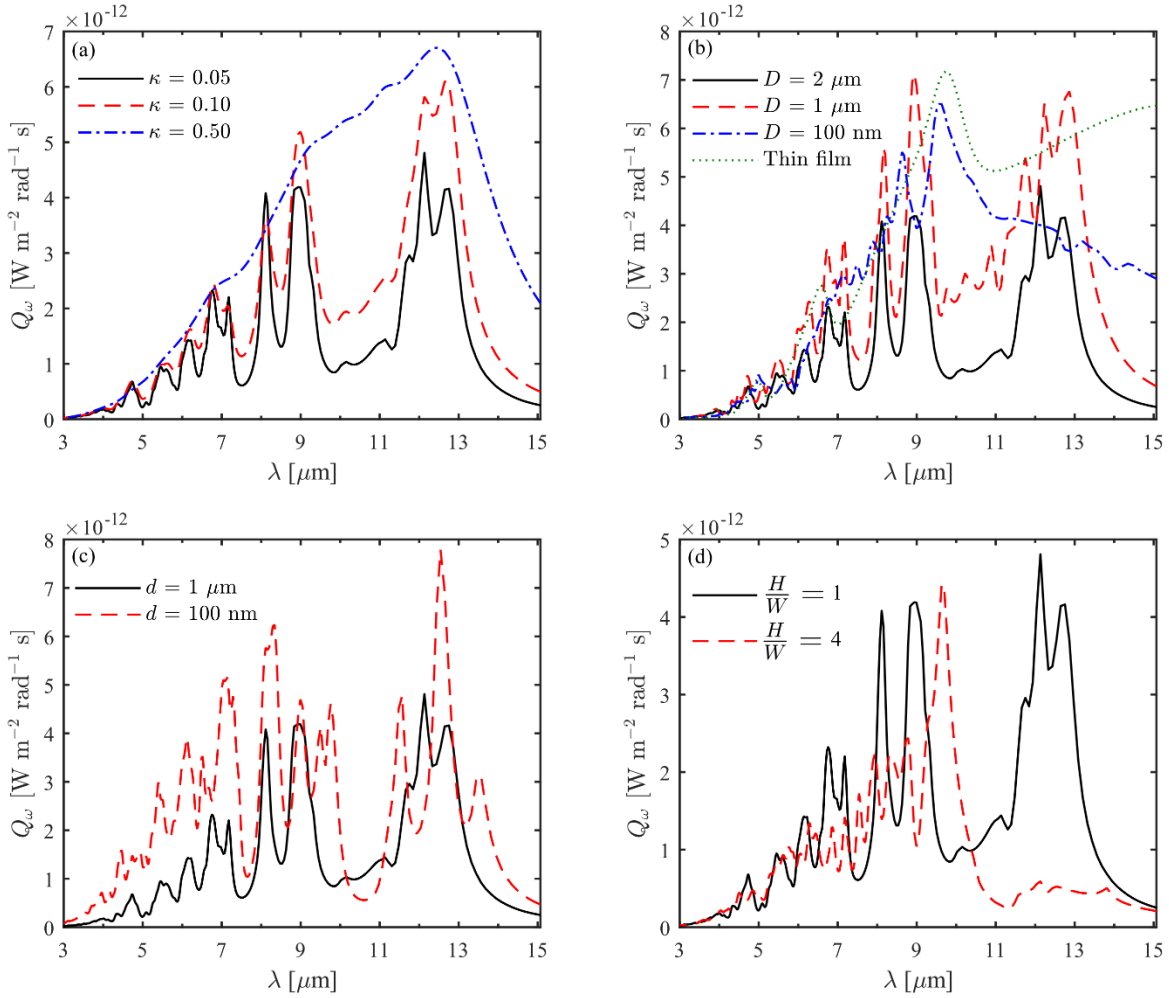

Figure 4-6 The effect of extinction coefficient, cube interspacing, separation gap, and geometry on the spectrum of near-field heat flux.

(a) The effect of the extinction coefficient, κ, on the heat flux. $L = W = H = D$ = 2 μm, n = 5.0, and d = 1 μm (b) The effect of cube interspacing, D, on the heat flux. $L = W = H$ = 2 μm, $\tilde{n}$ = 5.0 + 0.05i, and d = 1 μm. (c) The effect of the separation gap, d, on the heat flux. $L = W = H = D$ = 2 μm and $\tilde{n}$ = 5.0 + 0.05i. (d) The effect of the geometry of the Mie resonators on the heat flux. $\tilde{n}$ = 5.0 + 0.05i, d = 1 μm, and $L = W$. The array pitch is 4 μm, and the volume of the Mie resonators is 8 μm^3.

It should be noted that even though a refractive index of n = 5.0 is assumed in Fig. 4-6, the effects of κ, D, d, and $\frac{H}{W}$ on the spectrum of near-field heat flux for a smaller refractive index of n = 2.4 remain the same as those found for n = 5.0. The spectral heat flux for a refractive index of n = 2.4 as a function of κ, D, d, and $\frac{H}{W}$ is shown in Fig. C-4 of Appendix C [27].

4.5 Conclusion

The spectrum of near-field radiative heat transfer between two Mie resonance-based metamaterials is studied using non-approximate numerical simulations. The effects of the refractive index, extinction coefficient, shape, and interspacing of the Mie resonators as well as the separation gap of the two metamaterials on the near-field spectrum are analyzed. It was shown that as the refractive index increases, the Mie resonances redshift and the heat flux increases. The number of Mie resonances that can thermally be excited increases with increasing the refractive index. As the extinction coefficient increases, the heat flux increases at all wavelengths and the Mie resonances start to damp until the spectrum eventually becomes broadband. It was also found that as the interspacing of the Mie resonators reduces, the interactions between neighboring resonators initially cause resonance splitting and eventually results in disappearance of most of the Mie peaks except for the electric dipole mode. The heat flux monotonically increases with decreasing the interspacing and eventually converges to that for a thin film with the same thickness as the Mie resonators. With decreasing the separation gap of the metamaterials, the heat flux increases while the Mie resonances split into a few peaks due to the spatial overlap of the modes. Lastly, it was shown that the spectral locations of the Mie resonances are significantly dependent on the geometry of the Mie resonators. By modulating the geometry, the Mie resonances can spectrally overlap and form a sharp peak in the heat-flux spectrum. The results of this study provide

insight into the mechanisms of near-field radiative heat transfer between Mie resonance-based metamaterials and can provide a guide for designing materials with desired near-field spectrum.

4.6 Acknowledgement

This work is supported by the National Science Foundation under Grant No. CBET-1804360.

4.7 References

[1] Zhang, Z.M., 2020. *Nano/microscale heat transfer*. Cham: Springer.

[2] Joulain, K., Mulet, J.P., Marquier, F., Carminati, R. and Greffet, J.J., 2005. Surface electromagnetic waves thermally excited: Radiative heat transfer, coherence properties and Casimir forces revisited in the near field. *Surface Science Reports*, *57*(3-4), pp.59-112.

[3] Lucchesi, C., Cakiroglu, D., Perez, J.P., Taliercio, T., Tournié, E., Chapuis, P.O. and Vaillon, R., 2021. Near-field thermophotovoltaic conversion with high electrical power density and cell efficiency above 14%. *Nano Letters*, *21*(11), pp.4524-4529.

[4] Legendre, J. and Chapuis, P.O., 2022. Overcoming non-radiative losses with AlGaAs PIN junctions for near-field thermophotonic energy harvesting. *Applied Physics Letters*, *121*(19).

[5] Otey, C.R., Lau, W.T. and Fan, S., 2010. Thermal rectification through vacuum. *Physical review letters*, *104*(15), p.154301.

[6] Basu, S. and Francoeur, M., 2011. Near-field radiative transfer based thermal rectification using doped silicon. *Applied Physics Letters*, *98*(11).

[7] Zhu, L., Fiorino, A., Thompson, D., Mittapally, R., Meyhofer, E. and Reddy, P., 2019. Near-field photonic cooling through control of the chemical potential of photons. *Nature*, *566*(7743), pp.239-244.

[8] Cai, W. and Shalaev, V., 2010. *Optical metamaterials*. New York: Springer.

[9] Mirmoosa, M.S., Omelyanovich, M. and Simovski, C.R., 2016. Microgap thermophotovoltaic systems with low emission temperature and high electric output. *Journal of Optics*, *18*(11), p.115104.

[10] Li, K., Wu, S., Cao, S., Cai, Q., Ye, Q., Liu, X. and Wu, X., 2021. Transient performance of a nanowire-based near-field thermophotovoltaic system. *Applied Thermal Engineering*, *192*, p.116918.

[11] Taniguchi, Y., Isobe, K. and Hanamura, K., 2021. Enhancement of spectrally controlled near-field radiation transfer by magnetic polariton generated by metal–insulator–metal structures. *Applied Thermal Engineering*, *183*, p.116041.

[12] Chang, J.Y., Yang, Y. and Wang, L., 2015. Tungsten nanowire based hyperbolic metamaterial emitters for near-field thermophotovoltaic applications. *International Journal of Heat and Mass Transfer*, *87*, pp.237-247.

[13] Yu, H., Duan, Y. and Yang, Z., 2018. Selectively enhanced near-field radiative transfer between plasmonic emitter and GaSb with nanohole and nanowire periodic arrays for thermophotovoltaics. *International Journal of Heat and Mass Transfer*, *123*, pp.67-74.

[14] Watjen, J.I., Liu, X.L., Zhao, B. and Zhang, Z.M., 2017. A computational simulation of using tungsten gratings in near-field thermophotovoltaic devices. *Journal of Heat Transfer*, *139*(5), p.052704.

[15] Fernández-Hurtado, V., García-Vidal, F.J., Fan, S. and Cuevas, J.C., 2017. Enhancing near-field radiative heat transfer with Si-based metasurfaces. *Physical review letters*, *118*(20), p.203901.

[16] Francoeur, M., Basu, S. and Petersen, S.J., 2011. Electric and magnetic surface polariton mediated near-field radiative heat transfer between metamaterials made of silicon carbide particles. *Optics express*, *19*(20), pp.18774-18788.

[17] Petersen, S.J., Basu, S., Raeymaekers, B. and Francoeur, M., 2013. Tuning near-field thermal radiative properties by quantifying sensitivity of Mie resonance-based metamaterial design parameters. *Journal of Quantitative Spectroscopy and Radiative Transfer*, *129*, pp.277-286.

[18] Petersen, S.J., Basu, S. and Francoeur, M., 2013. Near-field thermal emission from metamaterials. *Photonics and Nanostructures-Fundamentals and Applications*, *11*(3), pp.167-181.

[19] Ghanekar, A., Tian, Y., Zhang, S., Cui, Y. and Zheng, Y., 2017. Mie-metamaterials-based thermal emitter for near-field thermophotovoltaic systems. *Materials*, *10*(8), p.885.

[20] Hu, Y., Li, H., Zhang, Y., Zhu, Y. and Yang, Y., 2020. Enhanced near-field radiation in both TE and TM waves through excitation of Mie resonance. *Physical Review B*, *102*(12), p.125434.

[21] Zare, S., Pouria, R. and Edalatpour, S., 2021. Validity of the effective medium theory for modeling near-field thermal emission by nanowire arrays. *Journal of Quantitative Spectroscopy and Radiative Transfer*, *261*, p.107482.

[22] Chen, K., Zhao, B. and Fan, S., 2018. MESH: A free electromagnetic solver for far-field and near-field radiative heat transfer for layered periodic structures. *Computer Physics Communications*, *231*, pp.163-172.

[23] Alaee, R., Rockstuhl, C. and Fernandez-Corbaton, I., 2018. An electromagnetic multipole expansion beyond the long-wavelength approximation. *Optics Communications*, *407*, pp.17-21.

[24] Li, D., Jiang, M., Qi, H., Wang, Q. and Liu, C., 2016. Optical Constants of Zinc Selenide at 373 and 423 K in the Wavelength Range of 2–15 μm. *Journal of Applied Spectroscopy*, *83*, pp.512-516.

[25] Pouria, R. and Edalatpour, S., 2024. Tuning the spectrum of near-field radiative heat transfer using Mie resonance based metamaterials. *Physical Review B*, *109*(4), p.045407.

[26] Kotlikov, E.N., Ivanov, V.A., Pogareva, V.G. and Khonineva, E.V., 2000. Study of optical constants of PbTe and GeTe films. *Optics and Spectroscopy*, *88*, pp.718-720.

[27] See Supplemental Material at https://journals.aps.org/ PhysRevB.109.045407 for the spatial distribution of the induced electric field within the microcubes for a refractive index of 3.5, the multipole expansion of the scattering cross section for a refractive index of 5.0, the effect of cubes' length to width ratio on the spectrum of near-field heat flux, and the effect of metamaterials' parameters on the spectrum of near-field heat flux for a refractive index of 2.4.

[28] Chapuis, P.O., Laroche, M., Volz, S. and Greffet, J.J., 2008. Radiative heat transfer between metallic nanoparticles. *Applied Physics Letters*, *92*(20).

[29] Ginn, J.C., Brener, I., Peters, D.W., Wendt, J.R., Stevens, J.O., Hines, P.F., Basilio, L.I., Warne, L.K., Ihlefeld, J.F., Clem, P.G. and Sinclair, M.B., 2012. Realizing optical magnetism from dielectric metamaterials. *Physical review letters*, *108*(9), p.097402.

Chapter 5
Conclusions and Recommendations

While the main goal of this dissertation is to show the potential of metamaterials for engineering the spectrum of thermal radiation in the far-field and near-field regimes, it also aims at covering the knowledge gap that exists in the literature of thermal radiation for two of the mechanisms that are less explored; namely LSPh modes and Mie resonance modes. The main results and contributions of this research as well as recommendations for future studies are discussed hereafter.

5.1 Engineering Far-Field Thermal Emission with Metamaterials Supporting LSPh modes

In summary, this study investigates far-field thermal emission from non-diffractive arrays of subwavelength silicon carbide nanoparticles, with a specific emphasis on the influence of LSPh modes. The strategic utilization of these resonant modes underscores the feasibility of approaching the blackbody limit for a wide range of emission angles. Achieving the blackbody limit for thermal emissivity is possible because of overlapping of the LSPh modes and hybrid waveguide-SPhP modes. This effect is realized by optimizing the interparticle spacing between the subwavelength constituents, i.e., nanopillars. It was seen that when the interparticle spacing is above the optimized value, the resonance modes are spectrally scattered with low values of emissivity while reducing the interparticle spacing below the optimized value reduces the dipole moments of nanopillars due to the increased negative impact of near-field interaction between the nanopillars. We also found that far-field thermal emission from nanoparticles that support LSPh modes is highly independent of emission angle. The numerical results for far-field spectral, directional emissivity are backed up with experimental measurements using a direct measurement technique that was developed in our lab. The angular independence of far-field thermal emission from LSPh modes makes them

suitable for practical applications, such as thermal management for electronic devices and thermophotovoltaic energy harvesting. In electronic devices, effective thermal management is crucial to prevent overheating and optimize performance. The near-unity thermal emissivity achieved through LSPh modes could be used for heat dissipation, improving device reliability and longevity. The angle independent thermal emission facilitated by metamaterials that support LSPh modes makes these types of metamaterials ideal for efficient thermal energy harvesting, potentially advancing renewable energy technologies and offering a more sustainable approach to energy generation.

5.2 Engineering Far-Field Thermal Emission with Mie Resonance-Based Metamaterials

Dielectric materials that support special resonance modes such as surface phonons are limited in number, and they may not be suitable for every application. Additionally, the spectral range where surface phonon modes are active for these dielectric materials is also limited. Thus, it becomes crucial to find a mechanism for engineering the spectrum of far-field thermal radiation with more spectral freedom for dielectric materials that do not support surface phonon modes. For this purpose, we proposed studying far-field thermal emission from Mie resonance-based metamaterials. More specifically, we investigated periodic arrays of Mie resonance-based microcuboids made of silicon carbide. Silicon carbide does not support surface phonon modes outside its Reststrahlen band bound by ~10-12.5 μm, since the real part of the dielectric function for silicon carbide is positive outside of this band. By carefully choosing the size of the microcuboids, we showed that it is possible to tune the Mie resonances to occur outside of Reststrahlen band of silicon carbide. It was found that when microcuboids of silicon carbide with large scattering cross sections (comparable to geometric cross section of the microcubes) are laid on a flat substrate made of the same material, the metamaterial can achieve near-unity emissivity

over a wide range of wavelengths and angles. The choice of SiC as the substrate was strategic, given its inherent properties and relevance in various applications, including optoelectronics, thermal management, and energy harvesting. The broadband improvement achieved in emissivity was a noteworthy outcome, as it reaches the blackbody limit on both sides of the Reststrahlen band. A crucial aspect elucidated in the study was the coupling effect between Mie resonance-based microcubes and the SiC substrate. The substrate, being composed of the same material as the microcuboids, plays a pivotal role in achieving perfect emissivity for Mie resonance-based configurations. This coupling effect creates a strong tendency for forward scattering within the resonator, forming a leaky channel that enhances thermal emission. Understanding and harnessing this coupling effect contributes to the optimization of the metamaterial design for achieving superior thermal radiation properties. Moreover, the study explored the potential for omnidirectional improvement in thermal radiation. Numerical simulations suggested that the enhancement of thermal radiation remains consistent up to 60 degrees, indicating a wide-angle efficacy. This was a particularly promising result, as it implied that the proposed metamaterial configuration could find applications in scenarios where thermal radiation needs to be enhanced across various viewing angles. The omnidirectional improvement further extends the versatility of this metamaterial in practical applications, making it a potential candidate for diverse fields such as aerospace, electronics, and solar energy. Crucially, the study's theoretical predictions are supported by experimental validation, underscoring the robustness and reliability of the proposed approach.

5.3 Engineering The Spectrum of NFRHT Using Mie Resonance-Based Metamaterials

In this work, we studied NFRHT between Mie resonance-based metamaterials in a non-approximate manner using the Fourier modal method. Using an exact multipole decomposition

method, the electromagnetic response of the Mie resonators was characterized by contributions from various multipoles and the origins of the peaks in the near-field spectra were identified. It was found that the refractive index, extinction coefficient, shape, and interparticle spacing of the Mie resonators, as well as the separation distance of the metamaterials have significant effects on both the magnitude and the spectrum of NFRHT. The refractive index of the metamaterial emerges as a critical factor, with an increase leading to a rise in heat flux and a spectral redshift of Mie resonances. This finding suggests that manipulating the refractive index provides a viable avenue for tailoring the heat transfer characteristics of Mie resonance-based metamaterials. Additionally, the study underscores the role of the extinction coefficient, showing that an increase results in higher near-field heat flux. However, this is accompanied by the damping of Mie resonances, ultimately leading to a broadband spectrum for heat flux. The delicate balance between maximizing heat transfer and maintaining spectral characteristics requires careful consideration in the design process. The research also sheds light on the nuanced effects of the shape and interspacing of Mie resonators on NFRHT. The observed resonance splitting as the distance between resonators approaches the nanometer scale introduces an intriguing aspect to the study. This phenomenon implies that the spatial arrangement of Mie resonators can give rise to distinctive features in the near-field spectrum. Understanding and harnessing this resonance splitting could open new possibilities for tailoring heat transfer in metamaterials for specific applications. The significance of the geometry of Mie resonators in shaping the spectrum of NFRHT is a noteworthy finding with implications for practical applications. The ability to carefully design the geometry to either produce scattered resonances or overlap them into a single, strong peak highlights the versatility of Mie resonance-based metamaterials. This design flexibility allows researchers to tailor the near-field heat transfer characteristics according to specific needs, whether it be

achieving a monochromatic heat transfer or creating a spectrum with multiple peaks. It should also be mentioned that, in all cases considered in this study, the NFRHT between the Mie resonance-based metamaterials is smaller than that between two thin films with the same material and thickness as the metamaterials.

5.4 Recommendations for future research

Future research in the field of engineering far-field thermal emission with metamaterials should focus on several key areas to advance the understanding and application of these materials. Firstly, exploring a broader range of dielectric materials that support LSPh and Mie resonance modes beyond silicon carbide could lead to more versatile and efficient thermal emission systems. Investigating materials with different dielectric properties may reveal new resonant behaviors and optimize the spectral and angular characteristics of thermal emission. Additionally, further studies should consider the impact of varying environmental conditions, such as temperature and pressure, on the performance of these metamaterials to ensure their robustness in practical applications. Advanced numerical modeling techniques, combined with experimental validation, can be employed to refine the design and optimize the interparticle spacing and geometry of the resonators for maximum emissivity. Moreover, integrating these metamaterials into complex systems, such as multi-layered structures or hybrid materials, could enhance their thermal management capabilities and expand their applicability in areas like thermophotovoltaic energy harvesting and electronic device cooling. Finally, long-term durability and stability studies are essential to understand the performance of these materials over extended periods, ensuring their reliability for industrial and commercial use. By addressing these research directions, the field can move towards developing more efficient, sustainable, and versatile thermal emission technologies.

In terms of near-field thermal radiation, one recommendation for future research could be the experimental analysis of Mie resonance-based metamaterials to validate the accuracy of numerical results. Experimental confirmation not only substantiates the numerical simulations but also establishes a foundation for further research and development in this direction. The successful experimental validation reinforces the practical feasibility of implementing this metamaterial for tuning the spectrum of near-field thermal radiation. Utilizing an in-house novel technique that couples evanescent waves to a high-refractive-index internal reflection element (IRE), we can measure the near-field thermal radiation spectra of Mie resonance-based metamaterials. This approach allows for a detailed examination of the specific peaks and spectral characteristics associated with Mie resonances, providing deeper insights into their interaction mechanisms and optimizing their design for various applications.

BIBLIOGRAPHY

Alaee, R., Rockstuhl, C. and Fernandez-Corbaton, I., 2018. An electromagnetic multipole expansion beyond the long-wavelength approximation. *Optics Communications*, *407*, pp.17-21.

Amemiya, T., Yamasaki, S., Kanazawa, T., Gu, Z., Inoue, D., Ishikawa, A., Nishiyama, N., Tanaka, T., Urakami, T. and Arai, S., 2018, May. Infrared Invisibility Cloak Using Rolled Metamaterial Film. In *2018 Conference on Lasers and Electro-Optics (CLEO)* (pp. 1-2). IEEE.

Arnold, C., Marquier, F., Garin, M., Pardo, F., Collin, S., Bardou, N., Pelouard, J.L. and Greffet, J.J., 2012. Coherent thermal infrared emission by two-dimensional silicon carbide gratings. *Physical Review B—Condensed Matter and Materials Physics*, *86*(3), p.035316.

Arnoldus, H.F., 2001. Representation of the near-field, middle-field, and far-field electromagnetic Green's functions in reciprocal space. *JOSA B*, *18*(4), pp.547-555.

Basu, S. and Francoeur, M., 2011. Near-field radiative transfer based thermal rectification using doped silicon. *Applied Physics Letters*, *98*(11).

Bezares, F.J., Long, J.P., Glembocki, O.J., Guo, J., Rendell, R.W., Kasica, R., Shirey, L., Owrutsky, J.C. and Caldwell, J.D., 2013. Mie resonance-enhanced light absorption in periodic silicon nanopillar arrays. *Optics Express*, *21*(23), pp.27587-27601.

Bhatt, G.R., Zhao, B., Roberts, S., Datta, I., Mohanty, A., Lin, T., Hartmann, J.M., St-Gelais, R., Fan, S. and Lipson, M., 2020. Integrated near-field thermo-photovoltaics for heat recycling. *Nature communications*, *11*(1), p.2545.

Biehs, S.A., Tschikin, M. and Ben-Abdallah, P., 2012. Hyperbolic metamaterials as an analog of a blackbody in the near field. *Physical review letters*, *109*(10), p.104301.

Biehs, S.A., Tschikin, M., Messina, R. and Ben-Abdallah, P., 2013. Super-Planckian near-field thermal emission with phonon-polaritonic hyperbolic metamaterials. *Applied Physics Letters*, *102*(13).

Cai, W. and Shalaev, V., 2010. *Optical metamaterials*. New York: Springer.

Caldwell, J.D., Glembocki, O.J., Francescato, Y., Sharac, N., Giannini, V., Bezares, F.J., Long, J.P., Owrutsky, J.C., Vurgaftman, I., Tischler, J.G. and Wheeler, V.D., 2013. Low-loss, extreme subdiffraction photon confinement via silicon carbide localized surface phonon polariton resonators. Nano letters, 13(8), pp.3690-3697.

Caldwell, J.D., Lindsay, L., Giannini, V., Vurgaftman, I., Reinecke, T.L., Maier, S.A. and Glembocki, O.J., 2015. Low-loss, infrared and terahertz nanophotonics using surface phonon polaritons. *Nanophotonics*, *4*(1), pp.44-68.

Chalabi, H., Alù, A. and Brongersma, M.L., 2016. Focused thermal emission from a nanostructured SiC surface. *Physical Review B*, *94*(9), p.094307.

Chalabi, H.; Alù, A.; Brongersma, M. L. Focused Thermal Emission from a Nanostructured SiC Surface. *Physical Review B* **2016**, *94* (9), 094307.

Chang, J.Y., Yang, Y. and Wang, L., 2015. Tungsten nanowire based hyperbolic metamaterial emitters for near-field thermophotovoltaic applications. *International Journal of Heat and Mass Transfer*, *87*, pp.237-247.

Chapuis, P.O., Laroche, M., Volz, S. and Greffet, J.J., 2008. Radiative heat transfer between metallic nanoparticles. *Applied Physics Letters*, *92*(20).

Chen, D., Dong, J., Yang, J., Hua, Y., Li, G., Guo, C., Xie, C., Liu, M. and Liu, Q., 2018. Realization of near-perfect absorption in the whole reststrahlen band of SiC. *Nanoscale*, *10*(20), pp.9450-9454.

Chen, K., Zhao, B. and Fan, S., 2018. MESH: A free electromagnetic solver for far-field and near-field radiative heat transfer for layered periodic structures. *Computer Physics Communications*, *231*, pp.163-172.

Chen, Y., Francescato, Y., Caldwell, J.D., Giannini, V., Maß, T.W., Glembocki, O.J., Bezares, F.J., Taubner, T., Kasica, R., Hong, M. and Maier, S.A., 2014. Spectral tuning of localized surface phonon polariton resonators for low-loss mid-IR applications. *Acs Photonics*, *1*(8), pp.718-724.

Dahan, N., Niv, A., Biener, G., Gorodetski, Y., Kleiner, V. and Hasman, E., 2007. Enhanced coherency of thermal emission: Beyond the limitation imposed by delocalized surface waves. *Physical Review B—Condensed Matter and Materials Physics*, *76*(4), p.045427.

Dang, P.T., Kim, J., Nguyen, T.K., Le, K.Q. and Lee, J.H., 2021. Ultra-broadband metamaterial absorber for high solar thermal energy conversion efficiency. *Physica B: Condensed Matter*, *620*, p.413261.

David Jackson, J. *Classical Electrodynamics*, 3rd edition.; Wiley, 1998.

Davidsen, R.S., Li, H., To, A., Wang, X., Han, A., An, J., Colwell, J., Chan, C., Wenham, A., Schmidt, M.S. and Boisen, A., 2016. Black silicon laser-doped selective emitter solar cell with 18.1% efficiency. *Solar Energy Materials and Solar Cells*, *144*, pp.740-747.

Didari, A. and Mengüç, M.P., 2015. Near-to far-field coherent thermal emission by surfaces coated by nanoparticles and the evaluation of effective medium theory. *Optics express*, *23*(11), pp.A547-A552.

Edalatpour, S. and Francoeur, M., 2013. Size effect on the emissivity of thin films. *Journal of Quantitative Spectroscopy and Radiative Transfer*, *118*, pp.75-85.

Edalatpour, S., 2019. Near-field thermal emission by periodic arrays. *Physical Review E*, *99*(6), p.063308.

Edalatpour, S., Čuma, M., Trueax, T., Backman, R. and Francoeur, M., 2015. Convergence analysis of the thermal discrete dipole approximation. *Physical Review E*, *91*(6), p.063307.

Enoch, S. and Bonod, N. eds., 2012. *Plasmonics: from basics to advanced topics* (Vol. 167). Springer.

Fernández-Hurtado, V., García-Vidal, F.J., Fan, S. and Cuevas, J.C., 2017. Enhancing near-field radiative heat transfer with Si-based metasurfaces. *Physical review letters*, *118*(20), p.203901.

Foteinopoulou, S., Devarapu, G.C.R., Subramania, G.S., Krishna, S. and Wasserman, D., 2019. Phonon-polaritonics: enabling powerful capabilities for infrared photonics. *Nanophotonics*, *8*(12), pp.2129-2175.

Francoeur, M., Basu, S. and Petersen, S.J., 2011. Electric and magnetic surface polariton mediated near-field radiative heat transfer between metamaterials made of silicon carbide particles. *Optics express*, *19*(20), pp.18774-18788.

Gao, M., Han, X., Chen, F., Zhou, W., Liu, P., Shan, Y., Chen, Y., Li, J., Zhang, R., Wang, S. and Zhang, Q., 2019. Approach to fabricating high-performance cooler with near-ideal emissive spectrum for above-ambient air temperature radiative cooling. *Solar Energy Materials and Solar Cells*, *200*, p.110013.

Garcia-Vidal, F.J., Sanchez-Dehesa, J., Dechelette, A., Bustarret, E., Lopez-Rios, T., Fournier, T. and Pannetier, B., 1999. Localized surface plasmons in lamellar metallic gratings. *Journal of Lightwave technology*, *17*(11), p.2191.

Ghanekar, A., Lin, L. and Zheng, Y., 2016. Novel and efficient Mie-metamaterial thermal emitter for thermophotovoltaic systems. Optics express, 24(10), pp.A868-A877.

Ghanekar, A., Tian, Y., Zhang, S., Cui, Y. and Zheng, Y., 2017. Mie-metamaterials-based thermal emitter for near-field thermophotovoltaic systems. *Materials*, *10*(8), p.885.

Ghanekar, A., Tian, Y., Zhang, S., Cui, Y. and Zheng, Y., 2017. Mie-metamaterials-based thermal emitter for near-field thermophotovoltaic systems. *Materials*, *10*(8), p.885.

Ginn, J.C., Brener, I., Peters, D.W., Wendt, J.R., Stevens, J.O., Hines, P.F., Basilio, L.I., Warne, L.K., Ihlefeld, J.F., Clem, P.G. and Sinclair, M.B., 2012. Realizing optical magnetism from dielectric metamaterials. *Physical review letters*, *108*(9), p.097402.

Gong, Y., Wang, Z., Li, K., Uggalla, L., Huang, J., Copner, N., Zhou, Y., Qiao, D. and Zhu, J., 2017. Highly efficient and broadband mid-infrared metamaterial thermal emitter for optical gas sensing. *Optics letters*, *42*(21), pp.4537-4540.

Greffet, J.J., Carminati, R., Joulain, K., Mulet, J.P., Mainguy, S. and Chen, Y., 2002. Coherent emission of light by thermal sources. *Nature*, *416*(6876), pp.61-64.

Gubbin, C.R., Berte, R., Meeker, M.A., Giles, A.J., Ellis, C.T., Tischler, J.G., Wheeler, V.D., Maier, S.A., Caldwell, J.D. and De Liberato, S., 2019. Hybrid longitudinal-transverse phonon polaritons. Nature communications, 10(1), p.1682.

Gubbin, C.R., Maier, S.A. and De Liberato, S., 2017. Theoretical investigation of phonon polaritons in SiC micropillar resonators. *Physical review B*, *95*(3), p.035313.

Gubbin, C.R., Martini, F., Politi, A., Maier, S.A. and De Liberato, S., 2016. Strong and coherent coupling between localized and propagating phonon polaritons. *Physical review letters*, *116*(24), p.246402.

Guha, B., Otey, C., Poitras, C.B., Fan, S. and Lipson, M., 2012. Near-field radiative cooling of nanostructures. *Nano letters*, *12*(9), pp.4546-4550.

Guo, Y., Cortes, C.L., Molesky, S. and Jacob, Z., 2012. Broadband super-Planckian thermal emission from hyperbolic metamaterials. *Applied Physics Letters*, *101*(13).

Hamdad, S., Diallo, A.T., Chakaroun, M. and Boudrioua, A., 2022. The role of Rayleigh anomalies in the coupling process of plasmonic gratings and the control of the emission properties of organic molecules. Scientific Reports, 12(1), p.3218.

Hasman, E.; Kleiner, V.; Dahan, N.; Gorodetski, Y.; Frischwasser, K.; Balin, I. Manipulation of Thermal Emission by Use of Micro and Nanoscale Structures. *Journal Heat Transfer* **2012**, *134* (3).

Hervé, A., Drévillon, J., Ezzahri, Y., Joulain, K., Meneses, D.D.S. and Hugonin, J.P., 2016. Temperature dependence of a microstructured SiC coherent thermal source. *Journal of Quantitative Spectroscopy and Radiative Transfer*, *180*, pp.29-38.

Herzinger, C.M., Snyder, P.G., Johs, B. and Woollam, J.A., 1995. InP optical constants between 0.75 and 5.0 eV determined by variable-angle spectroscopic ellipsometry. *Journal of applied physics*, *77*(4), pp.1715-1724.

Hesketh, P.J., Zemel, J.N. and Gebhart, B., 1986. Organ pipe radiant modes of periodic micromachined silicon surfaces. *Nature*, *324*(6097), pp.549-551.

Hodgkinson, J. and Tatam, R.P., 2012. Optical gas sensing: a review. *Measurement science and technology*, *24*(1), p.012004.

Hooper, I.R. and Sambles, J.R., 2002. Dispersion of surface plasmon polaritons on short-pitch metal gratings. *Physical Review B*, *65*(16), p.165432.

Hossain, M.M., Jia, B. and Gu, M., 2015. A metamaterial emitter for highly efficient radiative cooling. *Adv. Opt. Mater*, *3*(8), pp.1047-1051.

Howes, A., Nolen, J.R., Caldwell, J.D. and Valentine, J., 2020. Near-unity and narrowband thermal emissivity in balanced dielectric metasurfaces. *Advanced Optical Materials*, *8*(4), p.1901470.

Hu, Y., Li, H., Zhang, Y., Zhu, Y. and Yang, Y., 2020. Enhanced near-field radiation in both TE and TM waves through excitation of Mie resonance. *Physical Review B*, *102*(12), p.125434.

Huang, G., Yengannagari, A.R., Matsumori, K., Patel, P., Datla, A., Trindade, K., Amarsanaa, E., Zhao, T., Köhler, U., Busko, D. and Richards, B.S., 2024. Radiative cooling and indoor light management enabled by a transparent and self-cleaning polymer-based metamaterial. *Nature Communications*, *15*(1), p.3798.

Huang, H., Shan, S. and Zhou, Z., 2023. Near-field thermal diode based on 2d gratings. *International Journal of Heat and Mass Transfer*, *206*, p.123942.

Humlíček, J., Henn, R. and Cardona, M., 2000. Infrared vibrations in LaSrGaO 4 and LaSrAlO 4. *Physical Review B*, *61*(21), p.14554.

Ito, K., Matsui, T. and Iizuka, H., 2014. Thermal emission control by evanescent wave coupling between guided mode of resonant grating and surface phonon polariton on silicon carbide plate. *Applied Physics Letters*, *104*(5).

J. A. Woollam Co., 645 M Street, Lincoln NE 68508 www.jawoollam.com.

Joulain, K., Mulet, J.P., Marquier, F., Carminati, R. and Greffet, J.J., 2005. Surface electromagnetic waves thermally excited: Radiative heat transfer, coherence properties and Casimir forces revisited in the near field. *Surface Science Reports*, *57*(3-4), pp.59-112.

Kittel, A., Wischnath, U.F., Welker, J., Huth, O., Rueting, F. and Biehs, S.A., 2008. Near-field thermal imaging of nanostructured surfaces. *Applied Physics Letters*, *93*(19).

Kivshar, Y. and Miroshnichenko, A., 2017. Meta-optics with Mie resonances. *Optics and Photonics news*, *28*(1), pp.24-31.

Kong, A., Cai, B., Shi, P. and Yuan, X.C., 2019. Ultra-broadband all-dielectric metamaterial thermal emitter for passive radiative cooling. *Optics express*, *27*(21), pp.30102-30115.

Kotlikov, E.N., Ivanov, V.A., Pogareva, V.G. and Khonineva, E.V., 2000. Study of optical constants of PbTe and GeTe films. *Optics and Spectroscopy*, *88*, pp.718-720.

Latella, I., Biehs, S.A. and Ben-Abdallah, P., 2021. Smart thermal management with near-field thermal radiation. *Optics Express*, *29*(16), pp.24816-24833.

Le Gall, J., Olivier, M. and Greffet, J.J., 1997. Experimental and theoretical study of reflection and coherent thermal emissionby a SiC grating supporting a surface-phonon polariton. *Physical Review B*, *55*(15), p.10105.

Lee, N., Kim, T., Lim, J.S., Chang, I. and Cho, H.H., 2019. Metamaterial-selective emitter for maximizing infrared camouflage performance with energy dissipation. *ACS applied materials & interfaces*, *11*(23), pp.21250-21257.

Legendre, J. and Chapuis, P.O., 2022. Overcoming non-radiative losses with AlGaAs PIN junctions for near-field thermophotonic energy harvesting. *Applied Physics Letters*, *121*(19).

Lenert, A., Bierman, D.M., Nam, Y., Chan, W.R., Celanović, I., Soljačić, M. and Wang, E.N., 2014. A nanophotonic solar thermophotovoltaic device. *Nature nanotechnology*, *9*(2), pp.126-130.

Li, D., Jiang, M., Qi, H., Wang, Q. and Liu, C., 2016. Optical Constants of Zinc Selenide at 373 and 423 K in the Wavelength Range of 2–15 μm. *Journal of Applied Spectroscopy*, *83*, pp.512-516.

Li, K., Wu, S., Cao, S., Cai, Q., Ye, Q., Liu, X. and Wu, X., 2021. Transient performance of a nanowire-based near-field thermophotovoltaic system. *Applied Thermal Engineering*, *192*, p.116918.

Li, Q., He, H., Chen, Q. and Song, B., 2021. Radiative thermal diode via hyperbolic metamaterials. *Physical Review Applied*, *16*(6), p.064022.

Li, Y., Gao, W., Li, L., Guo, L., Ge, H., Xie, R., Wang, H., Wang, F. and An, B., 2022. Ultra-broadband thermal radiator for daytime passive radiative cooling based on single dielectric SiO2 on metal Ag. *Energy Reports*, *8*, pp.852-859.

Likam Scientific Instruments Ltd., Waterfield, Epsom, Tadworth KT20 5LR, United Kingdom, www.linkam.co.uk.

Liu, B. and Shen, S., 2013. Broadband near-field radiative thermal emitter/absorber based on hyperbolic metamaterials: Direct numerical simulation by the Wiener chaos expansion method. *Physical Review B—Condensed Matter and Materials Physics*, *87*(11), p.115403.

Liu, T., Xu, R., Yu, P., Wang, Z. and Takahara, J., 2020. Multipole and multimode engineering in Mie resonance-based metastructures. *Nanophotonics*, *9*(5), pp.1115-1137.

Liu, X. and Zhang, Z., 2015. Near-field thermal radiation between metasurfaces. *Acs Photonics*, *2*(9), pp.1320-1326.

Liu, X., Tyler, T., Starr, T., Starr, A.F., Jokerst, N.M. and Padilla, W.J., 2011. Taming the blackbody with infrared metamaterials as selective thermal emitters. *Physical review letters*, *107*(4), p.045901.

Liu, X., Zhao, B. and Zhang, Z.M., 2015. Enhanced near-field thermal radiation and reduced Casimir stiction between doped-Si gratings. *Physical Review A*, *91*(6), p.062510.

Liu, X.L., Bright, T.J. and Zhang, Z.M., 2014. Application conditions of effective medium theory in near-field radiative heat transfer between multilayered metamaterials. *Journal of Heat Transfer*, *136*(9), p.092703.

Lochbaum, A., Dorodnyy, A., Koch, U., Koepfli, S.M., Volk, S., Fedoryshyn, Y., Wood, V. and Leuthold, J., 2020. Compact mid-infrared gas sensing enabled by an all-metamaterial design. *Nano letters*, *20*(6), pp.4169-4176.

Lu, G., Gubbin, C.R., Nolen, J.R., Folland, T., Tadjer, M.J., De Liberato, S. and Caldwell, J.D., 2021. Engineering the spectral and spatial dispersion of thermal emission via polariton–phonon strong coupling. *Nano letters*, *21*(4), pp.1831-1838.

Lu, G., Gubbin, C.R., Nolen, J.R., Folland, T.G., Diaz-Granados, K., Kravchenko, I.I., Spencer, J.A., Tadjer, M.J., Glembocki, O.J., De Liberato, S. and Caldwell, J.D., 2021. Collective phonon–polaritonic modes in silicon carbide subarrays. *ACS nano*, *16*(1), pp.963-973.

Lu, G., Nolen, J.R., Folland, T.G., Tadjer, M.J., Walker, D.G. and Caldwell, J.D., 2020. Narrowband polaritonic thermal emitters driven by waste heat. *ACS omega*, *5*(19), pp.10900-10908.

Lucchesi, C., Cakiroglu, D., Perez, J.P., Taliercio, T., Tournié, E., Chapuis, P.O. and Vaillon, R., 2021. Near-field thermophotovoltaic conversion with high electrical power density and cell efficiency above 14%. *Nano Letters*, *21*(11), pp.4524-4529.

Matsuno, Y. and Sakurai, A., 2017. Perfect infrared absorber and emitter based on a large-area metasurface. *Optical Materials Express*, *7*(2), pp.618-626.

Mirmoosa, M.S., Omelyanovich, M. and Simovski, C.R., 2016. Microgap thermophotovoltaic systems with low emission temperature and high electric output. *Journal of Optics*, *18*(11), p.115104.

Modest, M.F., Mazumder, S., Modest, M.F. and Mazumder, S., 2003. Fundamentals of thermal radiation. *Radiative heat transfer*, *1*, pp.1-29.

Molesky, S., Dewalt, C.J. and Jacob, Z., 2013. High temperature epsilon-near-zero and epsilon-near-pole metamaterial emitters for thermophotovoltaics. *Optics express*, *21*(101), pp.A96-A110.

Neuner, B., Wu, C., Eyck, G.T., Sinclair, M., Brener, I. and Shvets, G., 2013. Efficient infrared thermal emitters based on low-albedo polaritonic meta-surfaces. *Applied Physics Letters*, *102*(21).

Nguyen-Huu, N., Chen, Y.B. and Lo, Y.L., 2012. Development of a polarization-insensitive thermophotovoltaic emitter with a binary grating. *Optics express*, *20*(6), pp.5882-5890.

Otey, C.R., Lau, W.T. and Fan, S., 2010. Thermal rectification through vacuum. *Physical review letters*, *104*(15), p.154301.

Pan, M., Huang, Y., Li, Q., Luo, H., Zhu, H., Kaur, S. and Qiu, M., 2020. Multi-band middle-infrared-compatible camouflage with thermal management via simple photonic structures. *Nano Energy*, *69*, p.104449.

Pejcic, B., Myers, M. and Ross, A., 2009. Mid-infrared sensing of organic pollutants in aqueous environments. *Sensors*, *9*(8), pp.6232-6253.

Petersen, S.J., Basu, S. and Francoeur, M., 2013. Near-field thermal emission from metamaterials. *Photonics and Nanostructures-Fundamentals and Applications*, *11*(3), pp.167-181.

Petersen, S.J., Basu, S., Raeymaekers, B. and Francoeur, M., 2013. Tuning near-field thermal radiative properties by quantifying sensitivity of Mie resonance-based metamaterial design parameters. *Journal of Quantitative Spectroscopy and Radiative Transfer*, *129*, pp.277-286.

Planck, M., 1914. *The theory of heat radiation*. Blakiston.

Pouria, R. and Edalatpour, S., 2024. Tuning the spectrum of near-field radiative heat transfer using Mie resonance based metamaterials. *Physical Review B*, *109*(4), p.045407.

Pouria, R., Chow, P.K., Tiwald, T., Zare, S. and Edalatpour, S., 2022. Far-field thermal radiation from short-pitch silicon-carbide nanopillar arrays. Applied Physics Letters, 121(13).

Razdolski, I., Chen, Y., Giles, A.J., Gewinner, S., Schöllkopf, W., Hong, M., Wolf, M., Giannini, V., Caldwell, J.D., Maier, S.A. and Paarmann, A., 2016. Resonant enhancement of second-harmonic generation in the mid-infrared using localized surface phonon polaritons in subdiffractional nanostructures. *Nano letters*, *16*(11), pp.6954-6959.

Reid, M. T. H.; Johnson, S. G. Fresnel Scattering http://homerreid.github.io/scuff-em-documentation/tests/FresnelScattering/FresnelScattering/.

Reid, M. T. H.; Johnson, S. G. Solving electromagnetic scattering problems with scuff-scatter http://homerreid.github.io/scuff-em-documentation/applications/scuff-scatter/scuff-scatter/.

Reid, M.H. and Johnson, S.G., 2015. Efficient computation of power, force, and torque in BEM scattering calculations. *IEEE Transactions on Antennas and Propagation*, *63*(8), pp.3588-3598.

Rytov, S.M. and Erkku, H., 1959. *Theory of electric fluctuations and thermal radiation* (p. 0280). Bedford, MA: Air Force Cambridge Research Center.

Schuller, J.A., Taubner, T. and Brongersma, M.L., 2009. Optical antenna thermal emitters. *Nature Photonics*, *3*(11), pp.658-661.

Senesky, D.G., Jamshidi, B., Cheng, K.B. and Pisano, A.P., 2009. Harsh environment silicon carbide sensors for health and performance monitoring of aerospace systems: A review. *IEEE Sensors Journal*, *9*(11), pp.1472-1478.

Silva, A.O. and Costa, J.C., 2014. Retrieving the Effective Permittivity of an Optical Metamaterial Structured with Metallic Cylindrical Nanorods-An Analytical Approach Based on the Calculation of the Depolarization Field. *Journal of Microwaves, Optoelectronics & Electromagnetic Applications*, *13*.

Song, B., Fiorino, A., Meyhofer, E. and Reddy, P., 2015. Near-field radiative thermal transport: From theory to experiment. *AIP advances*, *5*(5).

Song, K., Wang, Q., Liu, Q., Zhang, H. and Cheng, Y., 2011. A wireless electronic nose system using a Fe2O3 gas sensing array and least squares support vector regression. *Sensors*, *11*(1), pp.485-505.

Spinelli, P., Verschuuren, M.A. and Polman, A., 2012. Broadband omnidirectional antireflection coating based on subwavelength surface Mie resonators. *Nature communications*, *3*(1), p.692.

Starko-Bowes, R., Dai, J., Newman, W., Molesky, S., Qi, L., Satija, A., Tsui, Y., Gupta, M., Fedosejevs, R., Pramanik, S. and Xuan, Y., 2018. Dual-band quasi-coherent radiative thermal source. *Journal of Quantitative Spectroscopy and Radiative Transfer*, *216*, pp.99-104.

Taniguchi, Y., Isobe, K. and Hanamura, K., 2021. Enhancement of spectrally controlled near-field radiation transfer by magnetic polariton generated by metal–insulator–metal structures. *Applied Thermal Engineering*, *183*, p.116041.

Tittl, A., Michel, A.K.U., Schäferling, M., Yin, X., Gholipour, B., Cui, L., Wuttig, M., Taubner, T., Neubrech, F. and Giessen, H., 2015. A switchable mid-infrared plasmonic perfect absorber with multispectral thermal imaging capability. *Advanced Materials*, *27*(31), pp.4597-4603.

Tiwald, T.E., Woollam, J.A., Zollner, S., Christiansen, J., Gregory, R.B., Wetteroth, T., Wilson, S.R. and Powell, A.R., 1999. Carrier concentration and lattice absorption in bulk and epitaxial silicon carbide determined using infrared ellipsometry. *Physical Review B*, *60*(16), p.11464.

Wang, L.P. and Zhang, Z.M., 2013. Thermal rectification enabled by near-field radiative heat transfer between intrinsic silicon and a dissimilar material. *Nanoscale and microscale thermophysical engineering*, *17*(4), pp.337-348.

Wang, T., Li, P., Chigrin, D.N., Giles, A.J., Bezares, F.J., Glembocki, O.J., Caldwell, J.D. and Taubner, T., 2017. Phonon-polaritonic bowtie nanoantennas: controlling infrared thermal radiation at the nanoscale. *Acs Photonics*, *4*(7), pp.1753-1760.

Watjen, J.I., Liu, X.L., Zhao, B. and Zhang, Z.M., 2017. A computational simulation of using tungsten gratings in near-field thermophotovoltaic devices. *Journal of Heat Transfer*, *139*(5), p.052704.

Wei, J., Ren, Z. and Lee, C., 2020. Metamaterial technologies for miniaturized infrared spectroscopy: Light sources, sensors, filters, detectors, and integration. *Journal of Applied Physics*, *128*(24).

Yang, Y. and Wang, L., 2016. Spectrally enhancing near-field radiative transfer between metallic gratings by exciting magnetic polaritons in nanometric vacuum gaps. *Physical review letters*, *117*(4), p.044301.

Yang, Y., Basu, S. and Wang, L., 2013. Radiation-based near-field thermal rectification with phase transition materials. *Applied Physics Letters*, *103*(16).

Yang, Y., Sabbaghi, P. and Wang, L., 2017. Effect of magnetic polaritons in SiC deep gratings on near-field radiative transfer. *International Journal of Heat and Mass Transfer*, *108*, pp.851-859.

Yokoyama, T., Dao, T.D., Chen, K., Ishii, S., Sugavaneshwar, R.P., Kitajima, M. and Nagao, T., 2016. Spectrally selective mid-infrared thermal emission from molybdenum plasmonic metamaterial operated up to 1000 C. *Adv. Opt. Mater*, *4*(12), pp.1987-1992.

Yu, H., Duan, Y. and Yang, Z., 2018. Selectively enhanced near-field radiative transfer between plasmonic emitter and GaSb with nanohole and nanowire periodic arrays for thermophotovoltaics. *International Journal of Heat and Mass Transfer*, *123*, pp.67-74.

Zare, S., Pouria, R. and Edalatpour, S., 2021. Validity of the effective medium theory for modeling near-field thermal emission by nanowire arrays. *Journal of Quantitative Spectroscopy and Radiative Transfer*, *261*, p.107482.

Zeng, B., Huang, Z., Singh, A., Yao, Y., Azad, A.K., Mohite, A.D., Taylor, A.J., Smith, D.R. and Chen, H.T., 2018. Hybrid graphene metasurfaces for high-speed mid-infrared light modulation and single-pixel imaging. *Light: Science & Applications*, *7*(1), p.51.

Zhai, Y., Ma, Y., David, S.N., Zhao, D., Lou, R., Tan, G., Yang, R. and Yin, X., 2017. Scalable-manufactured randomized glass-polymer hybrid metamaterial for daytime radiative cooling. *Science*, *355*(6329), pp.1062-1066.

Zhang, Z.M., 2020. *Nano/microscale heat transfer*. Cham: Springer.

Zhu, L., Fiorino, A., Thompson, D., Mittapally, R., Meyhofer, E. and Reddy, P., 2019. Near-field photonic cooling through control of the chemical potential of photons. *Nature*, *566*(7743), pp.239-244.

Appendix A

A. 1 Thermal Radiation from a Cylindrical Dipole

A schematic of the problem under consideration is shown in Fig. A-1. A cylindrical dipole is at temperature $T > 0$ K and radiates into the free space.

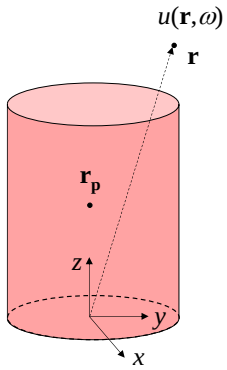

Figure 6-1 A cylindrical dipole is thermally emitting into the free space.
The energy density at location **r** in the free space is desired.

The energy density associated with thermal radiation from a cylindrical dipole at an observation point **r** in the free space can be written as [1]:

$$u(\mathbf{r},\omega) = \frac{1}{2}\varepsilon_0 \text{Trace}\langle \mathbf{E}(\mathbf{r},\omega) \otimes \mathbf{E}(\mathbf{r},\omega)\rangle + \frac{1}{2}\mu_0 \text{Trace}\langle \mathbf{H}(\mathbf{r},\omega) \otimes \mathbf{H}(\mathbf{r},\omega)\rangle \quad \text{(A. 1)}$$

where u is the energy density, ω is the angular frequency, ε_0 and μ_0 are the permittivity and permeability of the free space, respectively, **E** is the electric field, and **H** is the magnetic field. The first term in Eq. A. 1 is the energy density due to the electric field, u^E, while the second term represents energy density associated with the magnetic field, u^H. The electric and magnetic fields at **r** are related to the dipole moment of the cylinder, **p**, as [2]:

$$\mathbf{E}(\mathbf{r},\omega) = \omega^2 \mu_0 \overline{\overline{\mathbf{G}}}^E\left(\mathbf{r},\mathbf{r_p},\omega\right)\cdot \mathbf{p}(\omega) \quad \text{(A. 2a)}$$

$$\mathbf{H}(\mathbf{r},\omega) = -i\omega \overline{\overline{\mathbf{G}}}^H\left(\mathbf{r},\mathbf{r_p},\omega\right)\cdot \mathbf{p}(\,\omega) \quad \text{(A. 2b)}$$

where $\mathbf{r_p}$ is the position of the dipole, and $\overline{\overline{\mathbf{G}}}^E$ ($\overline{\overline{\mathbf{G}}}^H$) is the free space electric (magnetic) Green's function relating the electric (magnetic) field at $\mathbf{r}$ to the dipole moment at $\mathbf{r_p}$ [2]. Substituting Eqs. A. 2a and A. 2b into Eq. A. 1, the energy density can be written as:

$$u(\mathbf{r},\omega) = \frac{1}{2}\omega^4\mu_0^2\varepsilon_0 \mathrm{Trace}\left[\overline{\overline{\mathbf{G}}}^E(\mathbf{r},\mathbf{r_p})\langle \mathbf{p}(\omega)\otimes\mathbf{p}(\omega)\rangle \overline{\overline{\mathbf{G}}}^{E\dagger}(\mathbf{r},\mathbf{r_p})\right] +$$

$$\frac{1}{2}\omega^2\mu_0 \mathrm{Trace}\left[\overline{\overline{\mathbf{G}}}^H(\mathbf{r},\mathbf{r_p})\langle \mathbf{p}(\omega)\otimes\mathbf{p}(\omega)\rangle \overline{\overline{\mathbf{G}}}^{H\dagger}(\mathbf{r},\mathbf{r_p})\right] \quad \text{(A. 3)}$$

where † shows the Hermitian operator. The dipole moment of the cylinder, $\mathbf{p}$, is related to its thermally fluctuating dipole moment, $\mathbf{p}^{fl}$, as [3]:

$$\mathbf{p} = \overline{\overline{\mathbf{B}}}\cdot\mathbf{p}^{fl} \quad \text{(A. 4)}$$

Matrix $\overline{\overline{\mathbf{B}}}$ in Eq. A. 4 is diagonal and its elements are determined as:

$$B_{jj} = \frac{1}{1+L_j(\varepsilon-1)},\ j = x,y,z \quad \text{(A. 5)}$$

where L_j and ε are the depolarization factor [4,5] and the dielectric function of the cylinder, respectively. The spatial correlation function of $\mathbf{p}^{fl}$ is given by the fluctuation dissipation theorem as [3]:

$$\langle \mathbf{p}^{fl}\otimes\mathbf{p}^{fl}\rangle = \frac{4\varepsilon_0\varepsilon" V}{\pi\omega}\Theta(\omega,T)\overline{\overline{\boldsymbol{I}}} \quad \text{(A. 6)}$$

In Eq. A. 6, ε" is the imaginary part of the dielectric function, V is the volume of the cylinder, and $\Theta(\omega,T)$ is the mean energy of an electromagnetic state [3]. The spatial correlation function of the dipole moment of the cylinder appeared in Eq. A. 3 can be found using Eqs. A. 4 – A. 6 as:

$$\langle \mathbf{p}(\omega)\otimes\mathbf{p}(\omega)\rangle = \frac{4\varepsilon_0\varepsilon" V}{\pi\omega}\Theta(\omega,T)\ \overline{\overline{\mathbf{B}}}\cdot\overline{\overline{\mathbf{B}}}^{\dagger} \quad \text{(A. 7)}$$

Substituting Eq. A. 7 into Eq. A. 3, the electric energy density, u^E, is found as:

$$u^E(\mathbf{r},\omega) = \frac{2}{\pi}\omega^3\mu_0^2\varepsilon_0^2\varepsilon''V\Theta(\omega,T)\left[|B_{xx}|^2\left(|G_{xx}^E|^2 + \left|G_{yx}^E\right|^2 + |G_{zx}^E|^2\right) + \left|B_{yy}\right|^2\left(\left|G_{xy}^E\right|^2 + \left|G_{yy}^E\right|^2 + \left|G_{zy}^E\right|^2\right) + |B_{zz}|^2\left(|G_{xz}^E|^2 + \left|G_{yz}^E\right|^2 + |G_{zz}^E|^2\right)\right] \quad \text{(A. 8)}$$

Considering the facts that $\varepsilon''V\left|B_{jj}\right|^2 = \mathrm{Im}\left[\alpha_j\right]$ and $B_{xx} = B_{yy}$ for a cylindrical dipole, Eq. A. 8 can be written as:

$$u^E(\mathbf{r},\omega) = \frac{2}{\pi}\omega^3\mu_0^2\varepsilon_0^2\Theta(\omega,T)\left[\mathrm{Im}[\alpha_x]\left(|G_{xx}^E|^2 + \left|G_{yx}^E\right|^2 + |G_{zx}^E|^2 + \left|G_{xy}^E\right|^2 + \left|G_{yy}^E\right|^2 + \left|G_{zy}^E\right|^2\right) + \mathrm{Im}[\alpha_z]\left(|G_{xz}^E|^2 + \left|G_{yz}^E\right|^2 + |G_{zz}^E|^2\right)\right] \quad \text{(A. 9)}$$

The magnetic energy density, u^H, can be written in a similar manner as:

$$u^H(\mathbf{r},\omega) = \frac{2}{\pi}\omega\mu_0\varepsilon_0\Theta(\omega,T)\mathrm{Trace}\left[\mathrm{Im}[\alpha_x]\left(|G_{xx}^H|^2 + \left|G_{yx}^H\right|^2 + |G_{zx}^H|^2 + \left|G_{xy}^H\right|^2 + \left|G_{yy}^H\right|^2 + \left|G_{zy}^H\right|^2\right) + \mathrm{Im}[\alpha_z]\left(|G_{xz}^H|^2 + \left|G_{yz}^H\right|^2 + |G_{zz}^H|^2\right)\right] \quad \text{(A. 10)}$$

As it is seen from Eqs. A. 9 and A. 10, the electric and magnetic energy densities are dependent on the imaginary parts of the polarizability of the dipole along x and z directions. When the denominators of $\mathrm{Im}[\alpha_x]$ and $\mathrm{Im}[\alpha_z]$ become negligible, the energy density resonantly increases due to thermal emission of transversal and longitudinal localized surface phonons, respectively.

A. 2 Ellipsometry Measurement of the Dielectric Function of 6H-SiC at 400°C

To determine 6H-SiC ordinary and extraordinary complex dielectric functions at a temperature of 400°C, a single-side polished 6H-SiC c-plane (<0001>) substrate was mounted inside of a Linkam TSEL1000 high temperature stage [6] attached to a J. A. Woollam IR-VASE Mark II ellipsometer [7]. Data were acquired every 4 cm^{-1} from 333 – 5900 cm^{-1} (1.7 – 30 μm, 0.041 – 0.73 eV). All data were acquired at 50° angle of incidence (a relatively shallow angle for ellipsometric measurements), because the light beam needed to clear the edge of the crucible heater.

The sample was modeled as a uniaxial anisotropic substrate. For a c-plane surface, the ordinary dielectric response (ε_o) interacts with the electric field component parallel to the surface (perpendicular to the c-axis), and extraordinary dielectric response (ε_e) interacts with electric fields normal to the surface (parallel to the c-axis). The phonon modes in both ε_o and ε_e were modeled using four asymmetric Lorentz oscillators to account for coupling between the modes[8]. The various oscillator parameters were optimized until the model fit the ellipsometric data using a procedure similar to Tiwald et al. [9] (also see Herzinger et al. [10]).

Because the substrate's c-axis is normal to the <0001> surface, the measured spectra is dominated by ε_o and has very limited sensitivity to ε_e, except for a narrow range of wavenumbers between 960 and 1070 cm^{-1} which is the epsilon-near-zero (ENZ) region for both ε_o and ε_e. The high sensitivity to ε_o means that it is relatively easy to extract ε_o versus temperature. It is much more difficult to track the evolution of $\varepsilon_e$with temperature, especially when the large ε_o phonon mode is broadened at higher temperatures which tends to mask the effects of ε_e in the ENZ region. Given this limited sensitivity to ε_e, we made the assumption that the magnitude and broadening versus temperature would shift at the same rate for the ε_e phonon modes as for the ε_o modes. Using that assumption, the model-generated data fit the experimental data very well, but the ε_e evolution with temperature has not been independently determined. The measured ordinary and extraordinary dielectric functions are plotted in Fig. A-2.

A. 3 Far-, Middle-, and Near-Field Components of the Free Space Green's Function

The free space electric Green's function relating the electric field observed at point **r** to an emitting dipole at location $\mathbf{r}_p \neq \mathbf{r}$ in the free space (see Fig. A-1) is given by [3]:

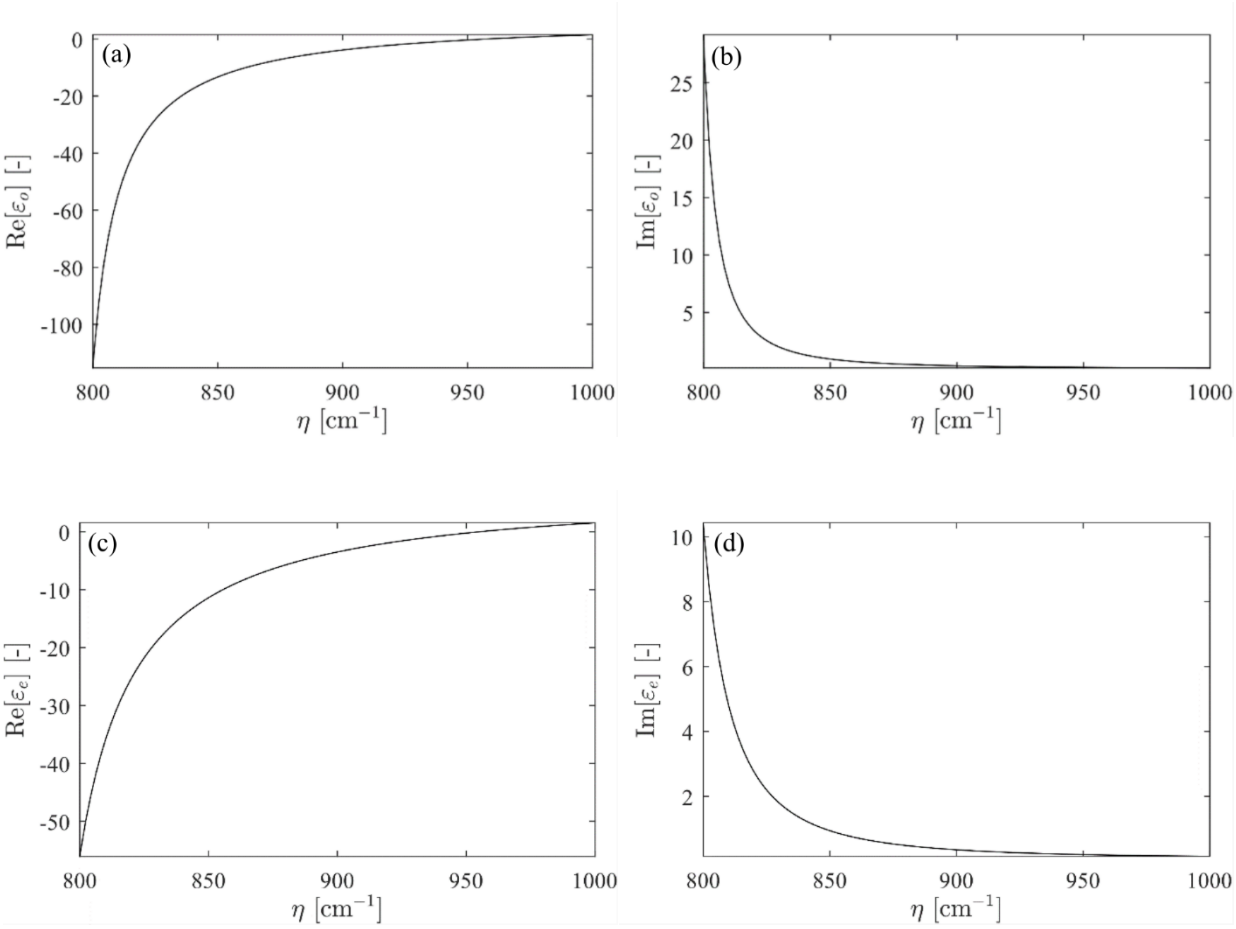

Figure 6-2 The real and imaginary parts of the measured dielectric function.
(a,b) ordinary dielectric function, and (b,c) extraordinary dielectric functions of 6H-SiC at 400°C.

$$\bar{\bar{\mathbf{G}}}(\mathbf{r},\mathbf{r_p}) = \frac{e^{ik_0R}}{4\pi R}\left\{\left[1-\frac{1}{(k_0R)^2}+\frac{i}{k_0R}\right]\bar{\bar{\mathbf{I}}}-\left[1-\frac{3}{(k_0R)^2}+\frac{3i}{k_0R}\right]\hat{\mathbf{R}}\otimes\hat{\mathbf{R}}\right\} \quad \text{(A. 11)}$$

where k_0 is the magnitude of the wavevector in the free space, i is the imaginary unit, $\bar{\bar{\mathbf{I}}}$ is the unit dyad, R is the magnitude of the vector $\mathbf{R}=\mathbf{r}-\mathbf{r_p}$, $\hat{\mathbf{R}}=\frac{\mathbf{R}}{R}$, and $\otimes$ denotes the outer product.

The Green's function can be decomposed into three far-field ($\bar{\bar{\mathbf{G}}}^{\mathrm{FF}}$), middle-field ($\bar{\bar{\mathbf{G}}}^{\mathrm{MF}}$), and near-field ($\bar{\bar{\mathbf{G}}}^{\mathrm{NF}}$) components [11]:

$$\bar{\bar{\mathbf{G}}}^{\mathrm{FF}}(\mathbf{r},\mathbf{r_p}) = \frac{e^{ik_0R}}{4\pi R}\left[\bar{\bar{\mathbf{I}}}-\hat{\mathbf{R}}\otimes\hat{\mathbf{R}}\right] \quad \text{(A. 12a)}$$

$$\bar{\bar{\mathbf{G}}}^{\mathrm{MF}}(\mathbf{r},\mathbf{r_p}) = \frac{ie^{ik_0R}}{4\pi k_0 R^2}\left[\bar{\bar{\mathbf{I}}} - 3\hat{\mathbf{R}}\otimes\hat{\mathbf{R}}\right] \quad \text{(A. 12b)}$$

$$\bar{\bar{\mathbf{G}}}^{\mathrm{NF}}(\mathbf{r},\mathbf{r_p}) = \frac{e^{ik_0R}}{4\pi k_0^2 R^3}\left[\bar{\bar{\mathbf{I}}} + 3\hat{\mathbf{R}}\otimes\hat{\mathbf{R}}\right] \quad \text{(A. 12c)}$$

Equations A. 12a – A. 12c show that the far-field, middle field, and near-field components of the Green's function vary with the distance between the source dipole and the observation point, R, as $\frac{1}{R}$, $\frac{1}{R^2}$, and $\frac{1}{R^3}$, respectively.

A. 4 Isofrequency contours of surface phonon polaritons for short- and long-pitch shallow gratings

Figures A-3a and A-3b show the isofrequnecy contours of surface phonon polaritons (SPhPs) for a two-dimensional shallow grating at a wavenumber of η = 937.8 cm^{-1} corresponding to the SPhP resonance of a bare 6H-SiC substrate at T = 400°C. Figure S3a corresponds to a long-pitch array with a pitch size $\Lambda = \frac{3\lambda}{4}$, while Fig. A-3b shows the isofrequnecy contour for a short-pitch array with $\Lambda = 0.09\lambda$. The area inside red circles correspond to the electromagnetic modes with a parallel component of the wavevector, $k_\rho = \sqrt{k_x^2 + k_y^2}$, smaller than the wavevector in the free space, k_0. The blue circles show the parallel component of the wavevector of the SPhPs, k_ρ^{SPhP}, for a bare substrate at the given wavenumber, which is obtained using the dispersion relation as $k_\rho^{\mathrm{SPhP}} = k_0\sqrt{\frac{\varepsilon}{\varepsilon+1}}$ [12]. The purple circles represent the modified parallel component of the wavevector of SPhPs in the presence of the shallow gratings found as $k_{\rho,mn}^{\mathrm{SPhP}} = k_\rho^{\mathrm{SPhP}} \pm m\frac{2\pi}{\Lambda} \pm n\frac{2\pi}{\Lambda}$ for $m, n = \pm 1$. Figure A-2a shows that $k_{\rho,mn}^{\mathrm{SPhP}}$ for long-pitch gratings can be located within the free space circle, while the short-pitch arrays cannot reduce $k_{\rho,mn}^{\mathrm{SPhP}}$ enough to be less than k_0.

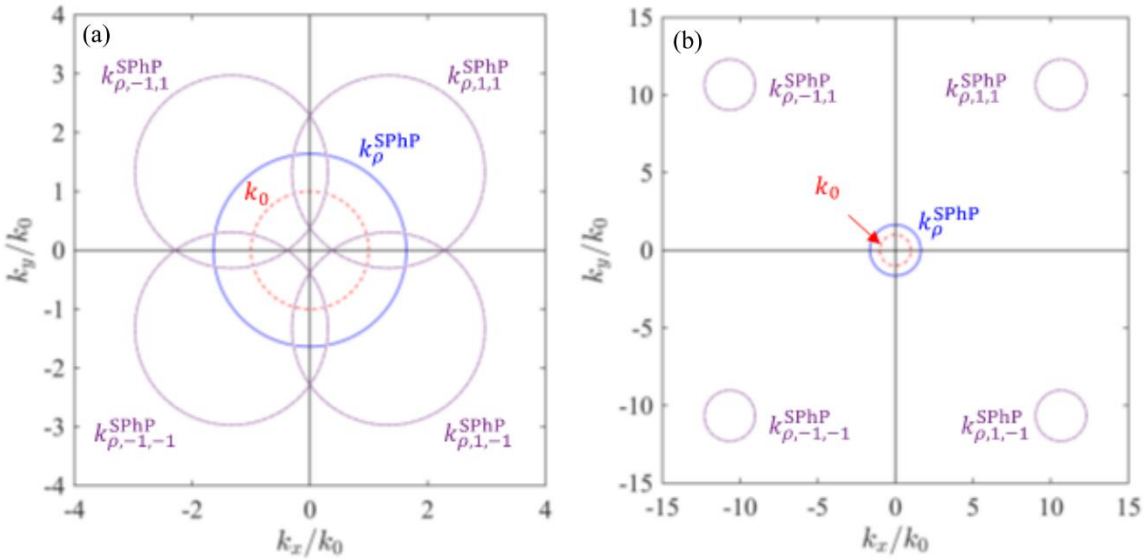

Figure 6-3 The isofrequency contour of SPhPs.
for (a) a long-pitch, shallow grating with a pitch of $\Lambda = \frac{3\lambda}{4}$, and (b) a short-pitch, shallow grating with a pitch of $\Lambda = 0.09\lambda$.

A. 5 Method for Fabricating SiC Nanopillars

Semi-insulating, 430 micron-thick 6H-SiC <0001> wafers (MSE Supplies) were cleaned in piranha solution and DI water. For use as a hard etch mask, a 100-nm chromium layer was deposited using RF sputtering at a rate of 2.6A/s. The wafer was coated in a protective layer of Shipley S1818 photoresist and diced into 12-mm square chips, followed by photoresist stripping and another piranha cleaning step. Individual Cr/SiC chips were coated with a 300-nm layer of maN-2403 negative-tone resist. A 1-cm square array of 500 nm-diameter circles was patterned into the resist using a Nanobeam Ltd. nB4 e-beam writer with an acceleration voltage of 80 kV and beam current of 31 nA. The exposed pattern was developed in AZ 300 MIF developer and rinsed with DI water. The chromium circles were defined using inductively-coupled plasma reactive ion etching (ICP-RIE) in a Cl2/O2 plasma (Oxford PlasmaPro Cobra 100). Any residual resist was then removed by piranha cleaning. The SiC nanopillars were defined by a second ICP-

RIE step, utilizing a SF6/O2 plasma. The forward RIE power and ICP power were set at 150 and 1500 watts, respectively, with a pressure of 6 mtorr. The height of the pillars was controlled by the etch duration. Residual chromium hard mask layers were removed in a commercial chromium etchant (Transene CR1A) at room temperature overnight. Final treatment of the nanopillars in 50:1 buffered oxide etch solution was used to remove residual surface oxides and/or particles.

A. 6 References

[1] Edalatpour, S., 2019. Near-field thermal emission by periodic arrays. *Physical Review E*, *99*(6), p.063308.

[2] David Jackson, J. *Classical Electrodynamics*, 3rd edition.; Wiley, 1998.

[3] Edalatpour, S., Čuma, M., Trueax, T., Backman, R. and Francoeur, M., 2015. Convergence analysis of the thermal discrete dipole approximation. *Physical Review E*, *91*(6), p.063307.

[4] Silva, A.O. and Costa, J.C., 2014. Retrieving the Effective Permittivity of an Optical Metamaterial Structured with Metallic Cylindrical Nanorods-An Analytical Approach Based on the Calculation of the Depolarization Field. *Journal of Microwaves, Optoelectronics & Electromagnetic Applications*, *13*.

[5] Zare, S., Pouria, R. and Edalatpour, S., 2021. Validity of the effective medium theory for modeling near-field thermal emission by nanowire arrays. *Journal of Quantitative Spectroscopy and Radiative Transfer*, *261*, p.107482.

[6] Likam Scientific Instruments Ltd., Waterfield, Epsom, Tadworth KT20 5LR, United Kingdom, www.linkam.co.uk.

[7] J. A. Woollam Co., 645 M Street, Lincoln NE 68508 www.jawoollam.com.

[8] Humlíček, J., Henn, R. and Cardona, M., 2000. Infrared vibrations in LaSrGaO 4 and LaSrAlO 4. *Physical Review B*, *61*(21), p.14554.

[9] Tiwald, T.E., Woollam, J.A., Zollner, S., Christiansen, J., Gregory, R.B., Wetteroth, T., Wilson, S.R. and Powell, A.R., 1999. Carrier concentration and lattice absorption in bulk and epitaxial silicon carbide determined using infrared ellipsometry. *Physical Review B*, *60*(16), p.11464.

[10] Herzinger, C.M., Snyder, P.G., Johs, B. and Woollam, J.A., 1995. InP optical constants between 0.75 and 5.0 eV determined by variable-angle spectroscopic ellipsometry. *Journal of applied physics*, *77*(4), pp.1715-1724.

[11] Arnoldus, H.F., 2001. Representation of the near-field, middle-field, and far-field electromagnetic Green's functions in reciprocal space. *JOSA B*, *18*(4), pp.547-555.

[12] Joulain, K., Mulet, J.P., Marquier, F., Carminati, R. and Greffet, J.J., 2005. Surface electromagnetic waves thermally excited: Radiative heat transfer, coherence properties and Casimir forces revisited in the near field. *Surface Science Reports*, *57*(3-4), pp.59-112.

Appendix B

B. 1 Modeling Near-Field Radiative Heat Transfer using the Fourier Modal Method

Near-field radiative heat flux between the two Mie resonance-based metamaterials is calculated using the Fourier modal method as implemented in the MESH electromagnetic solver [1]. A schematic of the system under study is shown in Fig. B-1.

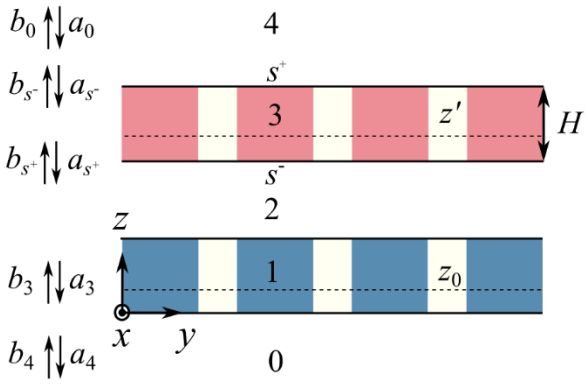

Figure 7-1 A schematic of the system under study.
Two Mie resonance-based metamaterials with a height of H (media 1 and 3) are periodic in the x-y plane and are separated by a vacuum gap.

The two metamaterials, labeled as media 1 and 3, have a height of H along the z-axis and they are periodic in the x and y directions. The spectral heat flux can be found using the z component of the Poynting vector as [22]:

$$Q_\omega = \frac{1}{2}[\Theta(\omega, T_3) - \Theta(\omega, T_1)]\ \mathrm{Re}\{\mathrm{Tr}[\Pi^\intercal \langle \mathbf{E}\mathbf{H}^* \rangle]\} \tag{B. 1}$$

where $\Theta(\omega, T)$ is the mean energy of an electromagnetic state [2,3], ω is the angular frequency, T_1 and T_3 are the temperatures of the two metamaterials, **E** and **H** are the electric and magnetic fields, respectively, Re indicates the real part of a complex tensor, Tr and subscripts * and ⊺ refer to the trace, complex conjugate and transpose operations, respectively, and $\Pi_{\mathbf{r},\alpha;\mathbf{r}',\beta} = \pi_{z\alpha\beta}$ with

$\mathbf{r}$ and $\mathbf{r}'$ being the position vectors in the x-y plane and $\pi_{z\alpha\beta}$ being the three dimensional Levi-Civita symbol. The electric and magnetic fields can be written using the electric ($\mathbf{G}_e$) and magnetic ($\mathbf{G}_h$) Green's functions as:

$$\mathbf{E} = \mathbf{G}_e\mathbf{J} \tag{B. 2a}$$

$$\mathbf{H} = \mathbf{G}_h\mathbf{J} \tag{B. 2b}$$

where the stochastic current density, $\mathbf{J}$, is the source of thermal radiation. The mean value of the stochastic current density is zero, while its spatial correlation is given by the fluctuation dissipation theorem as [2,3]:

$$\langle \mathbf{J}_\alpha(\mathbf{r}, z)\mathbf{J}^*_\beta(\mathbf{r}'z')\rangle = \frac{4\epsilon_0\omega}{\pi}\Theta(\omega, T)\delta(z - z')\Gamma_{\alpha\beta} \tag{B. 3}$$

In Eq. B. 3, ϵ_0 is the permittivity of the free space, δ is the Dirac function, and $\Gamma_{\alpha\beta}$ is defined as $\Gamma_{\alpha\beta} = \gamma_{\alpha\beta}\delta(\mathbf{r} - \mathbf{r}')$ where γ is the imaginary part of the dielectric function tensor.

Substituting for $\mathbf{E}$ and $\mathbf{H}$ using the Green's functions presented in Eq. B. 2 and utilizing Eq. B. 3, the net heat flux given by Eq. B. 1 can be written as:

$$Q_\omega = \frac{2\epsilon_0\omega}{\pi}[\Theta(\omega, T_3) - \Theta(\omega, T_1)]\int_0^H \mathrm{Re}\{\mathrm{Tr}[\Pi^\intercal\mathbf{G}_e\Gamma\mathbf{G}_h^\dagger]\}dz' \tag{B. 4}$$

Where the superscript † refers to Hermitian operator. The Green's functions $\mathbf{G}_e$ and $\mathbf{G}_h$ relate the electric and magnetic fields at point $\mathbf{r}$ generated due to emission by a source, $\mathbf{J}$, located at $\mathbf{r}'$. To find the Green's functions, the in-plane electromagnetic fields $e_\parallel$ and $h_\parallel$ at a given location z are first expanded into eigenmodes as [1]:

$$e_\parallel(z) = M^e F(z)a \tag{B. 5a}$$

$$h_\parallel(z) = M^h F(H - z)b \tag{B. 5b}$$

where the matrix M^e (M^h) includes the expansion coefficients of $e_{\|}$ ($h_{\|}$) in terms of the modal basis, a and b vectors contain the modal amplitudes for the forward and backward propagating modes (see Fig. B-1), respectively, and F is a diagonal matrix defined as $F_{nn} = e^{-\mathrm{i}q_n z}$ with q_n representing the nth eigenvalue. The modal amplitudes are found using the scattering matrix method and substituted in Eqs. B. 5a and B. 5b as [2]:

$$e_{\|} = R_e L M_s^{-1} P \mathbf{J} \tag{B. 6a}$$

$$h_{\|}(z) = R_h L M_s^{-1} P \mathbf{J} \tag{B. 6b}$$

In Eqs. B. 6a and B. 6b, $L = \begin{bmatrix} F_s(H-z') & 0 \\ 0 & F_s(z') \end{bmatrix}$, $P = \begin{pmatrix} \frac{1}{\mathrm{i}\omega\epsilon_0}\frac{\partial}{\partial x}\eta_{zx} & \frac{1}{\mathrm{i}\omega\epsilon_0}\frac{\partial}{\partial x}\eta_{zy} & \frac{1}{\mathrm{i}\omega\epsilon_0}\frac{\partial}{\partial x}\eta_{zz} \\ \frac{1}{\mathrm{i}\omega\epsilon_0}\frac{\partial}{\partial y}\eta_{zx} & \frac{1}{\mathrm{i}\omega\epsilon_0}\frac{\partial}{\partial y}\eta_{zy} & \frac{1}{\mathrm{i}\omega\epsilon_0}\frac{\partial}{\partial y}\eta_{zz} \\ 0 & 1 & 0 \\ -1 & 0 & 0 \end{pmatrix}$,

and $\begin{bmatrix} R_e \\ R_h \end{bmatrix} = M_r \begin{bmatrix} F_r(z_0)D_1 \\ F_r(H-z_0)D_2 \end{bmatrix} K_1^{-1}[\mathbf{I} \quad K_2]$ where $K_1 = \mathbf{I} - F_s S_{12}(s^-, 0) F_s S_{21}(s^+, 4)$ and $K_2 = -F_s S_{12}(s^-, 0)$, and $D_1 = \left(\mathbf{I} - S_{12}(s^+, r) S_{21}(r, N)\right)^{-1} S_{11}(s^+, r)$ and $D_2 = S_{21}(r, N) D_1$ [1]. In these equations, the subscripts s and r refer to the source and receiver layers, respectively, S_{ij} (m, n) is the element ij of the scattering matrix between layers m and n, $\mathbf{I}$ is the unit matrix, z' is z-component of the location of the source, z_0 is the location at which the electromagnetic field is evaluated, η is the inverse of the dielectric tensor ϵ, and s^+ and s^- are two artificial layers with a thickness of 0 defined at the top and bottom surfaces of emitting layer s, respectively. The s^+ and s^- layers have the same dielectric function as layer s.

Comparing Eqs. B. 6 with B. 2, the electric and magnetic Green's functions are found as:

$$\mathbf{G}_e = R_e L M_s^{-1} P \tag{B. 7a}$$

$$\mathbf{G}_h = R_h L M_s^{-1} P \tag{B. 7b}$$

Substituting Eqs. B. 7a and B. 7b into Eq. B. 4 and evaluating the integral, the spectral heat flux between the two metamaterials is found as [1]:

$$Q_\omega = \frac{2\epsilon_0\omega}{\pi}[\Theta(\omega,T_3)-\Theta(\omega,T_1)]\mathrm{Re}\left\{\mathrm{Tr}\left[\Pi^{\intercal}R_e[(M_s^{-1}P\Gamma P^{\dagger}[M_s^{-1}]^{\dagger})\circ \mathrm{Y}]R_h^{\dagger}\right]\right\} \quad \text{(B. 8)}$$

where $\circ$ indicates Hadamard product and matrix $\mathrm{Y} = \begin{bmatrix} y_1 & y_2 \\ y_2 & y_1 \end{bmatrix}$ is defined as [1]:

$$Y_{1,(mn)} = \frac{1-e^{-\mathrm{i}(q_m-q_n^*)H}}{\mathrm{i}(q_m-q_n^*)} \quad \text{(B. 9a)}$$

$$Y_{2,(mn)} = \frac{e^{\mathrm{i}q_n^*H}-e^{-\mathrm{i}q_mH}}{\mathrm{i}(q_m-q_n^*)} \quad \text{(B. 9b)}$$

In Eq. B. 9, q_m and q_n are the mth and nth eigenvalues of the electromagnetic field, respectively.

B. 2 References

[1] Chen, K., Zhao, B. and Fan, S., 2018. MESH: A free electromagnetic solver for far-field and near-field radiative heat transfer for layered periodic structures. *Computer Physics Communications*, *231*, pp.163-172.

[2] Zhang, Z.M., 2020. *Nano/microscale heat transfer*. Cham: Springer.

[3] Joulain, K., Mulet, J.P., Marquier, F., Carminati, R. and Greffet, J.J., 2005. Surface electromagnetic waves thermally excited: Radiative heat transfer, coherence properties and Casimir forces revisited in the near field. *Surface Science Reports*, *57*(3-4), pp.59-112.

Appendix C

C. 1 Supplemental Material for Tuning the Spectrum of Near-Field Radiative Heat Transfer using Mie Resonance-Based Metamaterials

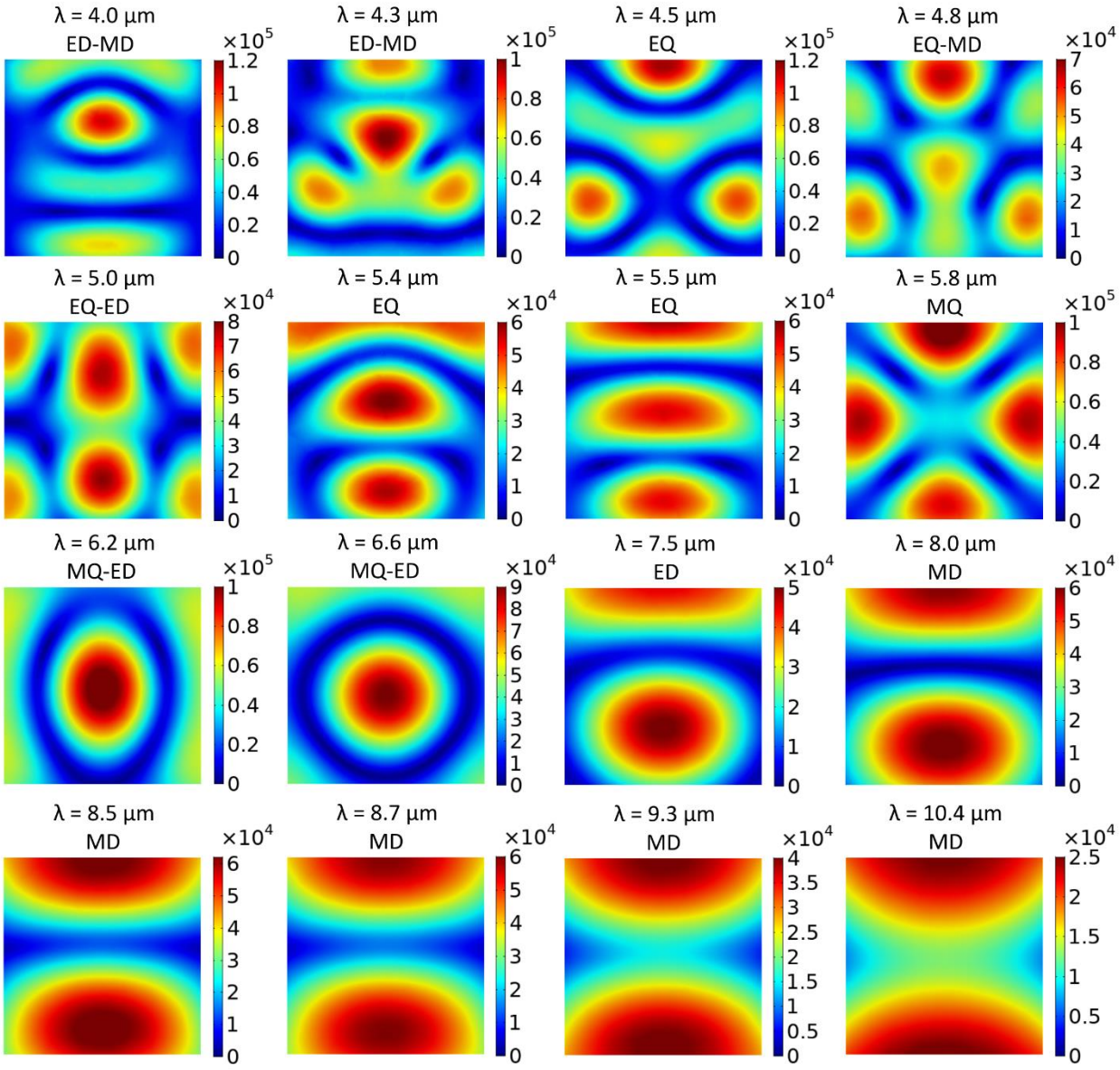

Figure 8-1 The spatial distribution of the induced electric field within the micro-cubes at the spectral locations of the NFRHT peaks.

The electric field is plotted in the $x = \frac{L}{2}$ plane. The complex refractive index is $\tilde{n}$ = 3.5 + 0.05i, while $L = W = H = D$ = 2 μm and d = 1 μm. The unit for the color bar is V/m.

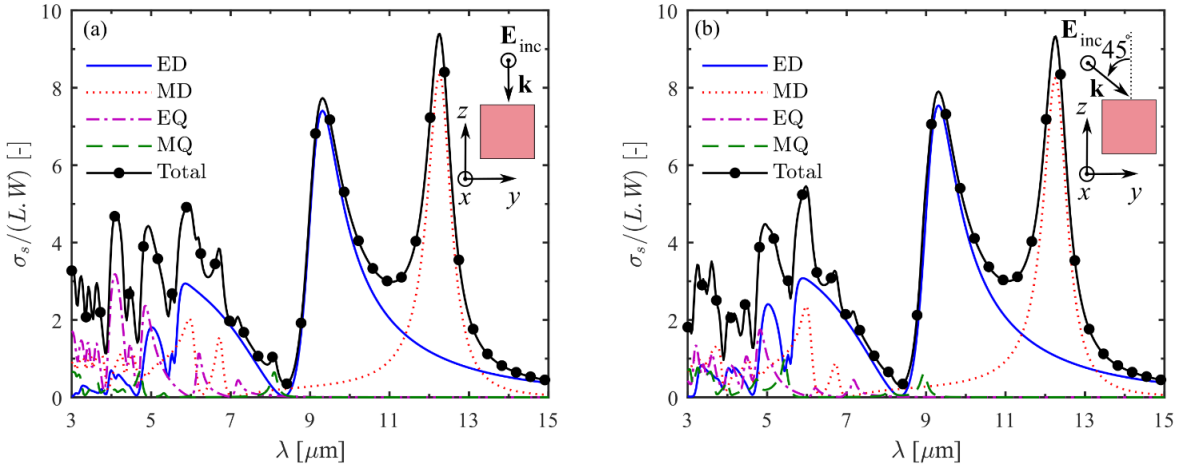

Figure 8-2 The scattering cross section of an individual micro-cube.
The scattering cross section is normalized by the geometrical cross section, when the micro-cube is illuminated by an incident plane wave. The incident electric field is polarized along the x-axis, while it propagates along the z-axis in Panel (a) and at angle of 45° with respect to the z-axis in Panel (b). See the insets of Panels (a) and (b) for schematics. The refractive index of the micro-cubes and the separation gap of the metamaterials are $\tilde{n}$ = 5.0 + 0.05i and d = 1 μm, respectively, while $L = H = W = D$ = 2 μm.

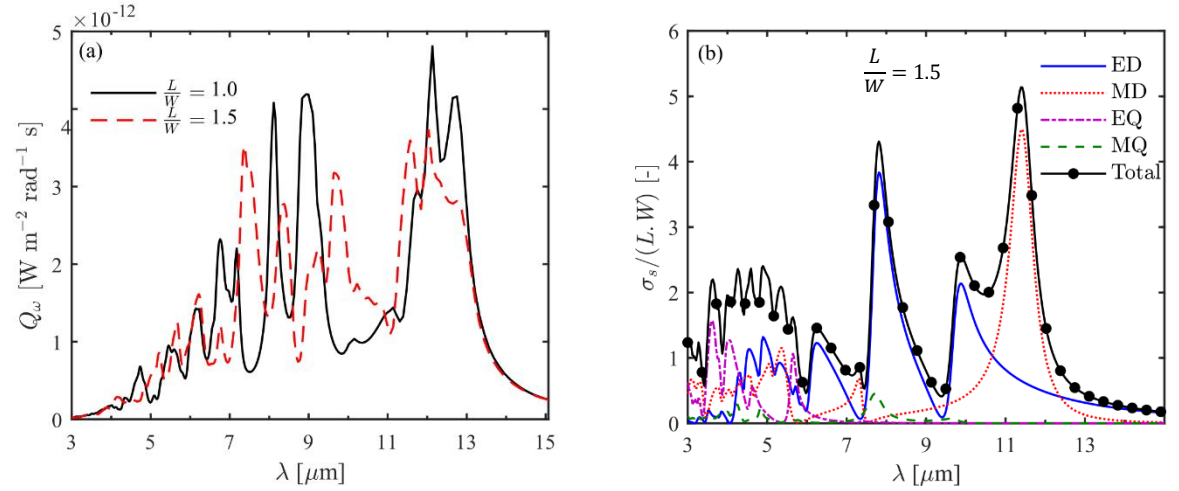

Figure 8-3 The effect of the geometry of the Mie resonators on the heat flux.
(a) The effect of cubes' length to width ratio ($\frac{L}{W}$) on the spectrum of near-field heat flux between two Mie resonance-based metamaterials. $\tilde{n}$ = 5.0 + 0.05i, d = 1 μm, and $L = W$. The array pitch is 4 μm, and the volume of the Mie resonators is 8 μm^3. (b) Multipole expansion of scattering cross section for the case with $\frac{L}{W}$ = 1.5.

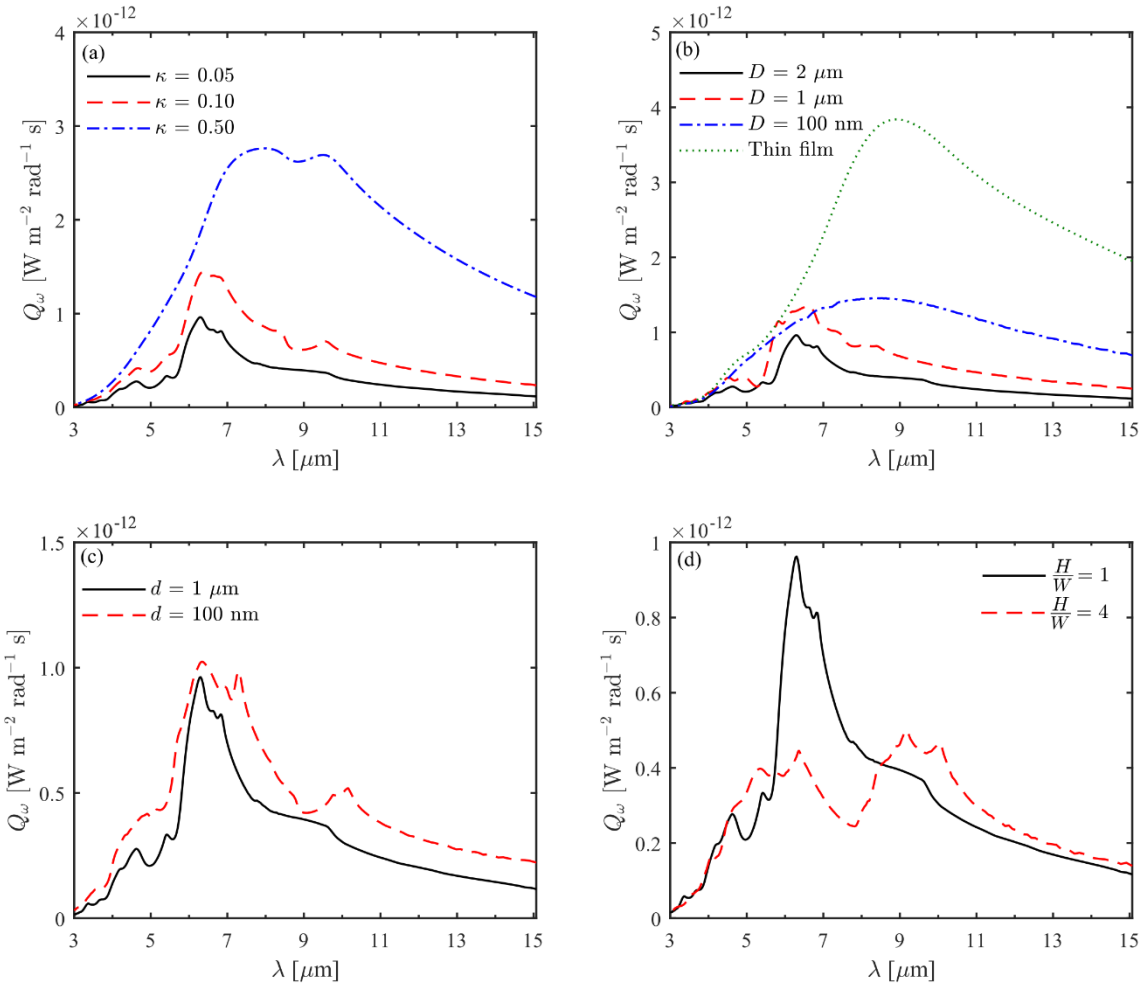

Figure 8-4 The spectrum of near-field heat flux between the two Mie resonance-based metamaterials schematically shown in Fig. 4-1.

(a) The effect of the extinction coefficient, κ, on the heat flux. $L = W = H = D = 2$ μm, $n = 2.4$, and $d = 1$ μm (b) The effect of cube interspacing, D, on the heat flux. $L = W = H = 2$ μm, $\tilde{n} = 2.4 + 0.05$i, and $d = 1$ μm. (c) The effect of the separation gap, d, on the heat flux. $L = W = H = D = 2$ μm and $\tilde{n} = 2.4 + 0.05$i. (d) The effect of the geometry of the Mie resonators on the heat flux. $\tilde{n} = 2.4 + 0.05$i, $d = 1$ μm, and $L = W$. The array pitch is 4 μm, and the volume of the Mie resonators is 8 μm^3.

Appendix D

D. 1 Fabrication of 6H-SiC Microcuboids

6H-SiC microcuboids with side lengths 2.1 by 2.1 by 2.3 μm and an inter-cube spacing of D = 1.47 μm (pitch of Λ = 3.57 μm) were fabricated on a 430-μm-thick 6H-SiC substrate. Initially, 100 nm of chrome was deposited on the substrate to serve as a hard mask for the etching process. This was followed by spin-coating PMMA (polymethyl methacrylate) in preparation of the dicing saw. A 1.5 cm by 1.5 cm area, onto which the microcubes are written, was centered within a 2 cm by 2 cm area using the NanoBeam Electron Beam Lithography system at 70 kV and 70 nA. The resist stack consisted of 2 layers of PMMA 950k A2 spun at 4000 rpm with a bake at 180℃ for 2 minutes followed by 6% HSQ in MIBK spun at 4000 rpm for 1 min. Following exposure of the resist stack, a 30-minute acetone development was done. Next, the chrome layer was etched using the chlorine reactive ion etching (Cl-RIE) Oxford Cobra III-V followed by the SiC etching using the fluorine RIE (F-RIE) in the Oxford Cobra 300. The parameters of the Cl-RIE and F-RIE are listed in Table A1. Lastly, the samples were immersed in chrome etchant 1020 to remove the hard mask and then rinsed in water. An SEM image of the fabricated sample is shown in Fig. 3-3(a).

	Cl-RIE	F-RIE
Gas Flow	Cl_2: 42 sccm O_2: 8 sccm	SF6: 40 sccm O2: 10 sccm
Pressure	12 mTorr	6 mTorr
Forward power	10 W	150 W
DC bias	109 V	247 V

Table D-1 The parameters of the Cl-RIE and F-RIE.

Appendix E

E. 1 Emissivity Measurement

The spectral, directional emissivity of the sample is measured directly using an in-house emissometer, which is schematically shown in Fig. E-1 [1]. The sample is affixed onto an aluminum stage using S-Clip holders. A cartridge heater (Watlow Firerod) is installed inside the aluminum stage to raise the temperature of the sample to 400°C. The stage is mounted on a rotary stage (Standa Inc., 8MR174-11-20) to enable directional measurements of the emissivity. The exact temperature of the sample is determined by knowing the emissivity of the sample (= 1.0) at the Christiansen wavelength (10.1 µm) [1,2]. Thermal emission from the heated sample ($I_{S,\lambda}$) is directed towards a Fourier Transform Infrared (FTIR) spectrometer (Thermo Fisher Scientific, Nicolet iS50), equipped with a mercury-cadmium-telluride detector (Thermo Fisher Scientific, MCT-A/CdTe) using flat (Thorlabs, PFSQ20-03-M03) and parabolic (Thorlabs, MPD269-M03) mirrors. An iris element is placed in front of the sample to restrict the collection angle. Thermal radiation from a blackbody (ISDC, IR-563), with the same optical path and temperature as the sample, is also measured ($I_{BB,\lambda}$). Background thermal radiation ($I_{E,\lambda}$) is recorded with both the heater and the blackbody turned off and is subtracted from the sample and blackbody emissions. The spectral, directional emissivity is then found as $\varepsilon'_\lambda = \frac{(I_{S,\lambda} - I_{E,\lambda})}{(I_{BB,\lambda} - I_{E,\lambda})}$.

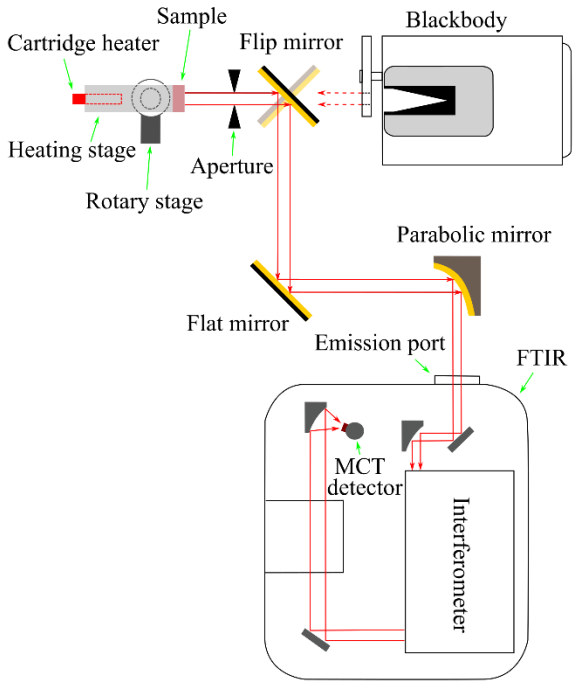

Figure 9-1 A schematic of the experimental setup used for direct measurement of spectral, directional emissivity.

E. 2 References

[1] Arnold, C.; Marquier, F.; Garin, M.; Pardo, F.; Collin, S.; Bardou, N.; Pelouard, J.-L.; Greffet, J.-J. Coherent Thermal Infrared Emission by Two-Dimensional Silicon Carbide Gratings. *Physical Review B* **2012**, *86* (3), 035316.

[2] Pouria, R., Chow, P.K., Tiwald, T., Zare, S. and Edalatpour, S., 2022. Far-field thermal radiation from short-pitch silicon-carbide nanopillar arrays. Applied Physics Letters, 121(13).

BIOGRAPHY OF THE AUTHOR

Ramin Pouria was born in Mianeh, Iran, in 1990. He was raised in Mianeh and graduated from the National Organization for Development of Exceptional Talents high school in 2008. He earned his bachelor's degree in mechanical engineering with a concentration in Thermo-Fluid sciences from Azerbaijan University, Tabriz, Iran in 2012. After taking the national entrance exam, he was admitted to the University of Tehran to pursue his Master's studies in Mechanical Engineering with a concentration in renewable energies engineering, from which he graduated in 2016. Later, he joined the Department of Mechanical Engineering at the University of Maine in August 2019. Ramin is a candidate for the Doctor of Philosophy degree in Mechanical Engineering from the University of Maine and is expected to graduate in August 2024.